SUSPENSION PROCESSING AND PRESSURELESS SINTERING OF SILICON CARBIDE WHISKER-REINFORCED ALUMINA-MATRIX COMPOSITES

BY

HAE-WEON LEE

A DISSERTATION PRESENTED TO THE GRADUATE SCHOOL
OF UNIVERSITY OF FLORIDA IN PARTIAL FULFILLMENT
OF THE REQUIREMENTS FOR THE DEGREE OF
DOCTOR OF PHILOSOPHY

UNIVERSITY OF FLORIDA

1990

ACKNOWLEDGEMENTS

I am grateful to Dr. M.D. Sacks, supervisory committee chairman, for his guidance and financial support during the course of this work. Especially, I appreciate him for his numerous suggestions and corrections during the preparation of this dissertation. Thanks should be given to Dr. D.E. Clark, Dr. R.T. DeHoff, Dr. C.T. Sun, and Dr. E.D. Whitney for their encouragement and advice.

I am also thankful to the Ministry of Education of the Republic of Korea for its financial support. I thank Mr. G.W. Scheiffele from the bottom of my heart for his help from day one in this work. Thanks go to Dr. Sun-Moo Her, Dr. C.S. Khadilkar, Dr. T.S. Yeh, Mr. S.D. Vora, Mr. O.E. Rojas, and Dr. A. Morrone for their fruitful discussion and technical help.

I would also like to extend my thanks to my family for their patience and encouragement.

TABLE OF CONTENTS

Pages

ACKNOWLEDGEMENTS.....ii

LIST OF TABLES.....vi

LIST OF FIGURES.....viii

CHAPTER

1 INTRODUCTION..... 1

2 LITERATURE SURVEY.....5

2.1 Review of Literature..... 5
2.1.1 Introduction..... 5
2.1.2 Limitation of Fiber-Reinforced Composites..... 6
2.1.3 Properties of Whisker Reinforced Composites..... 12
2.1.4 Processing and Processing Defects of Whisker Composites..... 17
2.1.4.1 Impurity and its related defects..... 20
2.1.4.2 Whisker clusters and associated large pores..... 23
2.1.4.3 Agglomerates..... 24
2.2 Theoretical Background..... 27
2.2.1 Toughening Mechanism by Whisker Reinforcement..... 27
2.2.1.1 Crack deflection..... 27
2.2.1.2 Whisker bridging..... 33
2.2.1.3 Whisker pull-out..... 36
2.2.1.4 Multiple toughening mechanism..... 38
2.2.2 Thermochemical Stability..... 40
2.2.3 Constrained Sintering..... 46
2.2.3.1 Viscoelastic model..... 46
2.2.3.2 Network (percolation) model..... 54
2.2.3.3 Contact probability argument..... 62
2.2.4 Green Microstructure Control..... 64
2.2.4.1 Control of powder characteristic..... 64
2.2.4.2 Suspension processing..... 66
2.2.4.3 Packing of whisker/particle mixture... 72
2.2.5 Infiltration of Liquid into Porous Compact..... 76
2.2.5.1 Kinetics of infiltration..... 77
2.2.5.2 Melting and decomposition of ANN..... 78

2.2.6 Liquid Phase Sintering..... 79
2.2.6.1 Rearrangement..... 80
2.2.6.2 Solution-reprecipitation process..... 83
2.2.6.3 Application of LPS to Al_2O_3/SiC whisker composites..... 85
2.3 Strategies..... 86

3 EXPERIMENTAL PROCEDURE..... 89

3.1 Powder Preparation and Characterization..... 89
3.1.1 Alumina Powder Preparation..... 89
3.1.2 SiC Whisker Preparation..... 91
3.1.3 MgO and Y_2O_3 Preparation..... 93
3.1.4 Characteristics of Powders..... 94
3.2 Suspension Preparation..... 96
3.2.1 Electrokinetic Measurement..... 96
3.2.2 Characterization of Suspensions..... 97
3.3 Green Body Preparation and Characterization..... 98
3.3.1 Optimization of Consolidation Condition..... 98
3.3.2 Green Body Infiltration..... 100
3.3.3 Characterization of Green Body..... 101
3.4 Sintering..... 102
3.5 Properties and Microstructures..... 103

4 RESULTS AND DISCUSSIONS..... 106

4.1 Powder Characterization..... 106
4.1.1 Al_2O_3 Powder..... 106
4.1.2 SiC Whisker..... 111
4.1.3 Sintering Additives and Infiltrant..... 122
4.2 Suspension Characteristics..... 127
4.2.1 Al_2O_3 Suspension..... 127
4.2.2 SiC Whisker Suspension..... 135
4.2.3 Characteristics of Composite Suspensions... 143
4.3 Green Body Characteristics..... 150
4.3.1 Consolidation Conditions..... 150
4.3.2 Dry Pressing vs. Suspension Processing..... 155
4.3.3 Effect of Whisker Aspect Ratio..... 161
4.3.4 Effect of Matrix Particle Size..... 166
4.3.5 Effect of Sintering Additives..... 174
4.3.6 Infiltration of Matrix Precursor..... 179
4.4 Densification and Microstructure..... 190
4.4.1 Dry Processing vs. Suspension Processing... 190
4.4.2 Effect of Sintering Atmosphere on Densification of Composites..... 192
4.4.3 Effect of Whisker Aspect Ratio..... 195
4.4.4 Effect of Matrix Particle Size..... 201
4.4.4.1 Densification of Al_2O_3 without SiC whiskers..... 201
4.4.4.2 Densification Behavior of Composite... 206
4.4.4.3 Microstructure Characterization..... 218
4.4.5 Effect of Sintering Additives..... 244
4.4.6 Effect of Green Body Infiltration..... 257

5 CONCLUSIONS..... 273
APPENDIX.....276
REFERENCES.....283
BIOGRAPHICAL SKETCH..... 299

LIST OF TABLES

Table		Page
2.1	Comparison of critical flaw sizes (μm) of monoliths and their composites reinforced with 20 vol% SiC whiskers	20
2.2	Critical exponents controlling the near-threshold scaling behavior of key quantities in percolation [Zal83]	58
2.3	Critical concentration for bond and site percolation on a variety of lattices [Zal83]	59
3.1	Suspension solids loading for slip casting	99
3.2	Thermal etching conditions for various samples	103
4.1	Characteristics of Al_2O_3 powders	107
4.2	Characteristics of SiC whiskers	112
4.3	Calculated surface area and length-averaged whisker length	113
4.4	Cation impurities of whisker obtained by ICP	120
4.5	Characteristics of sintering additives	123
4.6	Rheological and porosimetry results of Al_2O_3 suspension	130
4.7	Sediment density for SiC whisker suspensions	137
4.8	Packing efficiency based on bimodal packing theory	160
4.9	Effect of sintering conditions on densification and weight loss	193
4.10	Green microstructural characteristics of green compacts prepared with different whisker aspect ratios	197

4.11 Percent weight loss for samples prepared with TSC-A (L/D=21) and TSC-C (L/D=14)..... 200

4.12 Relative sintering driving force for the samples prepared with alumina-10 powder..... 217

4.13 Specific surface area of 70 vol% Al_2O_3/30 vol% SiC whisker composites..... 239

4.14 Sintering parameter of the samples with and without infiltration..... 262

LIST OF FIGURES

Figures		Page
2.1	Plots of high temperature fracture strength vs. test temperature for SiC whisker-reinforced (20 vol%) composites with various matrix materials (Al_2O_3 [Tie87], Si_3N_4 [Bul87a], 3Y-TZP [Cla86]) and for LAS glass-ceramic reinforced with 44 vol% SiC fiber [Pre86]	10
2.2	Plots of fracture toughness vs. SiC whisker content for various matrix materials: Al_2O_3 [Tie87], α-Si_3N_4 [Sha86a], β-Si_3N_4 [Sha86a], 3Y-TZP [Cla86], mullite [Wei85]	14
2.3	Comparison between strength values measured and calculated from fracture toughness for SiC whisker-reinforced composites (same reference as Fig. 2.2 except codierite [Cla86])	18
2.4	Crack-dispersoid interactions. (A) Schematic of interaction of crack with dispersoid in hydrostatic tension (e.g. due to $\alpha_d > \alpha_m$): (B) with dispersoid in hydrostatic compression (e.g. due to $\alpha_d < \alpha_m$)	29
2.5	Theoretical predictions of composite toughening by dispersoids of various shapes [Fab83]	31
2.6	The presence of a whisker bridging zone behind the crack tip modifies the crack opening displacement. In the presence of bridging whiskers, closure forces and stresses are imposed on the crack surfaces	33
2.7	Plots of fracture toughness increment vs. SiC whisker volume fraction for various matrix materials	36
2.8	Plots of equilibrium P_{CO} vs. temperature for the reaction between SiC and surface SiO_2	43
2.9	Plots of equilibrium partial pressure of CO gas vs. temperature for the decomposition	

reaction of Al_2O_3 and SiO_2..... 44

2.10 A rigid inclusion in a sintering matrix. Compressive radial stress (σ_r) and tensile circumferential stresses (σ_θ=σ_ϕ) are generated in the matrix..... 47

2.11 Qualitative sketch of potential energy curve versus separation between parallel plates..... 71

2.12 Packing curve for fibers with varied L/D ratios [Mil86]..... 73

2.13 Theoretical packing of whisker-particulate system [Mil86]..... 74

4.1 Cumulative plot of equivalent spherical particle size for (A) alumina-7, -8, and -11, and (B) alumina-10 and -27 powders..... 109

4.2 Particle size distribution plotted on a log-probability scale for alumina-7, -8, -10, and -27 powders..... 110

4.3 Scanning electron micrographs of the TSC-F whiskers prepared by (A) dry sampling and (B) wet sampling..... 115

4.4 Histogram plot of whisker diameter for TSC-F whisker on number basis..... 117

4.5 Histogram plots of whisker length for TSC-F whisker in (A) number-based and (B) length-based distributions..... 118

4.6 Histogram plots of whisker length for (A) TSC-A, (B) TSC-B, and (C) TSC-C on length-base distribution..... 119

4.7 Cumulative plots of equivalent spherical diameter for MgO and Y_2O_3..... 124

4.8 Plots of TG and DTA analyses for ANN..... 126

4.9 Plot of zeta potential as a function of pH for alumina..... 128

4.10 Plots of relative density and median pore channel radius as a function of the concentration of Tamol 901 at pH=11..... 132

4.11 Plots of suspension viscosity vs.

ultrasonication time for 50 vol% solid (alumina-7) loadings at pH=4..... 133

4.12 Plots of (A) green relative density and (B) median pore channel radius as a function of ultrasonication time..... 133

4.13 Plot of zeta potential of SiC whisker (TSC-C) as a function of pH..... 136

4.14 Plots of suspension viscosity vs. shear rate for suspensions prepared with washed and as-received whiskers with 3 and 8 vol% solids loading..... 139

4.15 Plots of suspension viscosity vs. shear rate for the suspensions prepared with various dispersant concentrations..... 141

4.16 Plots of viscosity vs. shear rate for suspensions containing 50 vol%solids and varying Al_2O_3 (alumina-8)/SiC whisker (TSC-C) volume ratios..... 144

4.17 Plots of viscosity vs. shear rate for 50 vol% composite suspensions with TSC-A (L/D~21) and TSC-C (L/D~14) whiskers..... 146

4.18 Plots of viscosity vs. shear rate for TSC-F SiC whisker/alumina-10 suspensions containing 45 vol% total solids and varying concentrations of SiC whiskers..... 148

4.19 Plots of specific pore volume frequency vs. pore channel radius obtained by mercury porosimetry for (A) slip-cast and low-speed centrifugally cast samples prepared using suspensions with 18 vol% solids, (B) slip-cast and low-speed centrifugally cast samples prepared using suspensions with 54 vol%..... 152

4.20 Scanning electron micrographs showing (A) depletion of SiC whiskers (ASC-F) near the top surface and (B) accumulation of SiC whiskers near the bottom surface of a low-speed centrifugally cast sample prepared using suspensions with 18 vol% solids.....153

4.21 Scanning electron micrographs showing a uniform distribution of SiC whiskers (ASC-F) in a slip-cast composite sample prepared using a suspension with 54 vol% solids: (A) region near the top surface and (B) region near the

bottom surface of the sample..... 154

4.22 Plots of green relative density vs. SiC whisker content for Al_2O_3 (alumina-8)/SiC whisker (TSC-B) samples prepared by slip casting and dry pressing..... 157

4.23 Plots of specific pore volume frequency vs. pore channel radius obtained by mercury porosimetry for Al_2O_3 (alumina-8)/SiC whisker (TSC-B) samples prepared by slip casting and dry pressing..... 158

4.24 Plots of relative green density vs. vol% TSC whiskers for slip-cast samples prepared with different SiC whisker size fractions..... 162

4.25 Plots of specific pore volume frequency vs. pore channel radius obtained by mercury porosimetry for Al_2O_3, SiC whisker, 70 vol% Al_2O_3 (alumina-8)/30 vol% SiC whisker (TSC-B) compacts prepared by slip casting..... 163

4.26 Plots of specific pore volume frequency vs. pore channel radius obtained by mercury porosimetry for slip-cast compacts containing various ratios of Al_2O_3 (alumina-8)/SiC whiskers (TSC-C)..... 164

4.27 Plot of green relative density vs. SiC whisker content for SiC whisker containing composites. Comparisons are made with composites prepared with pressure filtration [Por87] and CIP [Lun87; Tie87]..... 165

4.28 Plots of relative green density vs. SiC whisker content for samples prepared with alumina-10 and alumina-27 powders..... 167

4.29 Plots of median pore channel radius vs. SiC whisker content for samples prepared with alumina-10 and alumina-27 powders..... 169

4.30 Plots of specific pore volume frequency vs. pore channel radius obtained by mercury porosimetry for the samples prepared with alumina-10..... 170

4.31 Plots of specific pore volume frequency vs. pore channel radius for the samples prepared with alumina-27..... 171

4.32 Scanning electron micrographs of the top

surface of 70 vol% Al_2O_3 (alumina-10)/30 vol% SiC whisker (TSC-F) green compact: (A) low magnification and (B) high magnification..... 172

4.33 Scanning electron micrographs of the top surface of 70 vol% Al_2O_3 (alumina-27)/30 vol% SiC whisker (TSC-F) green compact: (A) low magnification and (B) high magnification..... 173

4.34 Plots of (A) relative green density and (B) median pore channel radius vs. SiC whisker content for alumina-10/TSC whisker compacts prepared with and without sintering additives... 175

4.35 Plots of specific pore volume frequency vs. pore channel radius for the samples prepared with sintering additives and varying SiC whisker (TSC-F)/alumina-10 ratios..... 177

4.36 Scanning electron micrographs of the top surface of 70 vol% Al_2O_3-10/30 vol% TSC-F whisker compact prepared with sintering additives: (A) low magnification and (B) high magnification..... 178

4.37 Plot of average fractional weight gain as a function of number of infiltration cycles..... 180

4.38 Plot of filling efficiency vs. number of infiltration cycles..... 181

4.39 Plots of green relative density vs. SiC whisker content for the samples infiltrated with ANN.... 184

4.40 Plot open porosity vs. SiC whisker content for the samples infiltrated with ANN..... 187

4.41 Plots of median pore channel radius vs. SiC whisker content for compacts with and without infiltration..... 188

4.42 Plots of specific pore volume frequency vs. pore channel radius for the samples infiltrated with ANN after decomposition at 900°C..... 189

4.43 Plots of relative density vs. SiC whisker content for the samples prepared by dry-pressing and slip casting..... 191

4.44 Plots of relative density vs. sintering temperature for the samples prepared with whisker aspect ratios of 14 and 21 at whisker concentration of (A) 5 vol%, (B) 15 vol%, and (C) 30 vol%..... 196

4.45 Plot of relative density vs. sintering temperature for the alumina-10 samples..... 202

4.46 Scanning electron micrographs showing the changes in grain and pore microstructures for pure alumina-10 samples sintered at (A) 1250°C, (B) 1500°C, (C) 1700°C, and (D) 1800°C... 204

4.47 Plots of relative density vs. sintering temperature for samples prepared with alumina-10 and -27 powders and with varying Al_2O_3/SiC whisker ratios: (A) 5 vol% SiC/95 vol% Al_2O_3, (B) 15 vol% SiC/85 vol% Al_2O_3, and (C) 30 vol% SiC/70 vol% Al_2O_3..... 207

4.48 Plots of open porosity vs. sintering temperature for samples prepared with varying Al_2O_3/SiC whisker ratio and with different matrix particle sizes: (A) alumina-27 and (B) alumina-10..... 208

4.49 Plots of sintered relative density vs. SiC whisker content for samples sintered at 1250 and 1500°C. Samples were prepared with alumina-10 powder..... 210

4.50 Comparison of the parameter a calculated from the present study and obtained by Lange from the work by DeJonge and coworkers [Lan87]..... 213

4.51 X-ray diffraction pattern for the 30 vol% SiC whisker composite prepared with the alumina-27 powder and sintered at 1800°C (A=α-Al_2O_3, S=SiC)..... 219

4.52 Transmission electron micrographs of 85 vol% Al_2O_3-10/15 vol% TSC-F SiC whisker sample sintered at 1800°C..... 221

4.53 Plots of average grain intercept size vs. sintering temperature for samples prepared with varying Al_2O_3/SiC whisker ratio. Samples were prepared with alumina-10 powder..... 222

4.54 Plots of average grain intercept size vs. sintering temperature for pure alumina-10 powder compacts..... 224

4.55 Scanning electron micrographs showing 70 vol% Al_2O_3/30 vol% SiC whisker samples (A) before

and (B) after sintering at 1250°C (30 min). Samples are prepared with alumina-10 powder..... 227

4.56 Scanning electron micrographs showing 70 vol% /30 vol% SiC whisker samples (A) before and (B) after sintering at 1250°C (30 min). Samples are prepared with alumina-27..... 228

4.57 Scanning electron micrographs for the composites prepared with alumina-10 at the sintering temperature of 1250°C: (A) 5 vol%, (B) 15 vol%, and (C) 30 vol% whiskers..... 230

4.58 Scanning electron micrographs for the composites prepared with alumina-10 at the sintering temperature of 1500°C: (A) 5 vol%, (B) 15 vol%, and (C) 30 vol% whiskers..... 231

4.59 Scanning electron micrographs for the composites prepared with alumina-10 at the sintering temperature of 1700°C: (A) 5 vol%, (B) 15 vol%, and (C) 30 vol% whiskers..... 232

4.60 Scanning electron micrographs for the composites prepared with alumina-10 at the sintering temperature of 1800°C: (A) 5 vol%, (B) 15 vol%, and (C) 30 vol% whiskers..... 233

4.61 Scanning electron micrographs for the composites prepared with alumina-27 at the sintering temperature of 1250°C: (A) 5 vol%, (B) 15 vol%, and (C) 30 vol% whiskers..... 234

4.62 Scanning electron micrographs for the composites prepared with alumina-27 at the sintering temperature of 1500°C: (A) 5 vol% and (B) 15 vol% whiskers..... 235

4.63 Scanning electron micrographs for the composites prepared with alumina-27 at the sintering temperature of 1700°C: (A) 5 vol% and (B) 15 vol% whiskers..... 236

4.64 Scanning electron micrographs for the composites prepared with alumina-27 at the sintering temperature of 1800°C: (A) 5 vol%, (B) 15 vol%, and (C) 30 vol% whiskers..... 237

4.65 Plots showing relative density for composite samples determined by the Archimedes displacement method and quantitative microscopy measurement of the pore volume fraction. The straight line

represents the ideal case where the two methods of measurement give the exact same value..... 238

4.66 Plots of average grain intercept size vs. sintering temperature for samples prepared with varying Al_2O_3/SiC whisker ratio. Samples were prepared with the alumina-27 powder..... 241

4.67 Plots of relative density vs. SiC whisker content for the samples prepared with and without sintering additives and sintered at (A) 1700 and (B) 1800°C..... 245

4.68 Comparison between the relative density values determined by Archimedes method and point counting. The straight line represents the ideal case..... 247

4.69 Plots of the optimum sintered density vs. SiC whisker content for samples with sintering additives. The results are compared with the results reported by Tiegs and Becher [Tie87].... 248

4.70 Scanning electron micrographs of the samples prepared with sintering additives and sintered at 1700°C with (A) 5 vol% and (B) 15 vol% whiskers..... 250

4.71 Scanning electron micrographs of the samples prepared with sintering additives and sintered at 1800°C with (A) 5 vol% and (B) 15 vol% whiskers..... 251

4.72 X-ray diffraction patterns for the samples with 15 vol% whiskers and sintered at (A) 1700 and (B) 1800°C..... 253

4.73 EDS spectra for the 15 vol% whisker composite sample sintered at 1800°C at different sensitivities..... 255

4.74 Plots of grain intercept size vs. SiC whisker content for samples prepared with and without sintering additives..... 256

4.75 Plots of relative density vs. SiC whisker content for samples prepared with and without infiltration and sintered at 1700 and 1800°C.... 258

4.76 Comparison between the relative density values determined by Archimedes method and point counting. The straight line represents the

ideal case where the two methods of measurement give the exact same value..... 261

4.77 Plots of open porosity vs. SiC whisker content for samples prepared with and without infiltration and sintered at 1800°C..... 264

4.78 Plots of average grain intercept size vs. SiC whisker content for samples prepared with and without infiltration and sintered at 1800°C.....265

4.79 Comparison of maximum measured grain size with the predicted limiting grain size determined by Zener's relation..... 267

4.80 Plots of indentation fracture toughness vs. SiC whisker content for the samples prepared with and without infiltration and sintered at 1800°C..... 269

4.81 Scanning electron micrograph showing significant whisker pull-out lengths which indicate that the interfacial strength is weak..... 270

4.82 Plots of hardness vs. SiC whisker content for the infiltrated samples sintered at 1800°C. Measured hardness values are compared with the theoretical prediction..... 271

A.1 Particle size distribution plots for various alumina obtained by X-ray sedigraph..... 281

A.2 Particle size distributions for SiC whiskers obtained by X-ray sedigraph..... 282

Abstract of Dissertation Presented to the Graduate School of the University of Florida in Partial Fulfillment of the Requirements for the Degree of Doctor of Philosophy

SUSPENSION PROCESSING AND PRESSURELESS SINTERING OF SILICON CARBIDE WHISKER-REINFORCED ALUMINA-MATRIX COMPOSITES

By

HAE-WEON LEE

May, 1990

Chairman: Dr. Michael D. Sacks
Major Department: Materials Science and Engineering

The effects of processing variables (e.g. matrix particle size, size distribution, SiC whisker content, whisker aspect ratio, suspension pH, etc.) on green microstructures were investigated in suspension processing. Homogeneous Al_2O_3 powder/SiC whisker compacts were prepared by suspension processing. Green bodies with high relative density (~65-71%) fine median pore size (~10-50 nm) were obtained with SiC whisker contents in the range of 5 to 30 vol%. The green density obtained by suspension processing was only dependent upon dispersion condition regardless of other processing variables, while median pore size was very sensitive to all the variables.

Pressureless sintering of suspension processed SiC whisker-reinforced Al_2O_3 composites was investigated. The effects of the aforementioned processing variables on

densification behavior and microstructure development are reported. Although liquid phase sintering, reducing matrix particle size or whisker aspect ratio, green body infiltration all enhanced densification of composites, the infiltration approach was more effective for samples with high SiC whisker concentrations. Samples with 27 vol% whiskers could be pressurelessly sintered to ~93% relative density and ~3% open porosity.

CHAPTER 1
INTRODUCTION

There has been a great deal of effort to develop high performance ceramic materials for high temperature applications such as heat engines. However, ceramic materials have relatively high sensitivity, compared with metals, to flaws and accidental surface damage. Thus, low fracture toughness values and low Weibull moduli for fracture strength are observed relative to metals.

In order to improve mechanical properties of ceramic materials, two approaches have received a great deal of attention: (1) increasing fracture toughness using fiber-reinforcement or transformation toughening (composite approach), (2) minimizing strength-degrading defects through improved processing (e.g., elimination of agglomerates, pressure sintering, etc.). Although significant improvements in physical properties have been achieved in recent years through these approaches, further advances in processing are needed to develop ceramics with the desired level of reliability for structural applications.

It is well-known that the presence of fully dense rigid inclusions (e.g., SiC whiskers) can significantly retard densification of a matrix material (e.g., Al_2O_3). In composites with low concentration of inclusions, several

explanations have been given for the substantial decrease in densification rate, including (1) the development of hoop tensile stresses in the matrix which resist the sintering stress and (2) the increase in the transport path length for diffusion. At higher inclusion concentrations, a rigid network may develop in the composite which resist matrix deformation under the sintering stress. Due to these adverse effects on densification, SiC-whisker-reinforced composites are generally prepared by hot pressing. However, hot pressing has several limitations: (1) it is extremely difficult to fabricate complex shapes, which results in high cost if a subsequent machining step is required; (2) hot pressing techniques are inefficient in mass production of ceramic articles such as engine parts (thus, it is desirable to sinter pressurelessly to high densities the green composites fabricated into complex shapes by forming methods such as slip casting, injection molding, or extrusion); (3) hot pressing results in preferred orientation of whiskers which leads to a restricted design of articles due to anisotropic physical properties.

In the present study, pressureless sintering of SiC whisker-reinforced Al_2O_3 composites was investigated using techniques which result in improved green microstructures. The primary objective of this research was to test the applicability of colloidal processing science to SiC whisker/Al_2O_3 composites, to identify the effects of critical processing variables on pressureless sintering of the

composites, and finally to investigate the properties and microstructure of these sintered composites.

Powder characteristics were tailored in order to achieve desired final microstructure and properties. The final microstructures and properties are significantly affected by the green microstructure. Especially in the composites containing non-sinterable, inert, rigid inclusions, the green microstructure control can determine the achievable final end-point density, and consequently, the final properties. Desired green microstructural characteristics are high density, small pore channel radius, and high homogeneity. Most high performance ceramic materials are fabricated using submicrometer powders, such that a 1 cm^3 specimen will contain 10^{12}-10^{15} particles. It is almost impossible to achieve green compacts with the aforementioned green microstructures without controlling interparticle behavior. This can be accomplished well using colloidal processing.

In addition to improving the green microstructure by colloidal processing, several other approaches were investigated in order to enhance densification of the composites. These approaches include liquid phase sintering of suspension-processed green compacts, reducing whisker aspect ratio, and sintering the green compacts which had been subjected to an infiltration process in order to increase green density. Even with the green compacts with high density, small pore size, homogeneous microstructure, it is important to control sintering variables, since SiC carbide

whiskers are unstable under some sintering conditions. The effect of sintering time, temperature, and atmosphere was investigated.

Sintered microstructures were studied using various techniques including SEM, TEM, EDS, XRD, etc. Fracture toughness was evaluated and compared with the results obtained by other processing techniques.

Theories and experimental studies relevant to this investigation are reviewed with regard to aforementioned approaches in Chapter 2. This review is followed in Chapter 3 by a description of the experimental procedures. The results and discussion are presented in Chapter 4. Conclusions are drawn in Chapter 5.

CHAPTER 2
LITERATURE SURVEY

2.1. Review of Literature

2.1.1 Introduction

Monolithic ceramic materials including SiC, Si_3N_4, Al_2O_3, and mullite have fracture toughness of the order of 3 to 5 $MPa \cdot m^{1/2}$. As the result of this low fracture toughness, it is necessary to fabricate parts with very small flaw sizes (< 50 μm) to achieve acceptable fracture strength (> 800 MPa) for structural applications. According to the Griffith formula,

$$\sigma_f = Y \frac{K_{Ic}}{\pi\sqrt{c}} \tag{2.1}$$

where σ_f is fracture strength, Y is a geometric factor, K_{Ic} is the critical fracture toughness, and c is critical flaw size, improved toughness can result in increased strength for a constant flaw size. In addition, improved K_{Ic} can enhance resistance to slow crack growth and strength degradation from thermal shock [Tie86]. Fiber* reinforcements, either continuous or discontinuous, can be used to obtain both strengthening and toughening of a brittle matrix. The development of fiber-reinforced ceramic-matrix composites has been limited by the availability of appropriate fibers. The

---

* According to Levitt [Lev70], a fiber is defined as any material in an elongated form such that it has a minimum length to a maximum average transverse dimension of 10:1. On the other hand, a whisker is any material that fits the definition of a fiber and is a single crystal.

main aim in the development of such composites has been increased toughness without the loss, at elevated temperature, of attractive structural characteristics and oxidation resistance of the unreinforced ceramic. Two different approaches have been investigated. One has been, in analogy with the development of conventional fiber composites, to utilize the high strength and stiffness of the fiber by producing composites with high volume fractions of continuous fibers. In this case, the matrix is of secondary importance to strength but imparts its elevated temperature characteristics. The other has been to incorporate modest amount of short fibers (whiskers or chopped fibers) in order to produce a composite which should, to a great extent, reflect the properties of the monolith, but with considerably improved toughness.

In the following, we will review the recent development and improvement of fiber-reinforced ceramic matrix composites, their processing techniques and problems. The review will focus mainly on SiC fiber (continuous or whisker type) reinforced ceramic polycrystalline matrix composites since improvement in high temperature properties is one of the most important goals in developing ceramic matrix composites.

2.1.2 Limitation of Fiber-Reinforced Composites

Glass and glass-ceramic composites reinforced with carbon- [Sam72a, Sam72b] and SiC-fibers [Pre82, Bre82, Lam86, Sin88, Mah85, Her86, Cap87] have shown good mechanical

properties at moderately high temperatures (<1200°C). From the viewpoint of composite fabrication, the glass-matrix composites, as compared to polycrystalline ceramic candidates, probably offer the greatest commercial potential due to an ease of densification, low cost and also excellent performance up to moderate temperature range (~800°C in air). The attributes are listed below [Pre86].

(1) Fiber-matrix interface reactions can be readily controlled due to wide range of glass compositions.

(2) Residual interfacial shear and radial stresses can be easily tailored to control the composite properties using the glasses with various thermal expansion coefficients.

(3) The ability to control the viscosity of glasses and deform them easily under pressure permits the physical densification of fiber reinforced composites without mechanical damage to the fibers. Therefore, relatively high fiber content can be incorporated into the matrix,

Although such composites have impressive mechanical properties at ambient temperature (K_{Ic} >10 MPa·$m^{1/2}$ and σ_f >700 MPa), they suffer from the problems of oxidation of fibers and reactions of fibers with matrix materials at elevated temperatures, even with SiC fibers which are more resistant to oxidation and thermal degradation compared to carbon or graphite fibers. Recently, Prewo and Brennan [Pre82] demonstrated that substantial increases in the fracture toughness of spodumene glass ceramics and borosilicate glass can be achieved by reinforcing with continuous

microcrystalline fibers, i.e, Nicalon SiC fibers. They reported toughness up to 20 $MPa \cdot m^{1/2}$ and strength approaching 850 MPa. Later, the same authors [Bre82] reported bend strengths over 700 MPa and fracture toughness values of greater than 17 $MPa \cdot m^{1/2}$ from room temperature to 1000°C in argon for SiC yarn reinforced lithium aluminosilicate (LAS) glass-ceramic composite system with a carbon rich interface. (Such an interface facilitates debonding. Toughening mechanisms involved in the continuous fiber composites are fiber bridging, crack deflection, and extensive fiber pull-out. In order to maximize the occurrence of toughening by these mechanisms, the interface of composites must satisfy the condition for debonding of fiber-matrix interface.) However, this composite also presented oxidation problems during heat treatment in air at high temperatures. For example, the oxidation of SiC fibers produced large surface holes evolving either volatile SiO and/or CO gas by the reaction between the SiO_2 and excess carbon. Also, excessive grain boundary sliding (due to the glassy SiO_2) is another concern for high temperature applications.

Despite the success of fiber-reinforced glass, glass-ceramic matrix composites at moderate temperature range, processing difficulties in fiber-reinforced polycrystalline matrix composites (resulting in non-uniform distribution of fibers, mechanical and chemical degradation of fiber properties and incomplete densification of the matrix) have limited the strength of these composites. The continuous

fiber-reinforced composites investigated so far have been unable to fully satisfy the requirements for high temperature applications such as high temperature strength, fracture toughness, thermal shock resistance. In particular, the strength values obtained in air at high temperatures are very disappointing.

However, it is noteworthy that very high fracture toughness (25 $MPa \cdot m^{1/2}$) was obtained for SiC/SiC (Nicalon fiber) composites prepared by CVI (chemical vapor infiltration) [Cap87]. The high fracture toughness results from rapid subdivision of the original crack into many microcracks, requiring a much larger energy for crack growth. Despite the remarkable increase in fracture toughness, the bend strength was only in the range of 300-400 MPa up to ~1250°C and decreased drastically above 1250°C. This is probably due to the large amount of residual open porosity (~10%) which can be an ideal channel of O_2 gas transport to the fibers. As mentioned earlier, exposure of continuous SiC fiber composites to air at the elevated temperatures may lead to oxidation of the fibers, reaction between the fibers and the matrix, and subsequent gas evolution (CO, SiO). The resulting interface, consisting of oxides, nitrides, carbides (either separately or in combination), invariably have high fracture resistance so that desirable composite properties are not retained [Evan88]. Singh and Gaddipati [Sin88] improved flexural strength from 202-271 MPa for monolith mullite to 646-855 MPa for mullite containing 25 vol% SiC

fibers (AVCO) by controlling interface with a BN coating. Fracture toughness was increased approximately 2-fold with a BN coating on the SiC fibers. However, the high temperature mechanical properties were not reported.

Figure 2.1 shows the high temperature strength of lithium aluminosilicate glass ceramic reinforced with 44 vol% SiC fibers compared to those of various whisker composites (20 vol% SiC whisker content).

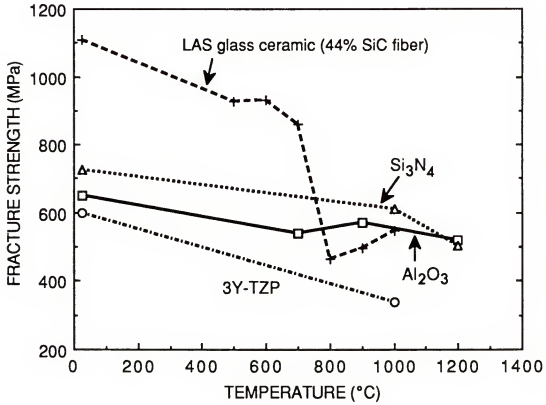

Figure 2.1 Plots of high temperature fracture strength vs. test temperature for SiC whisker-reinforced (20 vol%) composites with various matrix materials (Al_2O_3 [Tie87], Si_3N_4 [Bul87a], 3Y-TZP [Cla86]) and for LAS glass-ceramic reinforced with 44 vol% SiC fiber [Pre86].

All the samples have alignment of fibers or whiskers perpendicular to hot-pressing axis. The strength values in Figure 2.1 are those obtained by applying the load perpendicular to the plane with the aligned fibers or whiskers (i.e., the plane perpendicular to hot-pressing axis). This gives maximum strength. The LAS composite strength at high temperature decreased to the stress level at which matrix cracking begins to occur. The air then penetrates into composite and attacks the low strength carbon rich fiber-matrix interface in such a way as to cause an catastrophic failure without any strengthening. Another feature of the Figure 2.1 is that the whisker composites are more stable at elevated temperatures compared to continuous SiC fiber reinforced composites due to matrix refractoriness and the stability of SiC whiskers at high temperatures. However, 3Y-TZP matrix composite reinforced with 20 vol% SiC whiskers showed lower strength at room temperature compared to monolith 3Y-TZP (σ_f ~ 1100 MPa). The decrease in fracture strength can be attributed to the high tensile matrix stresses due to the thermal mismatch (4 vs. 11 $\times 10^{-6}$ K^{-1}). The situation is markedly different at high temperatures. At 1000°C, the strength of whisker composite was nearly twice that of the 3Y-TZP matrix. The thermal mismatch stresses are much lower than at room temperature and the interfacial layer has softened to the extent that more whisker pull-out can take place. Similarly, most whisker composites have

relatively high fracture strength at high temperature due to the effective load transfer between whisker and matrix.

2.1.3 Properties of Whisker Reinforced Composites

Since the high temperature properties of fiber reinforced composites were somewhat mediocre, other attempts have been undertaken to enhance fracture toughness and high temperature strength by whisker reinforcements. The thermal stability of the SiC whiskers in ceramic matrices at processing temperatures up to 1900°C [Bul87b, Hom87] is a distinct advantages over continuous microcrystalline SiC fibers that typically degrade above 1250°C [Mah84]. Thermal stability of SiC whiskers is excellent at elevated temperatures apparently because (1) they are single crystals and, therefore, do not degrade at T>1200°C by the grain growth that commonly occurs in microcrystalline continuous SiC fibers like Nicalon, and (2) they have very low content of oxygen and, therefore, decomposition of fibers and/or reactions between the fibers and matrix are less likely. In the case of Nicalon fibers, it is reported [Yaj79] that the atomic ratio of SiC fibers after pyrolysis (1300°C) of the precursor fiber is Si:C:O:H = 1:1.46:0.36:0.03. Thus, the as-received fiber contains a considerable amount of excess carbon and oxygen. The high oxygen content necessitates the use of fiber surface coating in composites prepared with oxide matrices in order to minimize interfacial reaction.

Mah et al.[Mah84] have observed that the Nicalon fiber strength degraded, regardless of heat-treatment conditions,

when the fibers were subjected to temperatures higher than 1200°C. This degradation was associated with β-SiC grain growth and evaporation of CO. The tensile strength of as-received Nicalon fiber was reported to be ~1.7 GPa but it decreased to ~660 MPa at 1200°C in air. The elastic moduli were 106 and 110 GPa at room temperature and 1200°C, respectively. On the other hand, reported values [Pet85] for long SiC whiskers (~5 mm gauge length) indicate that average tensile strengths of ~8.5 GPa and elastic moduli of ~700 GPa can be obtained. The oxygen content in the SiC whiskers was estimated to be less than 1 weight percent which is much less than that of Nicalon fibers (11.2 weight percent).

Becher and Wei [Becher84], Wei and Becher [Wei85], and Tiegs and Becher [Tie86, 87a, 87b, Bec88] demonstrated that the fracture toughness of polycrystalline ceramics can be significantly improved by reinforcing them with high strength SiC whiskers. For Al_2O_3 with 20 vol% SiC whiskers, the fracture toughness increased to 8 to 10 $MPa \cdot m^{1/2}$ for the planes perpendicular to the hot pressing axis and to ~5.6 $MPa \cdot m^{1/2}$ for the planes parallel to hot pressing axis. (Whiskers tend to be aligned perpendicular to hot pressing direction.)

Studies of the crack propagation behavior in the SiC whisker-reinforced ceramics reveal that the toughening mechanisms mainly involve (1) whiskers that bridge the crack just behind the crack tip and thus affect a crack closure

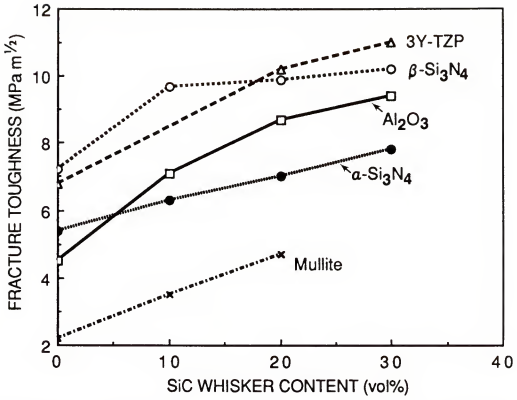

Figure 2.2 Plots of fracture toughness vs. SiC whisker content for various matrix materials: Al_2O_3 [Tie 87], α-Si_3N_4 [Sha86a], β-Si_3N_4 [Sha86a], 3Y-TZP [Cla 86], mullite [Wei 85].

force and (2) deflection of the crack by the whiskers such that the crack is reflected out of the mode I fracture plane [Bec86, Ang86]. In addition, whisker pull-out, although limited in extent, accompanies the eventual failure of the bridging whiskers. These toughening mechanisms rely on the strength of the whiskers and its retention, the whisker-matrix interface properties, and the matrix properties [Bec 88b]. Furthermore, the increased fracture toughness is retained with increasing temperature in air up to ~1400°C in the SiC-whisker-reinforced alumina composites [Beche86,

Bec88], as opposed to transformation-toughened systems where the toughness is temperature dependent because of the thermodynamic character of transformation.

Similar increases in fracture toughness have been observed in a variety of other SiC-whisker-reinforced ceramics as summarized in Figure 2.2. For example, fracture toughness of mullite increased from 2.2 to 4.7 $MPa \cdot m^{1/2}$ with the addition of 20 vol% SiC whiskers, and to 5.6 $MPa \cdot m^{1/2}$ with the additions of 20 vol% SiC whiskers and 10 vol% tetragonal ZrO_2 [Wei85, Tie86, Cla86]. When compared at equivalent volume fractions of reinforcing phase, whisker-reinforced composites exhibit toughness values which are similar to those of continuous-fiber-reinforced ceramics. However, whisker-reinforced composites have the advantage of fabrication by more conventional powder processing techniques. In general, 2- to 4-fold increases in fracture toughness have been observed in most of the whisker-reinforced composites, the extent of which was strongly dependent on the matrix-whisker interface, and the whisker and matrix properties. With the addition of 20 vol% SiC whiskers, fracture toughness values were higher than 10 $MPa \cdot m^{1/2}$ for 3Y-TZP and β-Si_3N_4 matrix composites; even higher values were reported for three component composite (mullite/t-ZrO_2/ SiC whisker) due to the additive contribution from whisker reinforcement and ZrO_2 toughening [Tie86, Bech87].

The fracture strength of Al_2O_3 reinforced with 20 vol% SiC whiskers exhibited almost constant strength value up to

1100°C in air while, above 1200°C, a marked strength degradation occurs which is associated with creep (Figure 2.1). Crack nucleation and growth resulting from creep deformation also contributes to the loss in strength of samples. Creep deformation and crack generation may well be related to enhanced grain boundary creep in the alumina because of the presence of a glass phase. The formation of alumina-silicate glasses on the exposed surfaces occurs at elevated temperatures in air as a result of the oxidation of the SiC and subsequent reaction between silica and alumina. In addition, impurities present in the whiskers and the alumina powders appear to modify the glass formation and the properties of the glass and lower the temperature at which such creep is initiated [Bec88].

Thermal shock resistance for 20 vol% SiC whisker reinforced alumina composite is also excellent up to ΔT=900°C while strength of alumina drops abruptly at ΔT>400°C. Repeated thermal shock degrades strength slightly which is indicative of a fatigue effect. Improvement of thermal shock resistance is mainly attributable to the higher fracture toughness (8.3 $MPa \cdot m^{1/2}$ compared to 4-5 for alumina) rather than higher thermal conductivity (35.2 vs. 32.3 $W/(m \cdot K)$) or lower thermal expansion coefficient (7.35 x 10^{-6} versus 8.22 x $10^{-6}/°C$). After multiple thermal shock, microcracking occurs in the matrix around whiskers, but these microcracks interact with whiskers and do not coalesce into large cracks. The

crack arresting interactions may occur by mechanisms such as crack bridging [Tie87].

Early work by Chokshi and Porter[Cho85] demonstrated a substantial improvement in creep resistance when alumina was reinforced with SiC whiskers. Furthermore, they concluded that the applied creep stress was carried largely by the whisker reinforcements, and that the creep response of the whiskers controlled the creep of the composite. Further study by Lipetzky et al.[Lip88] showed that at low stress levels, the primary creep deformation mechanism was diffusional creep and grain boundary sliding, facilitated by viscous flow of intergranular silica glass. The silica glass originated primarily from the oxidation of SiC whiskers. At higher stresses, cavitation occurred within glass pockets at interfaces and grain boundaries, enabling matrix grains to separate from the whiskers and causing an increase in the creep rate. With increasing creep strain, cavities linked together and formed cracks, resulting in composite failure. The measured activation energy for steady-state creep was higher for the composite than for unreinforced alumina with a similar grain size, and the creep rates for the composite were much lower [Lip88].

2.1.4 Processing and Processing Defects of Whisker Composites

Despite greatly improved fracture toughness of whisker composites, the fracture strength values of these composites were lower than expected from the increase in fracture toughness values. The fracture strengths of such composites

are very sensitive to the degree of microstructural homogeneity (i.e., the uniformity of dispersion of the whiskers in the dense matrix, matrix microstructures, etc.), as pointed out by Becher and Wei [Becher84]. Figure 2.3 compares the measured fracture strength values with the values calculated from the improvement of fracture toughness for 20 vol% SiC whisker reinforced composites with the various matrix.

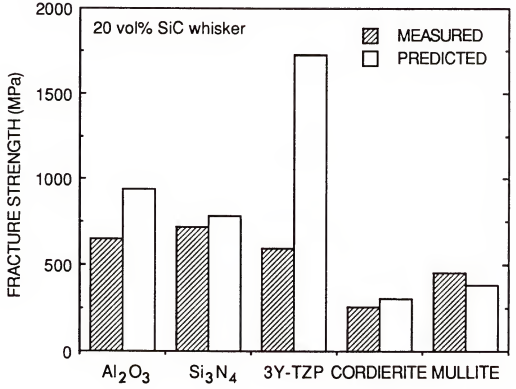

Figure 2.3 Comparison between strength values measured and calculated from fracture toughness for SiC whisker-reinforced composites (same reference as Fig. 2.2 except cordierite [Cla86]).

The calculated values were obtained using the Griffith equation (equation (2.1)) since most whisker composites

showed brittle failure [Evans86, Ken86, Bec88]. (The predicted values were obtained without taking into account the strengthening effects from the load transfer from matrix to whiskers.) For most composites, the measured strength values are slightly or considerably lower than those expected from the increase in fracture toughness by whisker reinforcements. This is partly because whisker (short fiber) has extremely limited load transfer capability due to short fiber length, compared to continuous fibers [Gad86]. However, fractographic analyses have demonstrated that the lower strength could be related to processing defects, which could have been avoided by beneficiation of starting powders and whiskers, proper mixing, and maintaining the mixed state during the consolidation step.

In Table 2.1, the critical flaw sizes of Griffith fracture for both monolithic matrices and 20 vol% whisker composite are compared. The processing steps for preparing materials are also summarized in the table. The critical flaw size for the alumina matrix composite increased from ~100 μm to ~220 μm with the addition of 20 vol% whiskers. On the other hand, the silicon nitride matrix composite had almost the same size of critical flaws. When we compare the processing routes for alumina and silicon nitride matrices, a distinct difference is that the whiskers were beneficiated by sedimentation before mixing. In the case of 3Y-TZP matrix composite, although the samples were fabricated in the same way as the cordierite matrix composite, the critical flaw

size for 3Y-TZP composite was much larger. This is due to microcracking caused by the large property mismatches (e.g., thermal expansion coefficient and elastic modulus) between the 3Y-TZP matrix and the SiC whisker.

Table 2.1 Comparison of critical flaw sizes (μm) of monoliths and their composites reinforced with 20 vol% SiC whiskers.

Matrix	Monolith	Composite	Processing Technique	Ref.
Al_2O_3	100.6	220.7	mixing with sonication, freeze drying, hot pressing	Wei85
Si_3N_4	46.2	54.0	sonication & sedimentation of whiskers, mixing with homogenizer, hot pressing	Bul87a
3Y-TZP	43.1	356.2	sedimentation of whiskers, tumbling mixing, hot pressing	Cla86
mullite	162.2	135.9	same as Al_2O_3	Wei85
cordierite	184.1	249.6	same as 3Y-TZP	Cla86

2.1.4.1 Impurity and its related defects. In whisker-reinforced composites, the major source of impurities is usually the SiC whiskers. Generally, it is proposed that the whiskers are fabricated from ground rice hulls by a vapor-liquid-solid (VLS) mechanism. Because of the short diffusion lengths and the thermal gradient, it is likely that solidification starts at the periphery of the solid/ liquid interface. Once nuclei form, they grow radially inward,

following the thermal gradient, and pushing the impurities in the liquid towards the center of the whisker. The highly impure front, containing the various impurities in the pyrolyzed rice hull, finally solidify at the central region, thus forming the core of the whisker [Far88].

The presence of impurities creates serious problems in some composite systems. There have also been reports that very large inclusions (up to ~250 μm diameter) were associated with the impurities in whiskers [Sha86a, Lun87]. Wei and Becher [Wei85] have also observed defects associated with impurities from SiC whiskers by electron microprobe analysis. The impurities were mainly Ca, Si, Al, Fe, and Cr which are quite common in SiC whiskers as a by-product of the whisker growth process.

Degradation of mechanical properties resulting from second phase inclusions is generally caused by residual stress, stress concentration, and degradation of matrix materials at the inclusion-matrix interface. Residual hydrostatic stress in the inclusion and large interfacial stresses may arise as a result of the mismatch in the thermal expansion coefficients of the matrix and inclusion. For a spherical inclusion in an infinite matrix, the residual stresses resulting from the property mismatch are given by [Sel61]

$$\sigma_r = -2\sigma_t = -\frac{(\alpha_m-\alpha_i)\ \Delta T}{\frac{1+\nu_m}{2+E_m} + \frac{1-\nu_i}{E_i}} \left(\frac{R}{r}\right)^3 \qquad (2.2)$$

where σ_r is residual stress, σ_t the tangential stress, α the thermal expansion coefficient, m and i refer to matrix and inclusion, respectively, ΔT is the difference between room temperature and the maximum temperature below which the stresses are not relaxed during cooling, ν is Poisson's ratio, E the elastic modulus, R the radius of the inclusion, and r is the radial distance from the inclusion. Depending on the property mismatches the residual stresses can be large enough to cause cracking of the matrix, if the inclusion size is equal to or greater than the critical size required for crack formation [Dav68]. In addition, for an inclusion with elastic constant different from those of the matrix material, a stress concentration will develop around the inclusion if the body is subjected to a uniform applied stress [Goo33]. The magnitude of stress concentration will depend on the elastic properties of the matrix and inclusion. In reality, for matrix-inclusion systems or composites with property mismatch of thermal expansion coefficients and elastic constants, the initiation of fracture resulting from the inclusion will be governed by the complex state of stress resulting from both the residual stress and the stress concentration effects.

Another important effect of these impurities is that the impurities may react with major components to produce undesirable glassy grain boundary or interface phases, as discussed in section 2.1.2 and 2.1.3. Becher and Tiegs [Bec88] improved the mechanical property (fracture strength)

of composites by washing whiskers in deionized water, which may remove a minimum amount of impurities from whisker surface.

2.1.4.2 Whisker clusters and associated large pores. Another common defect associated with whisker reinforced composites are clusters of whiskers, which cause serious reliability problems (strength degradation, fracture toughness inhomogeneity) [Becher84, Wei85]. In order to break up nests of whiskers and to promote homogeneous mixing among the components, ball milling, ultrasonication or mechanical homogenization have been used [Tie86, 87a, 87b; Bul87a; Sac88].

Shalek et al.[Sha86a] obtained ~480 MPa fracture strength for Si_3N_4 reinforced with 30 vol% SiC whiskers while Buljan et al. [Bul87a] achieved near 1 GPa. One very important processing step taken in the work by Buljan et al. [Bul87a] was fractionation of whiskers by gravity sedimentation in order to remove large whisker clusters, followed by sonication and homogenization of the mixture of Si_3N_4 powder, sintering additives (Al_2O_3, Y_2O_3), and SiC whiskers in a liquid medium (methanol). On the other hand, Shalek et al.[Sha86a] used a dry mixing technique. The analysis of the fracture surface revealed an inhomogenous distribution of sintering additives and whiskers, very large inclusions, large pores, and pore clusters related to whisker nests. The inhomogeneous microstructure caused very scattered values in strength values as well as fracture toughness.

Therefore, the difference in fracture strength is a direct reflection of the difference in powder preparation and subsequent mixing procedures.

For a given volume fraction of porosity, mechanical properties deteriorate to a greater extent when pores are present as few, inhomogeneously-distributed large pores, rather than when pores are distributed homogeneously with finer size. The failure-initiating pores typically range from 10 to 200 μm in size, depending on the materials. In general, the strength of these ceramics decreases with increasing pore size and volume. Typically, strength and porosity have been related by the following empirical equation [Duc53]:

$$\sigma_p = \sigma_o \exp(-BP) \tag{2.3}$$

where σ_p and σ_o are the strength of the specimen with and without porosity, B is a constant that depends on the morphology and distribution of pores, and P is the pore volume fraction. Vardar et al. [Var77] suggested that a porous brittle material fails due to randomly distributed flaws near the stress field of the pores. That is, the microcracks associated with pores may grow subcritically before they become critical flaws, and then the length of the critical crack finally controls the fracture stress.

2.1.4.3 Agglomerates. So far we discussed the processing defects related to SiC whiskers, but there are also defects related to the matrix powders, e.g., agglomerates. Agglomerates are groups of particles held together by forces

such as surface charges, hydrogen bonds, van der Waals bonds, and chemical bonds. Very often agglomerates are formed during preparation of ceramic powders and/or during formation of green bodies. These agglomerates have a significant effect on the densification and strength of the sintered material. As mentioned earlier in regard to the work by Buljan et al.[Bul87], wet blending of whisker/powder mixture may lead to homogeneous mixing in liquid medium. However, it is important to maintain this homogeneity through drying of mixed powder or preparation of green compacts. Wei and Becher [Wei85] used a freeze drying technique in combination with wet mixing in order to ensure the homogeneity of powder mixture. However, they found that after hot-pressing there were still some regions, associated with Al_2O_3 agglomerates, which were devoid of whiskers. This illustrates the importance of the sizing and harvesting processes for both starting powders and whiskers. When the samples are fabricated by pressureless sintering, the matrix powder agglomerates can produce more serious defects, as observed in both single phase and composite materials [Rev63, Dyn84, Ric73, Lan83a, Lan 83b, Lan 83c, Jan87].

Defects associated with the presence of agglomerates are often crack-like voids which act as critical flaws. It has been proposed that the formation of voids and cracks around the agglomerates is due to the density difference between the agglomerates and matrix. Thus, the difference in density between the agglomerates and the matrix in the green compact

will result in differential shrinkage of agglomerates and matrix, and may cause separation of the agglomerates from the matrix. The differential strain between the matrix and agglomerates resulting from the difference in shrinkage can be given by the following equation:

$$\varepsilon = \left(\frac{\rho_{om}}{\rho_m}\right)^{1/3} \left\{ \left(\frac{\rho_{oa}}{\rho_{om}}\right)^{1/3} \left(\frac{\rho_a}{\rho_m}\right)^{-1/3} - 1 \right\} \tag{2.4}$$

where ρ_{om} and ρ_{oa} are the green densities of the matrix and agglomerate, respectively, and ρ_m and ρ_a are the sintered densities of the matrix and agglomerates, respectively. Equation (2.4) indicates that the magnitude of the differential strain, $\Delta\varepsilon$, will depend on the density ratios of the agglomerate and matrix in the green and sintered states. There are two cases of importance in which the green density of agglomerates is lower and higher, respectively, than that of the matrix. In the first case, the agglomerates will densify faster than the matrix during sintering. The resulting differential strain will cause a uniform tensile stress in the agglomerates as well as a tensile radial stress and a compressive tangential stress in the matrix. Depending on the densification kinetics and material properties, the tensile radial stress in the matrix can be large and may result in circumferential cracks. On the other hand, if the agglomerates have higher density than the matrix, the matrix will densify faster than the agglomerates. The resulting differential strain will put the agglomerates in compression

and the matrix will be subjected to a tensile tangential stress and a compressive radial stress. If the tensile tangential stress is large, it will cause radial cracks in the matrix as observed in Al_2O_3/ZrO_2 composites. These voids and cracks generally have adverse effects on the mechanical properties of the material and should be eliminated by minimizing the agglomerate size by appropriate fabrication routes.

2.2. Theoretical Background

2.2.1 Toughening Mechanism by Whisker Reinforcement

Some aspects of whisker toughening will be reviewed in this section. The incorporation of whiskers into a brittle matrix can be envisioned to enhance the toughness in accordance with several mechanisms: crack deflection [Fab83], microcracking [Evan84], and crack bridging [Evans86, Bec88a] and whisker pull-out [Beche86, Dav87]. Each of these mechanisms has very different microstructural requirements. Therefore, the basic toughening mechanisms for ceramic composites are discussed and basic requirements and the status of their verification and modeling are reviewed.

2.2.1.1 Crack deflection. The predominant toughening mechanism that has so far been exploited in composite development for applications in severe environments has been crack deflection by crack interaction with the dispersoid,

i.e., hard refractory particulates or whiskers. This mechanism originates in the presence of a stress field surrounding the dispersoid along the dispersoid/matrix interface, which is caused by thermal expansion or elastic modulus mismatch. Deflection toughening arises whenever interaction between the crack front and the second phase produces a non-planar crack, subject to a stress intensity lower than that experienced by corresponding planar crack. The non-planar crack arises either from residual strains present in the material or from the existence of weak interfaces (compared to fracture strength of dispersoid). The former derives from elastic modulus and/or thermal expansion mismatch between the matrix and the second phase. The sign of residual strain determines the direction of deflection. Specifically, as shown in Figure 2.4, a dispersoid with a greater thermal expansion coefficient or elastic modulus than the matrix produces a tangential compressive strain near the dispersoid particle/matrix interface and diverts the crack around the particle (Figure 2.4(A)). Alternatively, a second phase with a lower thermal expansion coefficient than the matrix induces tangential tensile strains, causing the crack to deflect toward the particle (Figure 2.4(B)). However, toughness measurements suggest that the sign and the magnitude of the residual strain have no significant influence on the magnitude of crack interaction toughening. For example, Si_3N_4 ceramics have relatively low thermal expansion coefficients

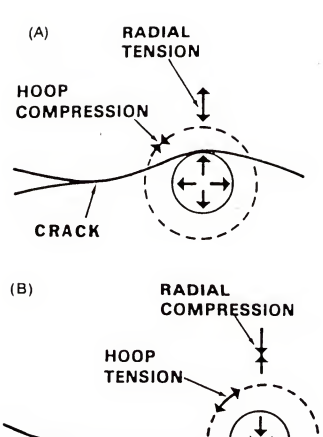

Figure 2.4 Crack-dispersoid interactions. (A) Schematic of interaction of crack with dispersoid in hydrostatic tension (e.g. due to $\alpha_d > \alpha_m$); (B) with dispersoid in hydrostatic compression (e.g. due to $\alpha_d < \alpha_m$) [Ric 81].

compared to most dispersoids, so that the residual strain state in the Si_3N_4 matrix surrounding such dispersoids is radial tension and tangential (hoop) compression [Sel61, Dav68]. This strain state tends to divert an advancing crack around the dispersoid as shown in Figure 2.4(A) [Esh57]. On the other hand, Al_2O_3 reinforced with SiC whiskers has the opposite signs of the residual stresses after densification (i.e., $\alpha_m > \alpha_d$) so the crack front will be attracted to the interface between matrix/dispersoid. In this case, the interfacial strength is estimated to be ~800 MPa compared to whisker tensile strength of ~8 GPa so that the crack will propagate along the interface [Bech88]. Subsequently, interface debonding, crack bridging, and whisker pull-out will be operative with more ease.

Toughening by crack deflection has been postulated to be independent of dispersoid size but dependent on dispersoid volume, irrespective of the sign of thermal expansion/elastic modulus mismatch stresses.

Numerical analysis by Faber and Evans [Fab83] demonstrated that crack deflection, which produces tilting and twisting of the advancing crack front, is an effective toughening mechanism and that the degree of toughening is dependent upon dispersoid shape. On a theoretical basis [Fab 83], rod-shaped particles are predicted to be more effective toughening agents than disc-shaped particles, which are more effective than spheres. Figure 2.5 shows the relative toughness as a function of whisker volume fraction for the

various aspect ratio. Although the toughness increased with increasing whisker content and aspect ratio, the toughness was essentially leveled off at whisker volume fraction higher than 0.2.

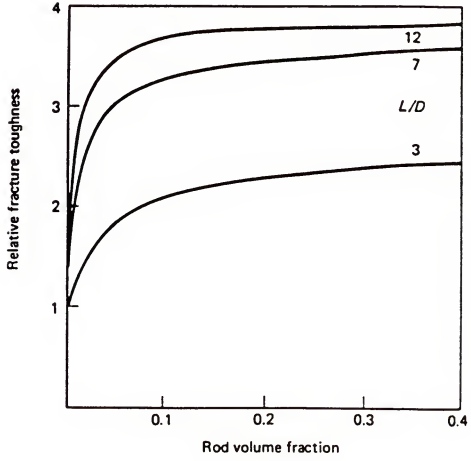

Figure 2.5 Theoretical predictions of composite toughening by dispersoids of various shapes [Fab83].

However, this has been clearly demonstrated only in glass-matrix systems [Fab83, Kri81], but not with

polycrystalline matrices. Recently, Buljan et al. [Bul87b] suggested that the matrix microstructure should be considered in evaluating the crack deflection mechanism in materials in which the matrix has grain boundary and/or interface boundaries (e.g., in polycrystalline matrix composites). The presence of intergranular fracture requires that grain size should be considered. In a material with typical intergranular fracture, the energy expended to propagate a crack is directly proportional to the amplitude and frequency of crack deflection of the grains. Based on geometrical considerations, Buljan et al. [Bul87b] approximated the expected fracture toughness change due to grain size by

$$\Delta K_{Ic} = cK_{Ic}^{\circ}\left(\frac{D}{D^{\circ}} - 1\right) \tag{2.5}$$

where c is proportionality factor and K_{Ic}° term represents the measured fracture toughness of the material with an average grain size D°. In the absence of other toughening effects and changes in fracture mode, the change of grain size from D° to D can produce an increase/decrease of fracture toughness directly proportional to D/D°. Based on these assumption, the fracture toughness of composite can be estimated using appropriate fractional contributions of matrix and dispersoid grain size. According to this analysis, the interaction of the advancing crack front with finer dispersoids (i.e., smaller than the matrix grains) should result in a reduction

of the composite fracture toughness due to the diminished amplitude of crack deflection [Bul87b].

2.2.1.2 Whisker Bridging. A recently proposed mechanism of toughening in polycrystalline ceramics is based in part on the observations of Swanson et al. [Swa87]. As shown schematically in Fig. 2.6, the intact whiskers that bridge the crack just behind crack tip exert crack-shielding traction forces. The bridging whiskers resist crack opening

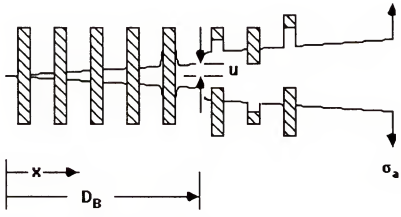

Figure 2.6 The presence of a whisker bridging zone behind the crack tip modifies the crack opening displacement. In the presence of bridging whiskers, closure forces and stresses are imposed on the crack surfaces.

by frictional sliding which occurs as one end pulls out of the matrix. The traction force acts to shield the crack tip from the applied stress, so that the K_I at the crack tip is less than the applied K_I by an amount proportional to the magnitude of the traction force. This mechanism seems to be prevalent in SiC whisker-reinforced Al_2O_3 composites

[Ang 86; Bec 88; Eva 86]. The toughening contribution resulting from bridging whiskers behind the crack tip (in bridging zone) is given below for the case where whisker bridging imposes a uniform closure stress in the debonding (or bridging) zone [Bech88]:

$$dK^w = \sigma^w \left\{ \left(\frac{V_f r}{6(1-\nu^2)} \right) \left(\frac{E_c}{E_w} \right) \left(\frac{G_m}{G_i} \right) \right\}^{1/2} \qquad (2.6)$$

where σ^w is the fracture strength of whiskers, ν is Poisson's ratio, V_f is volume fraction of whiskers, r is the radius of whisker, E is elastic modulus where subscript c and w represent composite and whisker, respectively, and G is strain energy release rate where m and i refer respectively to the matrix and interface. Therefore, the fracture toughness increases with increasing σ^w, V_f, and r and decreasing G_i.

Figure 2.7 shows plots of fracture toughness increment vs. SiC whisker content for various matrices. The toughening contribution due to SiC whisker reinforcement in various matrices increases with increasing whisker content. The extent of toughening is dependent on the matrix materials.

The difference in the extent of toughening can be explained by the other factors such as E_m, G_m/G_i. The magnitude of dK(w) increases with increasing Young's moduli of the matrix, i.e., increasing E_c/E_w. The elastic properties generally obey the rule of mixtures quite well so that $E_c = (1-V_f)E_m + V_f E_w$. Therefore, the toughening contribution from

whisker bridging increases as the elastic modulus of the matrix increases.

However, Si_3N_4 show significant deviation from the prediction (eq(2.6)) considering its high elastic modulus (higher than mullite). This behavior appears to be related to interface properties. As Becher and coworkers [Bech88] pointed out, the interface properties are significantly affected by the nature of the chemical bond of the whisker-matrix interface as well as mechanical constraints imposed on the whiskers by the matrix (e.g., stresses due to thermal mismatch). Using the solution for debonding where the main crack is normal to the interface, the ratio of the fracture energy of the matrix to that of the interface can be estimated by [Ken86]

$$\frac{G_m}{6G_i} = \frac{l_{DB}}{r} \tag{2.7}$$

where l_{DB} is the length of the interface debonding over which the displacement of whisker occurs due to the stress transfer from matrix to whisker. Generally, interface cracks (debonding) are observed immediately behind the crack tip which altered the propagation of the main crack in the matrix. Further behind the crack tip, whisker pull-out occurs as a result of interface debonding or whisker fracture in the debonding zone [Bech88, Evans86].

In general, whisker fracture in the debonding zone occurs at the end of the debonding so that the debonding

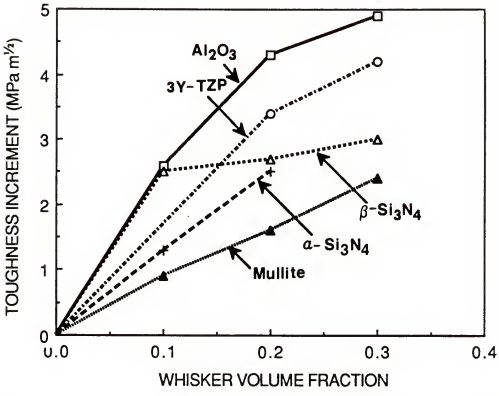

Figure 2.7 Plots of fracture toughness increment vs. SiC whisker volume fraction for various matrix materials.

length approximately equals the pull-out length of the whisker ($l_{DB} \sim l_{po}$) [Bech88, Evans86]. Thus, even though direct measurement of G_m/G_i is not possible at the moment, one can estimate this value by combining the experimental results and the analytical description. Becher and Tiegs [Bech88] expected that in order to achieve substantial increase in toughness (dK~20 MPa$\cdot$m$^{1/2}$), one must control debonding (i.e., interface), increase G_m/G_i, and/or develop whiskers with higher fracture strengths (~20 GPa).

2.2.1.3 Whisker Pull-Out. Whisker pull-out can occur when the stress transferred to the whisker during fracture of the

matrix is less than the fracture strength of whisker ($\sigma_f(w)$) but generates a shear stress that is greater than the interfacial shear strength of the whisker-matrix interface (τ_i). For a given whisker radius (r), the axial tensile stress generated in the whisker during pull out will be

$$\sigma_t = 2\tau_i\left(\frac{l_c}{r}\right) \tag{2.8}$$

where l_c is the critical length of the whisker where σ_t is equal to $\sigma_f(w)$, fracture strength of whisker. The tensile stress increases from a minimum at the end of the whisker to a maximum along the central portion of its length. For those whiskers bridging the fracture plane and whose ends terminate within $l_c/2$ from this fracture plane, pull-out will occur, while those with ends further away will fracture when $\sigma_t > \sigma_f(w)$. For uniaxially aligned whiskers with a mean length , l^* , the total work required to pull out whiskers will be

$$W_{po} = \left(\frac{l_c}{l^*}\right) \pi r \left(\frac{\tau_i}{12}\right) (l_c)^2 V_w \tag{2.9}$$

where V_w is the volume fraction of whiskers.[Beche86, Kel73] Note that to avoid premature fracture of the whiskers, both τ_i and thus σ_t should be minimized while τ_i needs to be positive in order to achieve a high work of pull-out. This can be achieved with whiskers with very high tensile strength and where the length of the whiskers, l, is $<l_c$:

$$l < l_c = \sigma_f(w)\ \tau_i\ (r/2) \tag{2.10}$$

where we assume that only a mechanical bond exists between the whisker and the matrix. For the mechanical bond case, the interfacial shear strength for a rod-like whisker will depend upon the coefficient of sliding friction between whisker and matrix (μ)

$$\tau_i = \mu \sigma_n \tag{2.11}$$

where σ_n is the stress acting normal to the interface parallel to the longitudinal axis of the whisker. When the matrix and whisker have property mismatch (i.e., Young's moduli, thermal expansion coefficient), σ_n is imposed by the radial matrix stress, σ_r (equation 2.2). When σ_r is compressive (<0) τ_i will be positive; while τ_i will be zero when σ_r is tensile (>0). Considering only this clamping force (assuming μ=0.5), the estimated τ_i values for Al_2O_3/SiC whisker and mullite/SiC whisker were ~800 and 135 MPa, respectively. These τ_i values are considerably larger than those measured for the SiC fiber-LAS glass-ceramic matrix system (τ_i < 5 MPa) where α_m < α_w so that σ_n is a tensile stress [Mar84]. For most of whisker composites, the lengths of whisker pull-out are very short so that toughening effect due to pull-out appears to be very limited [Tie86, Bul87a, Cla86, Bech88].

2.2.1.4 Multiple Toughening Mechanism. As mentioned earlier, mullite/ZrO_2/SiC whisker composite can increase fracture toughness higher than 10 MPa·$m^{1/2}$. This is achieved by two different toughening mechanisms [Cla86, Tie86, Bech87]. Dispersed ZrO_2 particles in ceramics are used to

increase toughness either by stress induced transformation of tetragonal ZrO_2 or by stress induced microcracking associated with monoclinic ZrO_2 in a zone surrounding the crack. These ZrO_2 toughening mechanisms are sensitive to the toughness of matrix and their contribution can be enhanced by increasing the matrix toughness. If the matrix toughness increases, then the crack tip stress must be increased for the crack to propagate and, as a result, the process zone size ($2r^T$) should increase. In the case of transformation toughening, the transformation toughening contribution, dK_{Ic}^T, is

$$dK_{Ic}^T = A\ V\ E_c\ e^T\ (r^T)^{1/2} \qquad (2.12)$$

where A is a constant dependent upon stress state, V is the volume fraction of transformable tetragonal ZrO_2, E_c is the Young's modulus of the composite, and e^T is the transformation strain [Mar83]. The zone size is dependent on the matrix toughness, K_{Ic}^M

$$r^T = B\ (K_{Ic}^M/\sigma_c^T)^2 \qquad (2.13)$$

where σ_c^T is the stress required to initiate the transformation and B is a function of crack tip stress state [Evans82]. Similar dependence are expected for stress induced microcracking. Thus if one considers that the whiskers increase the effective matrix toughness, the presence of dispersed ZrO_2 particles should result in additional toughening.

2.2.2. Thermochemical Stability

In composites containing dissimilar materials, chemical interactions between the various constituents would be limiting factors in fabrication processes. Therefore, it is important to control the fabrication atmosphere in order to produce composites that retain the original chemical and physical properties of the constituents.

Commonly, the chemical compatibility have been predicted based on the thermodynamic calculations among the constituents in the ideal atmospheric conditions [Lut88; Nic88]. However, the atmosphere is likely to be dependent on the furnace construction and heating elements. The furnace used in this study was a induction furnace using graphite susceptor. The atmosphere associated with heat treatment in this furnace is likely to be quite different from a furnace with tungsten heating elements, for example.

Tiegs and Becher [Tie86] have observed a wide range of weight loss in the Al_2O_3-20 vol% SiC whisker composites during densification under hot-pressing, i.e., 0.8 % to 5.17 % depending on the source of SiC whiskers. They attributed these weight losses to the reaction between Al_2O_3 and SiC whiskers.

Marra and Bray [Mar86] analyzed reaction products of Al_2O_3/SiC(w) powder mixture (1:1 weight ratio) during heat treatment in different atmospheres (dry air, vacuum, argon) using mass spectroscopy (MS) for reaction product gas analysis, and differential thermal analysis(DTA), X-ray

photon spectroscopy(XPS), X-ray diffraction(XRD), and scanning electron microscopy(SEM) for solid or liquid reaction products. At temperatures up to 1200oC (in a dry air atmosphere), the reaction products consisted mainly of cristobalite, Al_2O_3, and SiC, along with evolving CO_2 gas. At higher temperature (>1550°C), the product phases were primarily mullite and cristobalite. In vacuum, the mixture decomposes at a faster rate to give a gaseous products consisting of Al(g), Al_2O(g), CO(g), and SiO(g). The bulk materials were essentially Al_2O_3 and SiC while materials on the surface were made up of Al_2O_3, SiC, and Al_4O_4C. Finally, in argon which is of particular interest in this study, there was only ~2 % weight loss. (In vacuum, the weight loss was more than 20 %.) In argon, solid phases were mainly Al_2O_3 and SiC whereas the gaseous products were CO(g) and SiO(g).

According to the results obtained by Marra and Bray[Mar86], the possible reactions in the present study are

$$SiO_2(s) + SiC(s) = 2SiO(g) + C(s) \quad (2.14a)$$

$$2SiO_2(s) + SiC(s) = 3SiO(g) + CO(g) \quad (2.14b)$$

$$3Al_2O_3(s) + 2SiO_2(s) = 3Al_2O_3 \cdot 2SiO_2(s) \quad (2.14c)$$

$$Al_2O_3(s) + CO(g) = Al_2O(g) + CO_2(g) \quad (2.14d)$$

$$SiO_2(s) + CO(g) = SiO(g) + CO_2(g) \quad (2.14e)$$

Since silicon-based materials, such as SiC, Si_3N_4, and Si, readily form protective surface SiO_2 layer, silica is available to react either with Al_2O_3 or SiC. In order to identify pertinent reactions, it is necessary to find out the Gibbs free energy change, ΔG. If the standard free energy

change of the reaction is negative, then the reaction is favorable. However, although the reaction (2.14c) has a negative ΔG over all entire temperature range considered here, Marra and Bray [Mar86] could not detect mullite except in air at relatively high temperatures. This indicates that the surface silica has been consumed in different reactions. It is thus informative to calculate the equilibrium partial pressure of the gaseous products and the equilibrium activities of the solid reaction products, since the reaction can occur even if the standard free energy change is positive. As for reactions 2.14a and 2.14b, under the conditions that the activities of solids are 1, the directions of reactions are dependent on the CO partial pressure, P_{CO}. By calculating equilibrium partial pressure of CO, the P_{CO}-temperature diagram is constructed based on JANAF tables [Stu71] in the temperature range 1500-2500K as shown in Figure 2.9. Over the entire temperature range, the equilibrium partial pressure of CO is quite high so that reactions (2.14a) and (2.14b) will proceed to the right side until they reach the equilibrium CO partial pressures. Therefore, SiC whiskers will decompose to give SiO(g) and CO(g) at very low partial pressure of CO gas which is commonly confronted during processing. (Sintering is often carried out in graphite resistance furnace and hot pressing is often carried out in graphite die under flowing inert gas atmosphere.)

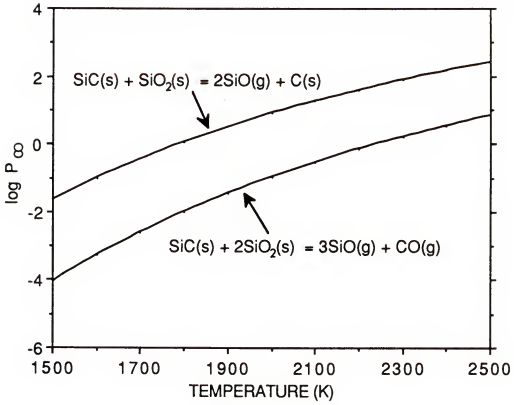

Figure 2.8 Plots of equilibrium P_{CO} vs.temperature for the reaction between SiC and surface SiO_2.

If the partial pressure of CO is high enough to reverse the reactions (2.14a and 2.14b), the matrix, Al_2O_3, is likely to decompose to give Al_2O_3 and CO_2 at high temperatures(reaction 2.14d). A similar reaction can occur with SiO_2 (reaction 2.14e). The effect of CO partial pressure on the decomposition reactions of Al_2O_3 and SiO_2 is shown in Figure 2.9. The thermodynamic calculations (Figures 2.8 and 2.9) indicates that the reaction between SiC whisker and surface SiO_2 may accompany the decomposition of Al_2O_3. Based on the observation by Marra and Bray using mass spectroscopy

[Mar86], it is believed that the pertinent reactions are reactions (2.14b,d,and e).

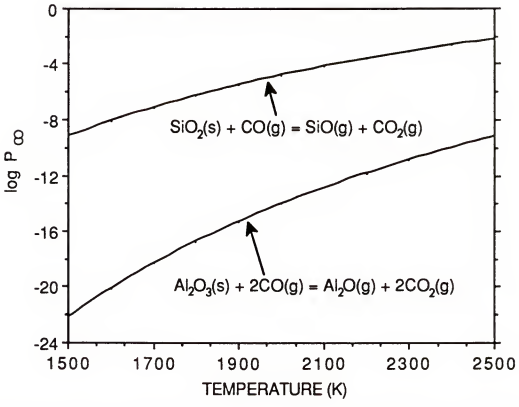

Figure 2.9 Plots of equilibrium partial pressure of CO gas vs. temperature for the decomposition reaction of Al_2O_3 and SiO_2.

When gas phases evolve during a high temperature process, the evaporation rate is dependent on the surface area and the gas partial pressures. Under vacuum, the volatilization rate would be maximum and can be given by the Hertz-Langmuir equation [Sea70]:

$$J = \frac{p}{(2\pi MRT)^{1/2}} \qquad (2.15)$$

where J is the volatilization rate per unit area, p is the partial pressure of the volatile species, T is the

temperature, and M is the molecular weight of the volatile species. Under flowing gas conditions, the volatilization rate can be calculated from the following equation [Lut88]:

$$J = \frac{DCp}{\delta P} = \frac{kCp}{P} \qquad (2.16)$$

where D is the diffusion coefficient of the volatile species, p is its partial pressure, C is the gas density, P is the total gas pressure, δ is the boundary layer thickness, and k is the mass-transfer coefficient. This equation indicates that gas evolution rate increases as partial pressure of the gas is higher, total gas pressure is lower, and diffusion rate of gas is higher. That is, the equilibrium state can be destroyed by removing the evolving gases so that the reaction can proceed. Therefore, although it is necessary to examine thermodynamic equilibrium conditions, kinetic factors must also be considered when trying to minimize considerable reactions. In our system, it is obvious that we need to control the partial pressure of CO and SiO gases. There are two strategies of controlling atmosphere: (1) use an inert atmosphere which may minimize undesirable environmental attack from the surrounding atmosphere (passive protection) (2) use an atmosphere which can attack the impurities (e.g. H_2 in metal sintering) or (3) maximize the partial pressure of reaction product gases in order to reverse reactions (active protection). The latter strategy (active protection) is commonly exercised by using packing powder with the same composition as the samples being sintered.

2.2.3 Constrained Sintering

Ceramic composites are generally produced by hot pressing in order to achieve high density and good mechanical properties. Difficulties in the sintering of composites in the absence of external pressure originate from the presence of dense inert inclusions in a porous matrix. There is no successful general theory available for explaining this phenomena. However, there have been two approaches: (1) viscoelastic model in which the presence of the inert inclusions generates differential sintering rates between inclusion and matrix which in turn induce tensile stresses within the matrix [Raj84; Bor 86; Rah87, 88; DeJ88; Hsu86; Sch87], and (2) network model in which inclusion particles form network structures (clusters) resisting the deformation caused by sintering stress [Lan87]. Both of the models are far from satisfactory, but they show the critical parameters which retard densification in composites sintering. Thus, some of key elements of the above models are reviewed and criticized in this section.

2.2.3.1 Viscoelastic model. Transient stresses are developed during sintering when one region of the powder compact shrinks differently from its surroundings. Deviatoric creep will always tend to relieve the stresses. The calculation of the stresses therefore requires a viscoelastic solution to the problem where differential shrinkage generates internal stresses in the body and the internal

stresses are relaxed by creep. The stresses oppose the sintering driving force, and the densification rate of the matrix is accordingly reduced. Several attempts have been made to evaluate the evolution of such stresses both theoretically and experimentally. Figure 2.11 shows the geometry of a non-densifying inclusion in a sintering matrix. In this case, a compressive radial stress, σ_r and tensile hoop stresses, σ_θ ($=\sigma_\phi$) are generated in the matrix. The stresses have their maximum values at the matrix-inclusion interface (r=a) and decrease as $1/r^3$ into the matrix.

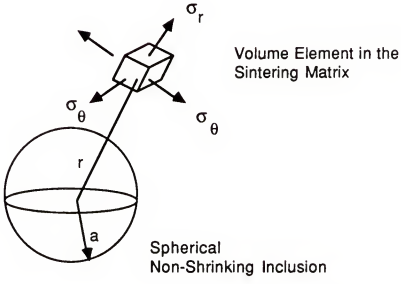

Figure 2.10 A rigid inclusion in a sintering matrix. Compressive radial stress (σ_r) and tensile circumferential stresses ($\sigma_\theta=\sigma_\phi$) are generated in the matrix.

Let $\sigma_r(a)$ be the radial stress at the interface and $\sigma_\theta(a)$ be the hoop stress in the matrix at the interface. The two are related by

$$\sigma_\theta(a) = -\sigma_r(a)\left(\frac{(1+2v_i)}{2(1-v_i)}\right) \qquad (2.17)$$

where v_i is the volume fraction of inclusions. The mean (hydrostatic) stress in the matrix is given by

$$\sigma = \frac{[\sigma_r(r) + 2\sigma_\theta(r)]}{3} = -\sigma_r(a)\left(\frac{v_i}{1-v_i}\right) \qquad (2.18)$$

In the inclusion, all three stress components are equal to $\sigma_r(a)$. Therefore, the inclusion is under purely hydrostatic stresses whereas in the matrix both hydrostatic and deviatoric stresses are present. The tensile stress, $\sigma_\theta(a)$, has been postulated to be responsible for radial cracks observed around heterogeneities. In addition, the uniform tensile hydrostatic stress σ has been used to explain the significant retardation of the densification of the matrix observed experimentally. For a sintering material, the free strain rate ($\dot{\varepsilon}_f$) is the linear contraction rate of an unconstrained body, which is the quantity typically calculated in theories of sintering. Densification is generally attributed to a hydrostatic compressive stress, Σ, called the sintering stress or sintering potential, which arises from the solid-vapor and solid-solid (grain boundary) interfacial energies.

The sintering potential is related to the volume strain rate through the bulk viscosity of the porous body as follows [Bor88a]:

$$\dot{\varepsilon} = (\Sigma+\sigma)/K_p \qquad (2.19)$$

For a glass, we expect $K_p \propto \eta$ and $\dot{\varepsilon}_f \propto 1/\eta$, so Σ is independent of the viscosity, and hence of temperature. Indeed, if Σ is physically meaningful, it is expected to depend only on geometrical factors and interfacial energies. For a polycrystalline material, the sintering mechanism may be different from the mechanism governing deformation under the stresses developed in the presence of inclusions. For example, $\dot{\varepsilon}_f$ may be related to the volume diffusion coefficient and K_p may depend on grain boundary sliding. In such cases, Σ involves the ratio of different diffusion coefficients; if the latter have different activation energies, then S could be strongly temperature-dependent.

For a uniform matrix (no heterogeneity), there is no stress so:

$$\dot{\varepsilon} = \Sigma/K_P \tag{2.19}$$

Since $\dot{\varepsilon}$ represents contraction rate and Σ is compressive, both are negative quantities. For a composite in which the heterogeneity sinters more slowly than the matrix, the volumetric strain rate in the matrix is expressed by the following equation [Bor88b]:

$$\dot{\varepsilon} = \frac{1}{K_P}\left(\Sigma - \left(\frac{v_i}{1-v_i}\right)\sigma_r(a)\right) \tag{2.20}$$

Since $\sigma_r(a)$ is compressive (negative), the effect of the heterogeneity is to reduce the shrinkage rate of matrix ($\sigma_r(a)$ is compressive).

Finally, the stresses developed due to a non-sintering inclusion were expressed in terms of volume fraction of inclusions and Poisson's ratio:

$$\sigma_\theta(a) = -\frac{\Sigma(1-2\nu_p)}{1+\nu_p(1-4\nu_i)/(1+2\nu_i)} \qquad (2.21)$$

and

$$\sigma_r(a) = \frac{2\Sigma(1-2\nu_p)(1-\nu_i)}{(1+\nu_p)+2\nu_i(1-2\nu_p)} \qquad (2.22)$$

As shown in the equation (2.21) and (2.22), the stresses are the function of sintering stress(Σ), Poisson's ratio of the body being sintered (ν_p), and the volume fraction of inclusions (ν_i). An extremely broad range of values have been calculated by various authors for the back stress against sintering stress. For example, Raj and Bordia[Raj 84], Hseueh [Hsu86], and Scherer [Sch87] estimated the stresses as ~45, ~250, and ~2 $\sigma_r(a)/\Sigma$, respectively. Such a discrepancy arises from the difference in Poisson's ratio in the porous body (-1.0 to 0.5). As a result, most models, which are empirical or semi-empirical, employ adjustable parameters. Therefore, there is a need for more careful analysis and more experimental results for the viscoelastic response of porous body against stresses.

Nonetheless, as pointed out in equation (2.20), the densification rate of composite is controlled by the volume fraction of inclusions, Poisson's ratio, bulk viscosity, and sintering stress. That is, the densification rate can be enhanced by reducing the volume fraction of inclusions, which

may minimize the contribution of the radial compressive stress, ultimately reducing the tensile hydrostatic pressure. Secondly, increasing sintering stress will enhance densification. Increased sintering stress can be readily achieved by applying external pressure (i.e., hot pressing or hot isostatic pressing) to counteract the compressive radial stresses from inclusions. Thirdly, decreasing bulk viscosity will relax the radial compressive stresses caused by non-sintering inclusions. Similar conclusions were drawn theoretically and experimentally by several other authors [Hsu86; Raj84; DeJ88; Bro88a; Bro88b]

The analysis of Hsueh et al.[Hsu86] suggests that the matrix stress will fall with rising temperature, provided that the activation energy of the densification process, which generates the stress against sintering, is lower than that of the creep process, which relaxes the stress. In separate studies, Raj and Bordia [Raj 84], and De Jonghe and Rahaman [DeJ88] similarly emphasized the ratio of densification rate to creep rate, the analyses of which show that the matrix stress is increased with increase in the ratio.

There is a very limited number of experimental studies to prove the effect of the back stresses caused by non-sintering inclusions. Brook and his co-workers [Bro88a; Bro88b] studied the influence of volume fraction of inclusions, matrix particle size, and matrix viscosity on the densification behavior of composites using 200 μm fused

alumina inclusion. They also estimated the creep strains by measuring the dimension change of the intentionally introduced large pores (~140 μm) in Al_2O_3, ZrO_2, and glass matrices [Bro88b]. Their results show, however, that while the addition of dense inclusions severely retards the densification rate, the extent of the retardation is decreased with increasing sintering temperature [Bro88b]. This behavior was attributed to the increased creep strain, i.e., decrease in viscosity, with increasing temperature. The data suggest that the matrix stress can be decreased by lowering the matrix viscosity with decreased matrix particle size. Further decrease in viscosity could be achieved by using a glass matrix. In the studies by Brook et al., creep strain values were 1.53% for alumina (density ~83), 2.04% for zirconia (density ~84%), and 7.73% for glass (density ~79%).

Rahaman and De Jonghe [Rah88] showed that glass matrix composites may be sintered even with 30 volume percent of inert SiC inclusions, despite a significant deviation from theoretical prediction. Polycrystalline matrix (ZnO) composites were severely inhibited by the presence of the SiC inclusions. For example, the ZnO matrix composites with >20 vol% SiC inclusions did not show any densification at all. Regardless of the matrix phase, most experimental results show significant deviations from theoretical predictions above matrix density of ~70% with the inclusion volume fraction of >0.15. They attributed this deviation to interactions between the inclusion particles. Thus, it was

postulated that the inclusions will initially interfere, and later will come into contact, eventually leading to a hard skeleton structure that densifies with much more difficulty. Therefore, the densification behavior of composites with relatively high content of inclusions will be dominated by impingement effects rather than the viscoelastic backstresses. Most viscoelastic models are based on the assumptions that the inclusion is much larger than matrix particle, and that the inclusions do not touch each other. This is the main reason for a large discrepancy between viscoelastic model and experimental result at relatively high inclusion concentrations. In analogy to a viscoelastic model, Dynys and Halloran [Dyn84] postulated that the retarded densification of alumina compacts with a high content of aggregates is a reflection of the decreased driving force due to the tensile stresses developed in the matrix. They evaluated the tensile stresses developed in the matrix by simply applying Coble's hot-pressing model [Cob70]. That is, the shrinkage rate depends on the surface tension, γ, and the applied stress, P_{eff}, according to

$$\left(\frac{\Delta L}{L_o}\right)_c^2 = \left(1 \pm B \frac{P_{eff}}{\gamma}\right)\left(\frac{\Delta L}{L_o}\right)_o^2 \qquad (2.23)$$

where $(\Delta L/L_o)$ is shrinkage, B is geometric constant depending on coordination number, γ is surface tension, P_{eff} is effective applied stress [Cob70]. The subscript c and o outside parentheses refer to composite and matrix,

respectively. Dynys and Halloran [Dyn84] suggested that the stress developed during differential sintering reduced the net driving force by about 30% as the amount of aggregate increased from 6% to 20%.

2.2.3.2 Network (percolation) model. Recent development of percolation theory predicts that small fractions of inclusions may form finite size of cluster (impingement between inclusions), ultimately causing a significant retardation in densification of composites [Zal83]. In the following, percolation theory is introduced to predict critical whisker volume fraction in the composite for full densification under pressureless sintering condition.

Percolation theory deals with the effects of varying, in a random and very large system, the degree of interconnections present. The single most important aspect of the percolation model is the presence of a sharp transition at which long-range connectivity suddenly appears. It is this percolation transition, which occurs with increasing connectedness or density or occupation or concentration, that makes percolation a natural model for a diversity of phenomena.

There are two basic types of percolation process: bond percolation and site percolation. A lattice is composed of sites (vertices, intersections between bonds) and bonds (edges, links, pairwise connections between sites). In both cases, the space to fill starts with a regular geometric object, a periodic lattice. In bond percolation, each bond is

either connected (which occurs with probability p) or disconnected (which occurs with probability 1-p). The assumption of completely random system means that the probability p, for every bond, is independent of the state of the neighboring bonds. In site percolation, each bond is considered to be connected, and it is now the sites which carry the random connectivity character of the structure. Each site is either connected (unblocked) or disconnected (blocked), with probability p and 1-p, respectively. Again, p is the same for each site, and is not influenced by the state of the neighboring sites. At low concentration regime (i.e. $p \ll 1$), nearly all of the occupied sites or bonds will occur as isolated singlets or clusters of size one. The probability of encountering a cluster of size s is of the order of p^s. Thus the cluster-size distribution, in the $p \rightarrow 0$ low density limit, is sharply peaked at s=1 and falls off exponentially with increasing s. s is used to denote cluster size. The cluster-size distribution is typically expressed as a discrete function n(s), defined at s = 1, 2, 3, 4, ..., where n(s) is normalized per site, that is, n(s) is the number of clusters of size s divided by the total number of sites in the system (for a large system). As p increases, probability of continuing a cluster becomes larger. The mean cluster size (s_{av}) grows. Since the number of sites occuring in clusters of size s is proportional to sn(s), then the site-weighted average cluster size is given by

$$s_{av} = \frac{\sum_s s^2\, n(s)}{\sum_s s\, n(s)} \qquad (2.24)$$

The sum in the denominator of this expression is proportional to the total number of filled sites. The numerator is a corresponding sum in which each filled site is weighted by the size of the cluster to which it belongs.

When we increase p, there will be a point where the percolation path would first be observed. This critical concentration p_c is called percolation threshold at which the system of interconnections has grown sufficiently for a connected network to propagate indefinitely (appearance of lattice-spanning percolation cluster). When it first appears, the percolation path is very tortuous. The tenuous nature of the infinite cluster, when it appears, can be characterized by a fractal dimensionality which is somewhat smaller than the space dimensionality of the percolation process being considered.

This fractal dimensionality is related to the critical exponents controlling the properties of a percolating system near its critical point. Another quantities to be defined are mean cluster size $s_{av}(p)$ and mean spanning length $l_{av}(p)$ (in fact, $s_{av}(p)$ was already defined). s grows as p increases, becomes large as $p \rightarrow p_c$ (very large cluster forms), and finally becomes infinite at $p = p_c$ with the emergence of the infinite cluster. Whereas s, the number of connected sites or bonds, provides the natural measure of the content or volume

or mass of a given cluster, l provides a measure of the cluster's characteristic linear dimension. The spanning length is defined as the maximum separation of two sites (or bonds) in the cluster:

$$l \equiv \max \{ | \mathbf{r}_i - \mathbf{r}_j | \}_{i,j \text{ in cluster}} \qquad (2.25)$$

We now focus on the region very close to the percolation threshold (p_c is approached from lower p).

$(p_c-p) \rightarrow 0$:

$$s_{av} \sim (p_c-p)^{-\gamma} \qquad (2.26)$$

$$l_{av} \sim (p_c-p)^{-\nu} \qquad (2.27)$$

$$n(s) \sim s^{-\tau} \qquad (2.28)$$

$$l(s) \sim s^{(1/f)} \qquad (2.29)$$

Finally, the percolation probability P(p) can be expressed by

$$P(p) \sim (p_c - p)^{\beta} \qquad (2.30)$$

In equations (2.26)-(2.30), the exponents γ, ν, τ, f, and β are found to be, for lattices in two and three dimensions, positive numbers that are not integers. The remarkable feature of the power-law dependences of equations (2.31)-(2.35) is that these exponents do not depend on the details of lattice geometry, they are the same for all lattices of the same dimensionality.

The experimentally observed exponents are presented in Table 2.2. This power-law holds only at ~p_c. Throughout the entire range below threshold, for each value of p, the fall-off in n(s) is much more rapid:

$$p < p_c, \; s \rightarrow \text{infinity}: \; n(s) \sim \exp[-\text{const.} \times s] \qquad (2.31)$$

This exponential decay of the frequency of occurrence as a function of cluster size is the asymtotic behavior appropriate to a regime in which localization (all clusters finite) applies. The constant is fixed for fixed p, but changes when p changes.

Table 2.2 Critical exponents controlling the near-threshold scaling behavior of key quantities in percolation [Zal83]

		Exponent in d dimension	
Functional form at $p \sim p_c$	Exponent	d=2	d=3
$P(p) \sim (p_c-p)^{\beta}$	β	0.14	o.4
$s_{av} \sim (p_c-p)^{-\gamma}$	γ	2.4	1.7
$l_{av} \sim (p_c-p)^{-\nu}$	ν	1.35	0.85
$n(s) \sim s^{-\tau}$	τ	2.06	2.2
$l(s) \sim s^{(1/f)}$	f	1.9	2.6

Now let us consider sintering of a composite containing inclusions. As p increases, all the scales (s_{av}, l_{av}, and l(s)) increase. Therefore, as densification proceeds, concentration of inclusions, p, initially below p_c, becomes large enough to develop inclusion-inclusion interactions (e.g., clusters) due to volume shrinkage. Particularly, when the distribution of inclusion particles is not homogeneous, frequency of clusters of a finite size will increase more rapidly. If the impingement effect is dominant in composite sintering, as postulated by Rahaman and De Jonghe [Rah 88], densification behavior of whisker-containing composites will

be more severely retarded because the excluded volume of the inclusion increases as its aspect ratio of increases. Percolation theory predicts the percolation threshold of rod type whiskers will be much lower than that of spheres [Boi83; Hol89]. According to Boissonade and coworkers [Boi83], the percolation threshold values of 0.3119, 0.1554, 0.0635 were obtained in the simple cubic lattice for aspect ratio of 1, 5, 15, respectively. This shows the dominant effect of aspect ratio on packing or densification behavior of composites containing whiskers.

Table 2.3 Critical concentration for bond and site percolation on a variety of lattices [Zal83].

Dimension d	Lattice or Structure	p_c^{bond}	p_c^{site}	Coordination, z	Filling Factor, v	$vp_c^{site} = f_c$
2	Triangular	0.347	0.500	6	0.907	0.45
3	fcc	0.119	0.198	12	0.741	0.147
3	bcc	0.179	0.245	8	0.680	0.167
3	sc	0.247	0.311	6	0.524	0.163
3	rcp		0.27		0.637	0.171

Weiser and De Jonghe [Wei88] observed that the densification of ZnO/SiC composites was more severely retarded with decreasing inclusion size. They attributed this phenomenon to the higher degree of clustering of the dispersed SiC inclusions. Similar effect of inclusion size was observed with alumina matrix with fused alumina

inclusions by Brook et al. [Bro88]. According to percolation theory, this may be related to the local clusters which formed during the preparation of powder mixture, forming, and sintering. It is likely, with finer inclusions, that the increased contact probability (due to the increased number of sites) may increase the number of local clusters. Consequently, the local clusters with open structures might increase the excluded volume of the inclusion particles, which increases the restraining force of inclusions against the intrinsic sintering force.

Holm and Cima [Hol89] calculated percolation threshold for two dimensional whisker percolation by computer simulation. They predicted that the percolation threshold (critical volume fraction in which whiskers interconnect each other) decreases as whisker aspect ratio increases. The percolation threshold value 23.75% was obtained for whisker aspect ratio of 10 while the threshold value decreased to 15.37% for aspect ratio of 20. As expected, the values are much higher compared to the values obtained in three-dimensional percolation in a simple cubic lattice [Boi83]. But percolation theory assumes that all the sites or bonds behave identically, which means that there is no inhomogeneities.

Table 2.3 shows the percolation threshold for the spheres in the various lattice structures. It is obvious that the percolation threshold is dependent on dimensionality, that is, p_c for 3-d is 0.311 compared to 0.5 in 2-d with the

same coordination number (Z=6). This is consistent with the results obtained for 2-dimensions by Holm and Cima [Hol89] and for 3-dimensions by Boissonade et al.[Boi83]. Another feature of percolation theory is that percolation threshold depends on the lattice geometry, but the critical volume f_c (that is, continuum percolation threshold) is almost the same regardless of lattice type.

Experimentally the critical volume for the formation of whisker skeleton structure can be estimated from the packing study of rod-type fibers. Using wooden rods and glass fibers, Milewski reported the packing density of fibers as a function of aspect ratio (length, L, to diameter, D, ratio) [Mil78; Mil86]. This purely mechanical packing study showed that the packing density of fibers has a strong dependence on the aspect ratio of fibers. For example, the packing density for fibers with an aspect ratio of 49 is only 10.3 % whereas the packing density with L/D = 15.5 is approximately 31 % [Mil86]. The results from percolation process and mechanical packing strongly illustrate that, at higher whisker content, whiskers readily form network structures. These network structures are expected to strongly resist deformation during densification. This effect will be intensified with poor spatial distribution of whiskers since poor mixing of whiskers and matrix will result in premature contacts of whiskers by shrinkage during densification.

According to Lange's network model [Lan87], composite density can be related to matrix shrinkage as following:

$$\rho_c = \rho_{oc} \{1 - \varepsilon_m[1 - (1/\alpha)(f/s)^{1/3}]\}^{-3} \qquad (2.32)$$

where ρ_c and ρ_{oc} are sintered and green densities, respectively, ε_m the matrix shrinkage, f volume fraction of inclusions, s the limiting volume fraction where the closest inclusions touch to form a continuous network, and α a numerical constant which defines the separation distance between inclusions. He was able to fit the densification data by De Jonghe et al. [DeJ86] to his model quite well by adjusting the numerical factor α. However, the limiting volume fraction used was assumed to be 0.277 based on experimental results obtained by De Jonghe et al. [DeJ86], but the limiting volume fraction may be varied by consolidation method. He used a different numerical constant, α, for different volume fraction of inclusions in order to adjust the separation distance between inclusion particles. This adjustment can change the the primitive lattice structure resulting in the variation of limiting volume fraction, s (i.e. percolation threshold). Another problem of this model is that the densification behavior of composites will be same for both polycrystalline and amorphous material, which is inconsistent with the experimental observation [Rah87; Rah88; Sch87] Therefore, it is hard to apply this model rigorously to predict the densification behavior of composites.

2.2.3.3 Contact probability argument. In multicomponent systems, the decrease in free surface energy (γ_A, γ_B) and in

interfacial energy (γ_{AB}) is a prerequisite for the commencement of sintering. According to Thummler and Thomma [Thum67], a condition for mixtures of phases, that neither react to form a compound nor interdiffuse to form solid solution, is

$$\gamma_{AB} < \gamma_A + \gamma_B \tag{2.33a}$$

With

$$\gamma_{AB} > \gamma_A + \gamma_B \tag{2.33b}$$

no sintering of the A-B contacts takes place, although the A-A and B-B contacts sinter together in every case. According to Goodison and White [Goo62], the sintering characteristics of the mixed powders without mutual solubility are a quadratic function of the mixing ratio. The number of similar types of A-A or B-B contacts, compared with the number of A-B contacts, determines the behavior of the system exclusively. With the same proportions by volume C_A and C_B (assuming equal particle size and shape), and the same statistical distribution, the A-B contacts are the most frequent and their influence on the overall sintering behavior is a maximum. Pines [Thu67] expressed the shrinkage ε by the following equation:

$$\varepsilon = \varepsilon_A C_A^2 + \varepsilon_B C_B^2 + 2\varepsilon_{AB} C_A C_B \tag{2.34}$$

with

$$C_A + C_B = 1$$

where ε_A and ε_B represent the shrinkage at A-A and B-B contacts, respectively. ε_{AB} is the shrinkage due to the A-B contacts. With an inert component (B), which does not sinter,

e_B and e_{AB} can become zero. This quadratic concentration dependence of the shrinkage was found in some insoluble oxide mixtures such as Cr_2O_3-SiO_2 and $MgCr_2O_4$-Mg_2SiO_4 [Goo62].

2.2.4 Green Microstructure Control

The microstructure determined during the sintering of ceramic materials are determined to a large extent by the powder characteristics (e.g., particle size, size distribution, shape, degree and state of agglomeration, and chemical composition) and green microstructure (e.g., green density and pore size distribution). Factors in processing which influence densification behavior are reviewed in this section.

2.2.4.1 Control of powder characteristics. Hard agglomerates (or aggregates) are present in most commercial powders. Aggregates are detrimental to powder consolidation and sintering [Rho81, Dyn83, Dyn84]. The effect of aggregates on the compaction behavior of alumina powder was investigated by Dynys and Halloran [Dyn83]. They found that dry-pressed compact densities decreased with increasing amount of aggregates. Occhionero and Halloran [Occ84] found that green density affects the pore size distribution of sintered body and that high green density delays the onset of grain growth.

Rhodes [Rho81] investigated the effects of aggregate size on the sintering behavior of yttria-stabilized zirconia and showed that the sintered density decreased with increasing agglomerate size. He also demonstrated that full

density could be obtained at low sintering temperature by using high green density (~74%) compacts which were consolidated from agglomerate-free fine powders. In addition to Rhodes' work, recent studies have suggested that improved green microstructure obtained by colloid processing can lead to the stability of the microstructure against exaggerated grain growth and significant reduction of sintering time and temperature [Bar82, Sacks84a, Sacks84b, Yeh89]. Particularly, Sacks and coworkers demonstrated that further improvement in green density and sintered density can be achieved by breaking down soft agglomerates in aggregate-free powders [Sack85, Sac88, Yeh89].

Relatively few studies have been carried out on the effect of packing on densification behavior of whisker/particle composites. In a study by Porter et al.[Por87], Al_2O_3/SiC whisker compacts were prepared using pressure filtration (or pressure casting). By varying the consolidation pressure and suspension pH, green relative densities in the range of 59-65% were obtained. The samples were subsequently hot pressed to near-theoretical density. Ishii and Bowen [Ish88] could sinter Al_2O_3-SiC whisker (15 wt%) composite to 95.5% at 1725°C for 20 min. using the samples prepared by pressure filtration of well-dispersed suspension. However, they decreased whisker size by ball-milling for 68 hr. It is likely that the reduced whisker size enhanced the densification of composites. Takao et al. [Tak87] have reported that Si-SiC whisker can be consolidated

to 53 % relative density using pressure filtration technique. Rojas [Roj88] achieved quite high green density values (~68% relative density) for Al_2O_3/ZrO_2/SiC whisker composites by slip casting well-dispersed suspensions and obtained high sintered density (94-99%) after sintering at 1700°C for 30 min.

2.2.4.2 Suspension processing. A suspension consists of particles/whiskers suspended in a liquid medium (e.g., water). Suspension processing was extensively used in the present study for powder/whisker tailoring and for fabricating homogeneous green compacts for sintering study. Since complete and detailed discussions on suspension processing can be readily obtained in the literature [Par73, Hie77, Hun81, Hun87], only a general review on suspension processing will be presented. Since the particles, if small enough, will be undergoing Brownian motion, they tend to flocculate to achieve a lower free energy state. The particles can remain as individual particles for an appreciable time only if some mechanism prevents flocculation (or aggregation) during a collision. These can be accomplished in two ways:

(a) the particles can be given an electric charge (either positive or negative) and if all have the same charge they will repel one another when they approach (electrostatic stabilization);

(b) the particles can be coated with an adsorbed layer of some material (e.g., polymer), which itself

prevents their close approach (steric stabilization).

The discussion that follows will be limited to electrostatic stabilization since this was primary stabilization mechanism used in this study.

A. Surface charge development. Understanding the structure of the interfacial region is of great importance in understanding the stability/flocculation of solid/liquid dispersions. There are four major mechanisms by which charge can be developed at the solid/liquid interface:

(a) Adsorption of ionized surfactants/electrolytes from the solution. For example, citrate ions can selectively adsorb on the alumina particle surface to give a net negative charge, in a alumina suspension containing sodium citrate.

(b) Non-stoichiometric dissociation/adsorption at the surface of an ionic solid (e.g, silver iodide/water system).

(c) Isomorphic substitution (e.g., clay/water system).

(d) Adsorption/dissociation of hydroxyl and hydrogen ions. This mechanism is the major charge development mechanism for most oxide materials.

With oxide materials such as alumina and silica, dissociation of surface OH groups occurs, and the surface may become positively or negatively charged depending on the pH, i.e.

$$M\text{-}OH(surface) + H^{+}(solution) = M\text{-}OH_2^{+}(surface)$$

$$M\text{-}OH(surface) + OH^-(solution) = M\text{-}O^-(surface) + H_2O(solution)$$

A unique pH can be defined at which the surface charge is zero. This is referred to as the point of zero charge (p.z.c.). If there is no specific adsorption, the point of zero charge is equivalent to isoelectric point (i.e.p.) which is defined as the pH at which the electrophoretic mobility is zero.

B. Electrical double layer and repulsive force. As a result of charge separation, an electrical double layer is established. The double layer consists of a surface charge, which is compensated by counterions. As a result of thermal motion, the counterions are diffuse in nature, which is opposite and equal to surface charge by electron neutrality. Some counter ions may physically adsorb on the particle surface due to the electrostatic attractive force (Stern layer), whereas the other counter ions form a diffuse layer outside the Stern layer. The combination of the charged particle surface and the surrounding counter ions in the diffuse layer is called an electrical double layer.

When two charged particles approach each other and overlap, repulsive force is produced due to the increase in the osmotic pressure or the increase of free energy. For two flat plates separated by distance d, the repulsive energy per unit area, V_R, can be approximated by the following equation:

$$V_{R(plate)} = \frac{64 n_o kT}{\kappa} \left[\frac{\exp(Ze\psi_o/2kT) - 1}{\exp(Ze\psi_o/2kT) + 1} \right]^2 \exp(-\kappa d) \qquad (2.35)$$

where n_o is the bulk ion concentration (number if ions/volume), k is the Boltzmann constant, T is the absolute temperature, Z is the valence of ions in a symmetrical electrolyte, e is the elementary charge, ψ_o is the surface potential (which is the potential at the Stern layer to represent the surface potential), κ is the Debye-Huckel parameter (i.e., the reciprocal of the thickness of the diffuse layer in the electrical double layer) which is given by:

$$\kappa^2 = \frac{e^2 \sum (n_{io} Z_i^2)}{\varepsilon_r \varepsilon_o kT} \qquad (2.36)$$

where n_{io} is the bulk concentration of ions of type i, Z_i is the valence of the ion i, ε_r is the relative dielectric constant, and ε_o is the permittivity of vaccum.

In the case of two interacting spherical particles with large κa (i.e., particle radius, a, is relatively large compared to the thickness of the double layer), the total repulsive energy can be approximated by the following equation:

$$V_{R(sphere)} = \frac{64\pi a n_o kT}{\kappa^2} \left[\frac{\exp(Ze\psi_o/2kT) - 1}{\exp(Ze\psi_o/2kT) + 1} \right]^2 \exp(-\kappa d) \qquad (2.37)$$

From the above equation, it is clear that the major parameters which determine the repulsive force as a function of interparticle separation distance are the ionic strength (i.e., valence of ions and ion concentration), the particle size, and surface potential. In practice, a near-surface potential is used instead of surface potential.

C. Total interaction energy (DLVO theory). Degree of dispersion is dependent upon not only repulsive force but also ever-present van der Waals attraction. According to DLVO (Derjaguin-Landau-Verwey-Overbeek) theory [Ove52, Hunt81, Hunt87], the total interaction energy (VT) is given by the sum of van der Waals forces (VA) and the electrostatic repulsive interaction (VR):

$$V_T = V_R + V_A \tag{2.38}$$

where $V_A = -A/(12\pi d^2)$ for the two flat plates and $V_A = -Aa/(12d)$ for the two spheres and A is the Hamaker constant. The negative sign indicates that the force is attractive.

A typical schematic plot of the total interaction energy as a function of separation distance between two surfaces is shown in Figure 2.12 [Hun87]. It should be noted that the van der Waals attraction always dominates at both large and small separations. However, it may be too weak to be of significance at large separation. At small separations, V_R must approach a finite magnitude, whereas V_A increases very markedly and hence is expected to pull the surfaces into a deep attractive well, called the primary minimum. The secondary minimum at large separations is due to the more rapid decay of electrostatic repulsion relative to van der Waals attraction. At intermediate separations, the electrostatic repulsive force may dominate. Thus, a potential maximum can be obtained at the intermediate separations with sufficient electrostatic repulsions and moderate ionic strengths.

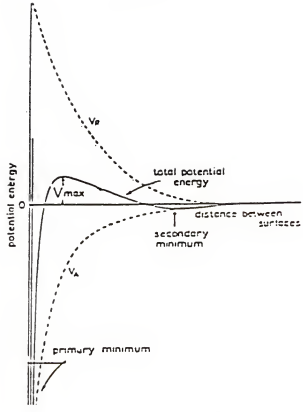

Figure 2.11 Qualitative sketch of potential energy versus separation between two parallel plates.

If the maximum potential (V_{max}) is much greater than the thermal energy of the particles (i.e., $V_{max} >> kT$), the potential barrier can prevent particles from permanent contacts when they encounter due to Brownian motion. In this case, the suspensions have good stability against flocculation. On the other hand, low zeta potential or high ionic strength can result in an absence of an energy barrier. This will result in flocculated suspensions.

In practice, the suspensions used for forming operation contain relatively high solids loading. When electrostatic stabilization (e.g., typically by pH adjustment) is used for preparing suspensions with high solids loading, controlling both zeta potential and ionic strength is very important [Sac88a, Roj88, Yeh89]. Therefore, in a given solid/liquid system under electrostatic stabilization (i.e., pH adjustment), a compromise between high zeta potential and low solution ionic strength results in maximum suspension stability against flocculation (i.e., well-dispersed suspension). The well-dispersed suspension produces a homogeneous green microstructure with high density and small pore channel radius [Sack85, Roj88].

2.2.4.3 Packing of whisker/particle mixture. Although there has been a lot of interest in the physical properties of whisker/particulate composites, only limited studies have been reported on the packing behavior of these composites. As discussed in section 2.2.3, the anisotropic shape of whiskers greatly reduces the packing efficiency of whisker composites. It is necessary to first determine the packing behavior of fibers (or whiskers) in order to evaluate their effect on packing behavior in powder/fiber (or whisker) mixtures. Figure 2.12 shows that the relative density of fiber compacts decreases dramatically with increasing aspect ratio. Another very important phenomena with high aspect ratio fibers is that for aspect ratios between 25 and 40, packing structure

of fibers changes (i.e., bundling and clumping develops.) [Mil86].

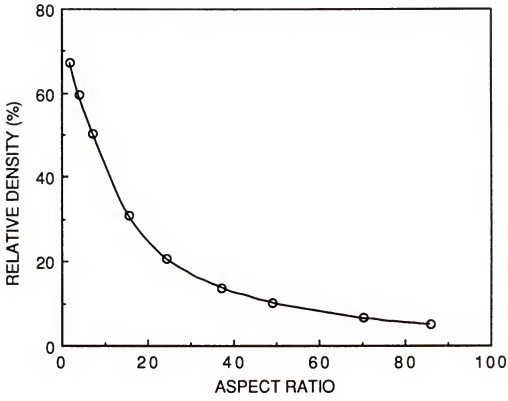

Figure 2.12 Packing curve for fibers with varied L/D ratios [Mil86].

Milewski [Mil78; Mil86] suggested that packing density of fiber/particle mixtures can be increased as the fiber aspect ratio decreases and the ratio of the particle diameter/fiber diameter, R, approaches either zero or infinity. Using bimodal packing theory, the packing density of whisker/particulate mixtures can be predicted, assuming that the mixture is homogeneous and each constituent achieves its maximum packing density. Figure 2.13 shows the

theoretical packing curve when the matrix particle size is infinitely small compared to fiber diameter (R=0). It is further assumed that the matrix packing follows random close packing and the whisker aspect ratio is 20. From Figure 2.12, the packing density of whisker alone is estimated to be ~25% (i.e. relative bulk volume = 4.0). The packing density of particulate is assumed to be 63.7% with random close packing.

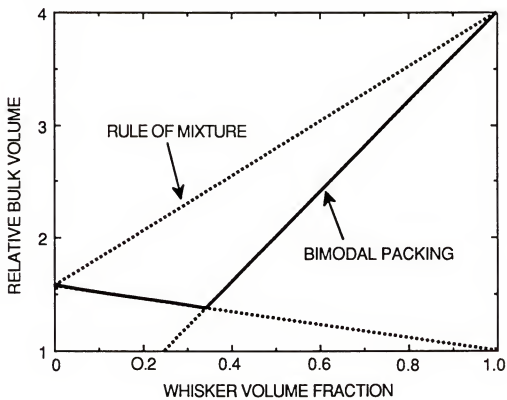

Figure 2.13 Theoretical packing of whisker-particulate system [Mil86].

The composition of optimum packing (minimum relative bulk volume) predicted for the homogeneously compacted mixture can be determined as following [Smi84]:

$$y = P/(P+W-1) \qquad (2.39)$$

where y is the volume fraction of whisker, P is the relative bulk volume of particulate component, and W is the relative bulk volume of whisker. Therefore, the minimum relative bulk volume (i.e. maximum relative packing density) can be obtained in the particulate-rich side as follows:

$$V_{min} = \frac{WP}{W+P-1} \tag{2.40}$$

In the above instance, the maximum relative density (72.7 %) can be obtained at 0.343 whisker volume fraction. However, the theoretical packing can never be achieved because of the finite size of the matrix particles and incomplete mixing and dispersion. Since most experimental data show a large discrepancy compared to theoretical predictions, Milewski [Mil78] introduced the concept of packing efficiency. The packing efficiency (PE) is defined as follows:

$$PE = \frac{V(RM) - V(exp)}{V(RM) - V(th)} \tag{2.41}$$

where V(exp) is the experimentally determined relative bulk volume, V(th) is the value obtained from bimodal packing theory, and V(RM) is the value calculated from the rule of mixtures.

Gac et al. [Gac84] suggested that the critical aspect ratio for toughening with SiC whisker was 20 for a glass matrix and 12 for hot-pressed silicon carbide matrix. Once the critical aspect ratio is reached, the additional toughness due to higher aspect ratio is negligible [Mil86]. Considering the effect of aspect ratio on the packing

behavior of whiskers and composites (Figure 2.14 and 2.15), it is imperative to optimize the whisker aspect ratio and diameter ratio R.

When we deal with multiphase systems, mixing and dispersion can be a very important problem. When materials have greater differences in particle size, geometric shape, and true density, the problem of achieving good mixing and co-dispersion becomes more serious. Thus, special precautions need to be taken in processing to achieve maximum homogeneity and dispersion.

2.2.5 Infiltration of Liquid into Porous Compact

As discussed in section 2.2.3, composites with a high volume content of whiskers are essentially impossible to sinter to near theoretical density with conventional processing techniques due to the extensive network structure of whiskers throughout the matrix phase. Even with optimum packing behavior of particles and whiskers, densification of composites with >20 vol% whiskers is severely inhibited since the network structure of the whiskers controls the densification behavior [Tie87b]. One alternative for enhancing densification is to increase green density and consequently minimize the shrinkage necessary for full densification. Since less shrinkage is required, the amount of newly forming whisker clusters can be reduced. This can be accomplished by infiltration processing [Sacks88].

Pressureless infiltration into porous ceramics has been carried out using molten metal, sols, organometallics, and molten precursor salt [Hil80, Gla87, Sacks88, Mar88]. In the case of molten salt, the material heated to the melting temperature and subsequently infiltrated into the porous compacts. Subsequently, the infiltrated compact was heat-treated in order to convert the infiltrant material to a desired phase. In this study, aluminum nitrate nonahydrate (ANN: $Al(NO_3)_3 \cdot 9H_2O$), which can be decomposed to alumina upon subsequent heat treatment, was infiltrated into Al_2O_3/SiC whisker green compact. Several important processing variables in the infiltration operation will be discussed below, including compact infiltration kinetics and phase transitions during heat treatment of ANN.

2.2.5.1 Kinetics of infiltration. In the infiltration processing, two quantities are important to maximize the infiltration efficiency. These are the volume percent of the infiltrated second phase and the infiltration rate. The volume percent of infiltrated phase is expected to be controlled by the relative density of the powder compact (G), the density of infiltrant (ρ_i), the density of the compound formed after decomposition of the infiltrant (ρ_c), the relative mass change on decomposition of the infiltrant or evaporation of the solvent (L), and the degree of filling of the pores (F). The volume percent of the infiltrated second phase (V_v) can be given by the following expression [Gla87]:

$$V_v = \{1 + G(\rho_c/\rho_i)/[F(1-L)(1-G)]\}-1 \qquad (2.42)$$

The penetration of a fluid into a cylindrical channel of radius, r, under the force of capillarity is given by the following equation:[82]

$$d^2 = \frac{rt\gamma \cos\theta}{2\eta} \qquad (2.43)$$

where d is the liquid penetration depth, γ is the surface tension of liquid, θ is the contact angle, t is time and η is the viscosity of infiltrant. The above equation does not account for the distribution of pore channel radius, tortuosity of the pore channels, the presence of closed pores, etc.; it is, however, expected to provide a rough estimation of the infiltration depth. It is evident from equations (2.60) and (2.61) that appropriate infiltrant should have low viscosity, good wettability (i.e. low contact angle), and high solid yield. In addition to these requirements, the infiltrant must be easy to convert to the desired solid phase at low temperature (e.g., to avoid adverse chemical reactions that might occur at high temperatures, etc.).

2.2.5.2 Melting and Decomposition of ANN. Aluminum nitrate nonahydrate (ANN: $Al(NO_3)_3 \cdot 9H_2O$) decomposes in very complex way. It involves both liquid solution and solid phase reactions in a multi-step process that leads to intermediate stable and metastable products, over a broad temperature range, until the thermodynamically stable α-Al_2O_3 is reached at high temperatures. The thermal decomposition starts with

dehydration. Upon heating the nonahydrate, it decomposes to an octahydrate and/or a hexahydrate at 60-62°C, and the hexahydrate is stable up to 129°C [Cim83]. The reported melting point of 73.5°C is the process involved in melting or dissolution of hexahydrate in its own water of crystallization [Sat78] Kuklina showed that an amorphous phase (by XRD) is obtained by calcination in air at 300°C for 6 hours [Kuk73]. The amorphous phase transforms to γ-Al_2O_3 at around 850°C and the γ-Al_2O_3 is stable up to 900°C until the appearance of α-Al_2O_3. The α-Al_2O_3 exist along with γ-Al_2O_3 at 900°C before complete transition to α-Al_2O_3 at ~1100°C. It was suggested that nitric acid is chemisorbed to the alumina surface and acts as a mineralizer and appreciably lowers the temperature of the phase transition from γ to α-Al_2O_3. It has also been shown that a transition from γ-Al_2O_3 to α-Al_2O_3 occurs only when a critical transient crystallite size (i.e., ~20 nm) is reached at a specific temperature [Kuk73].

2.2.6 Liquid Phase Sintering

Tiegs and Becher [Tie87b] used MgO and Y_2O_3 as liquid phase sintering additives in sintering Al_2O_3/SiC whisker composites. They increased the sintered density of 90% Al_2O_3/10% SiC whisker composite from 70.9% to 91.8% with the addition of 0.5 wt% MgO and 2 wt% Y_2O_3. Barclay et al. [Bar87] also observed an increase from 87% to 95% in sintered density for 97% Al_2O_3/3% SiC whisker composites with an addition of 0.6 wt% Y_2O_3. Microstructural analysis [Lip88; Beche86]

revealed that the addition of both the MgO and Y_2O_3 resulted in formation of $Y_3Al_5O_{12}$ and grain boundary phases containing Y, Si and Al. Furthermore, they observed some glassy phases which contained Ca and Si. The above observation indicates that surface silica and impurities from whiskers participate the formation of liquid phase. That is, the liquid phases involved appeared to be quarternary system Al_2O_3-SiO_2-MgO-Y_2O_3. However, MgO disappeared at the sintering temperature [Beche86 because MgO has quite high vapor pressure under reducing atmosphere [Bhe84]. Since MgO was disappeared at high sintering temperatures under reducing atmosphere, the liquid phase is expected to consist of Al_2O_3-SiO_2-Y_2O_3. Boskovic et al. [Bos87] densified Al_2O_3 powder compact to near full density with addition of 2 wt% liquid. The composition of the liquid phase was 35% Y_2O_3-21.5% Al_2O_3-44% SiO_2. They also observed the presence of $3Y_2O_3 \cdot 5Al_2O_3$ which is consistent with the observation of Becher et al.[Bec 86].

There are three stages in the classical theory of liquid phase sintering; (1) particle rearrangement, (2) solution-reprecipitation, and (3) coalescence [Kin 59].

2.2.6.1 Rearrangement. The theory of liquid phase sintering processes is usually based on the assumption that the liquid phase wets the surface of the solid particles and the solid substance is dissolved in the liquid. The wetting of the solid particles by the liquid between them results in curved liquid meniscus surfaces on which capillary forces act,

tending to draw the particles together. The interparticle force F between two spheres connected by a liquid bridge

$$F = 2\pi r\gamma_{LV}\cos\phi - \pi r^2 \gamma_{LV}(1/r+1/\rho) \qquad (2.44)$$

consists of a surface tension term acting at the wetting perimeter $2\pi r$ and a term arising from the capillary pressure ΔP in the liquid.[Hup75] Here γ_{LV} is the surface free energy of the liquid-vapor interface, r the radius of the liquid ring, ρ is the second radius of curvature of the liquid meniscus, and ϕ is the angle defining the center-center component of the surface tension force pulling particles together (ϕ is dependent upon contact angle). The shrinkage in the initial stage of liquid phase sintering is explained by the redistribution and concentration of particles toward the center of the compact due to the interparticle force under the surface tension of the liquid.

After establishing a relatively stable packing arrangement of the solid particles further lowering of the free energy of the packing may then occur by redistribution of the liquid [Sha86b]. The two-pore-size model by Shaw predicted that the pores of smallest coordination numbers will be the first to fill, and only if there is sufficient liquid will pores of higher coordinations start to fill. With relatively small amounts of liquid, it is still possible that pore filling process can contribute to densification by liquid redistribution. The liquid will be located at isolated necks between the particles before shrinkage starts. After certain amount of shrinkage has occurred, it will become

favorable to start filling the pores of the smallest coordination number with liquid. Slightly larger pores may only start filling with liquid once all the pores with the smallest coordination numbers are filled and further shrinkage has occurred.

The necessary shrinkage can be provided by two processes depending on the amount of liquid. One way to provide shrinkage is to achieve densification by capillary force and another is to densify by solid state sintering in the liquid-free regions. The inhomogeneous distribution of liquid arises because there are more contacts per particle and finer pores in the denser regions of compact. As sintering proceeds, liquid tend to be transferred out of the denser regions and to fill larger pores in the distribution. In the final stages of sintering, there will tend to be more liquid in the regions where the particles are less densely packed. Consequently, the compositional homogeneity of a liquid-phase-sintered material depends not only on the initial distribution of liquid forming additives but also on the homogeneity of packing of the powder and the ease with which the liquid can redistribute (i.e. wettability and viscosity) On the other hand, Park et al. suggested that pore filling process could proceed with grain coarsening which occurs by solution-reprecipitation (Oswald ripening) [Par84].

Nonetheless, if the pore size distribution contains a fraction of large pores, the large pores will be the last to fill with liquid during sintering and will fill only when the

radius of curvature of the meniscus has increased to a certain value. An increase in meniscus corresponds to a decrease in the driving force for sintering. Consequently, there will be a relatively low driving force for the elimination of the large pores. As a result, it may not be possible to eliminate such pores by sintering alone. In order to maintain a high driving force for sintering, it is desirable to have as large fraction of small pores as possible. In general, this means that high powder packing densities must be achieved. As discussed in the previous section, this can be accomplished by suspension processing.

2.2.6.2 Solution-reprecipitation process. This process is one of the densification processes with small amount of liquid. As long as there is a difference in radii of curvature, chemical potential gradients can be maintained throughout liquid phase sintering. The solubility of a substance increases with decreasing radius of curvature of the particles. For spherical surfaces

$$\ln\left[\frac{C}{Co}\right] = \frac{2\gamma_{SL}\, V_o}{rRT} \qquad (2.45)$$

where C/C_o is the ratio of the solubility of fine particles with a radius r and large particles with a radius $r_o \rightarrow$ infinity (i.e. plane interface), γ_{SL} is the specific free surface energy at the solid-liquid interface, V_o is the molar volume, R is the gas constant, and T is absolute temperature. Thus, fine particles are gradually reduced in size during sintering

and dissolve in the liquid phase, while at the same time, due to the lower solubility of the large particles, an excess of the substance in solution is reprecipitated on the large particles, thereby still further increasing their size [Ere70]. The solution-reprecipitation process is responsible for many phenomena during liquid phase sintering including grain growth (by Ostwald ripening), shape accommodation, and particle disintegration. Although densification in this stage is relatively slow compared to the rearrangement process, solution-reprecipitation process is indispensable for full densification when the amount of liquid is small. This sintering mechanism occurs in systems whose components are fairly soluble (i.e., solid phase is readily soluble in the liquid phase). The following conditions are necessary for this mechanism to occur: (1) a substantial difference in the melting point of the components; (2) insolubility (or low solubility) of the low-melting component in the high-melting component; (3) solubility of high-melting component in the low-melting component. During solution-reprecipitation process, the growing large particles also adjust to each other's shape in order to acquire shape appropriate for close packing (i.e., shape accommodation). Consequently, partial solution and rupture of contacts between particles are necessary for the particles to come closer together (particle disintegration) [Pet82].

Another important condition for the occurrence of the solution-reprecipitation process is the penetration of the

liquid between the grains. The extent to which the liquid enters the joints between the particles depends on the dihedral angle formed by the liquid phase at the boundary with two grains of the solid phase. Under equilibrium conditions this angle can be expressed as

$$\gamma_{SS} = 2\gamma_{SL} \cos(\phi/2) \qquad (2.46)$$

where γ_{SS} is the interfacial energy at the boundary between two grains, γ_{SL} is the interfacial energy at the boundary between the solid and liquid phases, and ϕ is the dihedral angle. The analysis of the above equation shows that the liquid will penetrate along the boundary separating the grains of solid phase if $2\gamma_{SL} < \gamma_{SS}$. If liquid does not flow completely into the joints between the particles, neighboring particles of the solid phase may bond together. Consequently, rapid densification corresponding to liquid phase sintering are negligible and densification rate should decrease to almost that of the solid state sintering condition.

2.2.6.3 Application of LPS to Al_2O_3/SiC whisker composites.

Since most liquid phases are detrimental in high temperature application, very limited amount of liquid phase has been used in sintering of these composites. With limited amount of liquid, it is impossible to expect full densification by rearrangement process alone. However, liquid phase will enhance densification of the composites by facilitating stress relaxation in the alumina matrix due to the low shear viscosity of liquid phase. Considering

microdensification around whiskers, the amount of liquid phase necessary for full densification of composites is dependent on the whisker content. Since limited amount of liquid phase may be used in the sintering of the composites, the homogeneous distribution of liquid phase sintering additives is important in order to maximize the effect of liquid phase on densification. Nonetheless, it is expected that the liquid phase sintering will result in enhanced densification up to the moderate whisker concentrations with relatively small amount of liquid phase if the high density homogeneous green microstructure can be achieved.

2.3 Strategies

In order to fabricate reliable alumina-based materials, two approaches were used - whisker reinforcement and suspension processing. Previous researchers [Wei85, Cla86, Tie87b] have shown that the whisker reinforcement in the alumina ceramics can lead to two-to-three fold increases in fracture toughness. Suspension processing has been used to produce pure alumina ceramics with ~1 GPa due to the reduced flaw sizes.

The presence of non-sintering whiskers in the alumina matrix results in either a development of tensile hydrostatic stresses in the matrix or the formation of whisker network structures. This significantly reduces the densification rate of alumina matrix. Thus, most whisker composites were

fabricated by hot pressing to overcome this problem. However, there is a strong desire to fabricate intricate parts with close tolerance through pressureless sintering.

A number of strategies were used in this study in order to enhance densification during pressureless sintering of whisker/particulate composites:

(1) Improving Green Microstructure. In order to obtain homogeneous green compacts with high density and small pore size, powder/whisker characteristics, suspension properties, and consolidation condition were optimized. In addition, infiltration was used to increase green density. This can minimize new whisker-whisker contacts during sintering by reducing required shrinkage.

(2) Reducing Whisker Length and Aspect Ratio. Whisker characteristics were tailored using fluid classification. However, this approach may not result in as good mechanical properties.

(3) Using Liquid Phase Sintering. Liquid phase can enhance densification of composites in which particle/whisker rearrangement and shape accomodation processes may reduce tensile hydrostatic stresses deveopled by whiskers. However, this approach may decrease high temperature mechanical properties of composites.

(4) Control of Sintering Condition. Sintering was carried out in the atmosphere in which whiskers are

actively protected against oxidation using protection powder.

CHAPTER 3
EXPERIMENTAL PROCEDURE

3.1. Powder Preparation and Characterization

3.1.1 Alumina Powder Preparation

The matrix phase in the composite samples was high-purity α-Al_2O_3.[a] For some experiments, agglomerate-free powders were prepared by a gravity sedimentation process in which coarse particles (e.g., agglomerates) were removed from the as-received Al_2O_3 powders. In this case, dilute (~2.5 vol%), well-dispersed suspensions were allowed to settle in cylindrical tubes for several days in which the cut-off particle diameter was predicted by Stokes' law

$$v_t = \frac{(\rho_s - \rho_l)\, g}{18\eta}\, d_{st}^2 \qquad (3.1)$$

where v_t is terminal velocity of particle, ρ_s and ρ_l are the densities of solid and fluid, respectively, g is gravitational acceleration, d_{st} is Stokes' diameter, and η is viscosity of fluid. Good dispersion was achieved by pH adjustment (3.5-4.0) [Roj88, Sac88, Yeh89] and

---

a AKP-50, Smitomo Chemical America, Inc., New York, NY. RCHP-DBM, Reynolds Metal Co., Chemical Div., Little Rock, AR.

ultrasonication.[b] The unsettled (fine) fraction of the suspension was collected, concentrated by filtration or centrifugation[c], washed with deionized water 4~5 times, dried at ~50°C, and stored for later use. The powders prepared with this process were designated Al_2O_3-8 for RCHP-DBM and Al_2O_3-11 for AKP-50 powders, respectively. The detailed procedures for preparing these powders are given in the Appendix.

In other experiments, an alternative fractionation method was used. Coarse particles were removed from dilute, well-dispersed suspensions using a continuous-flow centrifugal sedimentation.[d] In the centrifugal sedimentation, the cut-off diameter is dependent on the geometry of centrifuge as well as centrifugal field strength (rotation speed) and feeding rate of dilute suspension as shown below [Fou80]:

$$d_c = \left(\frac{18\eta Q}{(\rho_s - \rho_l)\omega^2 V} \ln\left(\frac{r_2}{r_1}\right) \right)^{1/2} \tag{3.2}$$

where ω is the angular velocity, r_1 and r_2 is the distances from the center of rotation to top surface of sediment and liquid surface, respectively, Q is volumetric feed rate, and V is the volume of material held in the centrifuge. This fractionation process is particularly effective for very fine

b Model W-375, Heat Systems-Ultrasonics, Inc., Farmingdale, NY.

c Model J-21, Beckman Instruments, Inc., Palo Alto, CA.

d IEC Chemical Centrifuge, International Instrument Co.

particle size range compared to the gravity sedimentation process. A dilute (1.5 vol%) AKP-50 suspension was subjected to the centrifugal field at 4600 RPM with suspension feed rate of 1.6 ml/sec. Subsequently, the overflown suspension was fed to an even higher centrifugal field at 4800 RPM with suspension feed rate of 1.3 ml/sec. The overflown suspension was concentrated to ~40 vol% solids loading for future use. This powder was designated Al_2O_3-27. The powder collected inside the centrifuge container was designated Al_2O_3-19 which was redispersed at pH~4. Similarly, the RCHP-DBM suspension was fractionated by this method, resulting in agglomerate-free powder, was designated Al_2O_3-8.

In order to adjust particle size distribution of Al_2O_3, two different centrifugally fractionated suspensions (Al_2O_3-8 and Al_2O_3-19) were mixed in 1:1 solid weight ratio and concentrated to 52 vol% (designated Al_2O_3-10). All the suspensions were stored in plastic container for later use and continuously agitated in a rotary mixer in order to avoid flocculation. The detailed procedures for preparing various Al_2O_3 powders are given in the Appendix.

3.1.2 SiC Whisker Preparation

The reinforcement in the composite samples was SiC in the form of whiskers.[e] As-received Tateho and ARCO whiskers

---

[e] SCW-1 and SCW-1 S105, Tateho Chemical Industries, Hyogo-ken, Japan.
Silar SC-10, ARCO Metals Co., Greer, SC.

were designated TSC-AR and ASC-AR, respectively. The whiskers exist primarily in β (cubic) and α form (<5%). Whiskers were subjected to acid (~0.018N HNO_3 solution) and base (~0.15N NH_4OH) washes for 24 hours in order to remove leachable impurities (e.g., Ca ions) and to improve the dispersibility of whiskers in water. The acid or base was removed by repeated washing with deionized water before subsequent processing. For most of the experiments, whiskers were fractionated by gravitational sedimentation in order to remove large whisker agglomerates (clusters) and/or very fine particles. The designations TSC-F and ASC-F are used for fractionated Tateho and ARCO whiskers, respectively. Attempts were made to separate whiskers into three fractions with different length and aspect ratio using a combination of gravitational and centrifugal sedimentation. Suspensions used for fractionation were dispersed by pH adjustment (pH~10.5) and ultrasonication. The suspension was subjected to a centrifugal field of 800 RPM and with a suspension feed rate of 3.5 ml/sec. The sediment inside the centrifuge container was redispersed, then subjected to a gravity sedimentation in order to remove whiskers finer than 1 μm equivalent spherical diameter. The overflown suspension was subjected to the second centrifugal fractionation process at 350 RPM with suspension feed rate of 10 ml/sec. The cake inside the container was redispersed, then settled in order to eliminate the fine whiskers (< 1 μm). This whisker was designated TSC-B fraction. The overflown suspension was combined with the fine

whisker (<1 μm) suspensions which were removed by a gravity sedimentation. The combined whisker fraction was designated TSC-C. After fractionation, suspensions were filtered, washed with deionized water, dried at ~50°C for 48 hr, and stored for later use. The detailed procedures for preparing whiskers with various size characteristics are given in Appendix.

3.1.3 MgO and Y_2O_3 Powder Preparation

MgO and Y_2O_3 are the common sintering additives for Al_2O_3, and form liquid phases at the sintering temperature which enhance densification [Bur57]. In SiC whisker/Al_2O_3 composites, additional liquid phases might form due to the presence of SiO_2 on the whisker surfaces.

Y_2O_3 powder was synthesized by a precipitation method. 0.4 M stock solution was prepared by dissolving 7.75 g $Y(NO_3)_3 \cdot 6H_2O$[f] in 50 ml of deionized water. The above stock solution was mixed with 13 g urea[g] in 750 ml of deionized water. The mixed solution was boiled in closed system for 2 hr under constant stirring. Within minutes after boiling, turbidity increases as powder precipitates. The precipitated powder was filtered, washed with deionized water, and calcined at 900°C for 24 hr in air. The calcined powder was ground with mortar and pestle. The ground powder was dispersed in ethanol (1 vol% solids loading) and ultrasonicated for 1 hr. Subsequently, the suspension was

---

f Yttrium nitrate, Fisher Scientific, Springfield, NJ.

g Urea, Fisher Scientific, Springfield, NJ.

subjected to a gravity sedimentation process in a 100 ml graduated cylinder. The sedimentation process was repeated 5 times to ensure that most hard agglomerates were eliminated.

Commercially available MgO[h] was classified using gravity sedimentation technique in ethanol similarly to Y_2O_3 classification. The classification conditions for both powders were aimed at achieving the cut-off Stokes diameter of 0.5 μm. The subsequent steps for filtration, washing and drying were similar to those of alumina.

3.1.4 Characterization of Powders

The Al_2O_3 and SiC whiskers were characterized by a variety of techniques. Specific surface areas were measured using nitrogen gas adsorption[i] (multipoint BET method). Powder true densities were determined by helium gas pycnometry.[j] X-ray sedimentation[k] and centrifugal photosedimentation[l] were used to determine the Al_2O_3 particle size distribution (i.e., Stokes diameter distribution).

For SiC whiskers, lengths and diameters were directly measured using enlarged micrographs from scanning electron

---

h MagChem 40, Martin Marietta Chemicals, Hunt Valley, MD.

i Model OS-7, Quantachrome Corp., Syosett, NY.

j Model PY-5, Quantachrome Corp.

k Sedi-Graph Particle Size Analyzer, Micromeritics Instrument Corp., Norcoss, GA.

l Model CAPA-700, Horiba Instruments, Inc., Irvine, CA.

microscopy.[m] Samples were prepared from suspensions which were dispersed by ultrasonication and pH adjustment, and diluted to ~10 ppm to minimize agglomeration of the whiskers during drying. In addition, in order to avoid formation of flocs during drying, a polymer (PVA) solution (~0.6 mg PVA/m^2 SiC) was employed [Kha88]. The polymer may provide a steric barrier against direct contacts between whiskers.

Measurements were made at magnifications in the range of ~24000 to 33000 for diameter determinations and ~1600 to 2500 for length determinations using digitizing tablet with computer. A minimum 12 randomly selected fields of view were used for each size measurement. The number of counts made to obtain average values was >500 for the diameter and >750 for the length. The average aspect ratio of whiskers was estimated by dividing the average length by the average diameter. Note that the whisker size measurements obtained by microscopy are collected on a number basis; in contrast, the Al_2O_3 size measurements obtained by X-ray sedimentation are collected on a weight basis.

However, attempts were made to obtain the size information of whiskers on the basis of volume, since most properties of whisker containing composites are significantly affected to the volume fraction. Since the distribution of whisker diameter was relatively narrow, it is a good

---

[m] Model JSM-35F, Japan Electron Optics Co., Ltd., Tokyo, Japan.

approximation to relate length-frequency of the whiskers of a given aspect ratio to their volume frequency. Average whisker length values based on length-frequency are obtained along with those based on number frequency.

3.2. Suspension Preparation

3.2.1 Electrokinetic Measurement

Microelectrophoresis[n] was used to measure the electrokinetic mobility of Al_2O_3 particles and SiC whiskers (TSC-C). Dilute suspensions were prepared by mixing ~300 ppm powder with deionized water. The pH was adjusted using nitric acid or ammonium hydroxide and suspensions were aged for 24 hr prior to the electrophoresis measurements. At each pH, a minimum of 40 individual measurements were taken at several field strengths to obtain an average electrophoretic mobility value. The zeta potential was calculated from the average mobility using the Helmholtz-Smoluchowski equation:

$$\zeta = \frac{\mu \eta}{\varepsilon \varepsilon_o} \qquad (3.3)$$

where η is viscosity of the suspending liquid (in Pa·s), ε is relative dielectric constant of the suspending liquid, ε_o is permittivity of vacuum (in 8.854×10^{-12} F/m). For aqueous dispersion at 25°C, equation (3.3) can be written:

$$\xi = 12.83\ \mu \qquad (3.4)$$

---

n Mark II, Rank Brothers, Cambridge, UK.

where ξ is the zeta potential in mV, and m is the electrophoretic mobility in (μm/sec)/(volt/cm).

3.2.2 Characterization of Suspensions

In order to determine the optimum co-dispersion conditions for both the Al_2O_3 and SiC whisker suspension, preliminary experiments to select dispersant and pH value were carried out. For Al_2O_3, pH adjustment as well as application of an polyelectrolyte dispersant[o] was investigated at ~50 vol% solids loading. For SiC whisker, pH adjustment along with polyelectrolyte dispersant[p] was studied with ~3 vol% solids loading. In order to screen various dispersion conditions quickly, sedimentation method was applied for SiC whisker suspensions. This is one of the simplest method to identify the dispersion condition by comparing sediment density of the suspensions. Suspension density can be expressed by the following equation:

$$\text{Sediment density} = \frac{\text{Solid Weight}}{\text{Sediment Bulk Volume}} \qquad (3.5)$$

Conditions that exhibited good dispersion were then examined in a detail using rheology[q] and Hg-porosimetry measurements.[r] For Al_2O_3, several conditions were investigated using rheology and Hg-porosimetry. Suspension rheological flow

---

o Tamol 901, Rohm and Haas Company, Philadelphia, PA.

p Daxad, W.R. Grace & Co, Lexington, MA.

q Model RV-100/CV-100, Haake, Inc., Saddle Brook, NJ.

r Models SP-100 and SP-20LV, Quantachrome Corp., Syosett, NY.

characteristics (i.e., shear stress versus shear rate behavior) were obtained using a concentric cylinder viscometer. Viscosity values, η, were determined using the relation

$$\eta = \frac{\tau}{\dot{\gamma}} \tag{3.6}$$

where τ is shear stress and $\dot{\gamma}$ is shear rate.

Composite suspensions were prepared from well-dispersed, mixed suspensions of SiC whiskers and Al_2O_3 particles. Suspensions of the individual components were prepared first, using ultrasonication to assist in breaking up powder agglomerates. The SiC whisker suspension was then added slowly to to the Al_2O_3 suspension. The mixed suspensions were concentrated to the appropriate solids loading in a water bath at 90°C under constant stirring. The overall solid concentration of the mixed suspensions ranged from 18 to 54 vol%. The composite suspensions were characterized concentric cylinder viscometer.

3.3 Green Body Preparation and Characterization

3.3.1 Optimization of Consolidation Condition

Green bodies were prepared by slip casting and centrifugal casting. In the latter method, particles in suspension were consolidated in glass tubes (~2 cm diameter)

using low-speed (<800 rpm) centrifuging[s] for 2 hours. Supernatant liquid above the consolidated samples was withdrawn with a pipet prior to drying the samples. The compacts inside the molds were dried at room temperature for 48 hr before removing the samples from molds. The removed samples were dried for 48 hr at ~80°C. Slip-cast samples were prepared by pouring suspensions into plastic or glass rings (~2cm diameter) set on absorbent plaster blocks. In both casting processes, samples were ~2 to 3 mm thick after drying. The solid loading of suspension for slip casting was varied depending on alumina particle size, whisker concentration, and dispersion condition (suspension pH).

Table 3.1 Suspension solids loading for slip casting

Whisker Content (vol%)	Matrix Powder (Suspension pH)		
	Alumina-10 (pH 4)	Alumina-10 (pH 11)	Alumina-27 (pH 4)
0	52	48	45
5	53	46	45
10	51	-	-
15	49	43	42
20	48	-	-
30	45	40	40

[s] Model HN-SII, International Equipment Co.

The suspensions prepared with alumina-8 and with various whisker fractions (TSC-A, -B, and -C) were slip cast at the 50 vol% total solids loading. The total solids loadings for other suspensions are tabulated in Table 3.1. To compare suspension processing with dry processing, several samples were formed by uniaxial dry-pressing in a steel die at 103 MPa (~15 ksi). The powders used in dry-pressing were prepared by crushing and lightly grinding the slip-cast green compacts. This process may slightly reduce the aspect ratio of whiskers compared to the corresponding slip-cast compacts.

3.3.2 Green Body Infiltration

In order to increase green density of composite compacts, an infiltration technique was used. Prior to infiltration, samples were presintered for 30 minutes at 650°C in flowing nitrogen atmosphere. Aluminum nitrate nonahydrate ($Al(NO_3)_3 \cdot 9H_2O$) was used as the infiltrant. Prior to infiltration, the samples were subjected to vacuum treatment in order to remove air from the samples. The infiltrant was melted in a separatory funnel at ~80-95°C, and subsequently applied to the evacuated samples. The samples were soaked in the infiltrant melt for ~1 hr. After infiltration, samples were dried at room temperature for ~1 hr and heat-treated at ~200°C for 30 minutes. The surfaces of the dried samples were trimmed to remove the excess of frozen salts. The trimmed samples were decomposed at 650°C for 30 minutes, and weighed in order to monitor the efficiency of pore filling with the

salt melt. The above procedure was repeated (7 times) until the efficiency of filling became very low. After 7 infiltration cycles, samples were heat-treated at 900°C for 30 minutes.

3.3.3 Characterization of Green Body

After drying, the green compacts were characterized by mercury porosimetry. The pore channel radii distribution was obtained using standard values for the mercury surface energy (484 erg/cm^2) and the contact angle (140°) under the assumption that the pores are cylindrical. The total porosity, P (i.e., the volume percentage of porosity), was calculated using relation

$$P = \frac{V_s \rho_r}{1 + V_s \rho_t} \tag{3.7}$$

where V_s is the specific pore volume (cm^3/g) and ρ_t is the true density of the powder. The measured pycnometer densities for the Al_2O_3 and SiC powders were used to calculate, by linear interpolation, true densities for samples with various powder compositions. The pore channel radii distribution was obtained using following relation:

$$r = \frac{2\gamma \cos\theta}{P} \tag{3.8}$$

In order to examine whisker distribution throughout the matrix, fracture surfaces or top surfaces were investigated by scanning electron microscopy.

3.4 Sintering

Most green compacts were sintered in an induction furnace[t] using a graphite crucible as a susceptor. Since a graphite crucible was used during sintering, sintering atmosphere was probably slightly reducing. Temperature was measured with a disappearing filament optical pyrometer. The temperature measurement was calibrated using both a W-Re thermocouple and a two-color pyrometer.[u] In order to optimize the sintering condition, several variables were considered such as sintering temperature, time, atmosphere, and protection powders. Samples were sintered at 1250-1900°C for 15-120 minutes in various sintering atmospheres and protection powder beds. Heating rate was approximately 30°C/min. After soaking at the given temperature, the samples were furnace-cooled. The sintering atmospheres consisted of argon, nitrogen, nitrogen/hydrogen mixture, vacuum. In the case of gas atmospheres, the furnace was evacuated by mechanical pump to ~10^{-3} torr, then purged with a given gas. The purging procedure was repeated prior to heat-up. The sintering was carried out with the static atmosphere of a given gas. The powder beds considered were SiC whisker bed and SiC whisker/alumina bed.

---

t Model 600-6x5IND6-25, Centorr Associates, Inc., Suncook, NH.

u MROR1535C11, Ircon Inc., Niles, IL.

3.5 Properties and Microstructures

After sintering, bulk densities and open porosities were measured by the Archimedes method using D.I. water as a suspending media. Polished sections were investigated in order to observe the distribution of whiskers throughout the matrix. Polished surfaces were thermally etched at 1200-1450°C for 30-60 minutes in argon (Table 3.2). Grain intercept size was measured by line intercept method with the measurement of more than 300 grains for each sample.

Table 3.2 Thermal etching conditions for various samples

Sintering temperature	Etching temperature (°C), etching time (min)			
	0 vol% SiC	5 vol% SiC	15 vol% SiC	30 vol% SiC
1250 °C	1200, 60	1200, 60	1200, 30	1200, 30
1500 °C	1400, 30	1400, 30	1400, 30	1400, 30
1700 °C	1450, 30	1450, 30	1450, 30	1450, 30
1800 °C	1450, 30	1450, 30	1450, 30	1450, 30

Since true density of composite samples are uncertain due to weight loss, reactions, etc., pore volume fraction was measured using point counting method. A transparent plastic sheet with 7 x 7 square grid (49 intersecting points) was overlaid on the CRT of SEM. At least 20 different fields were measured. Samples were characterized with x-ray diffraction,[v]

[v] Model APD 3720, Philips Electronic Instruments Co., Mt. Vernon, NY.

transmission electron microscopy,[w] energy dispersive and wavelength dispersive spectroscopies in order to investigate whisker/matrix interface and final phase analysis.

An indentation technique was used to determine fracture toughness [Eva76]. Since optical microscopy was used to determine the dimensions of radial cracks and impression radius, the specimen was polished with diamond paste to a 1 μm finish. The loads used were restricted to a range over which the indentation patterns remained well defined; at the lower end by the minimum requirement $c \geq 2a$ (where c is one half of the crack length and a is one half of the impression diagonal) to minimize the effect of tensile residual stress, at the upper end by chipping or by the limitation of specimen thickness. The crack dimensions were not allowed to exceed one-tenth of the specimen thickness to avoid interactions with the lower free surface. The indentations were made at least 10 times on each specimen with a Vickers microhardness tester. The hardness can be expressed as follows:

$$H = 0.47 \frac{P}{a^2} \tag{3.9}$$

where H is hardness (in $N/m^2 = Pa$) and P is load (in N), and a is a half of the impression diagonal (in m). The fracture toughness (K_c) was calculated from the semiempirical relationship [Eva76]:

---

[w] Models 200CX and 2000FX, Japan Electron Optics Co., Ltd., Osaka, Japan.

$$K_c = 0.16 \frac{H\, a^{1/2}}{(c/a)^{3/2}} \qquad (3.10)$$

CHAPTER 4
RESULTS AND DISCUSSION

4.1 Powder Characterization

Characteristics of the starting powder, e.g., particle size, size distribution, particle shape, particle aggregates, and degree of agglomeration, have a profound influence on particle packing, densification, microstructural development, and final properties. From the viewpoint of suspension processing, an ideal powder should have the attributes of small particle size, non-agglomeration, equiaxed shapes, and high purity. In order to obtain the powder with the aforementioned characteristics, powder characteristics were tailored using fluid classification techniques. In the following, the characteristics of powders used in this study are presented in detail.

4.1.1 Al_2O_3 Powder

The median Stokes diameter obtained by X-ray sedimentation, BET specific surface area, and gas pycnometer density values for various Al_2O_3 powders used in this study are given in Table 4.1. Al_2O_3 particle sizes and size distributions were tailored by gravity and/or centrifugal sedimentation techniques as described in chapter 3. Al_2O_3-8 powder was prepared by eliminating larger particles or agglomerates from the as-received Al_2O_3-7 powder (RCHP-DBM)

Table 4.1 Characteristics of Al_2O_3 Powders

Powder designation	Median Stokes diameter (μm)	Specific surface area (m^2/g)	Pycnometer density (g/cm^3)
Alumina-7	0.42	7.3	3.96
Alumina-8	0.39	8.4	3.96
Alumina-10	0.23	10.0	3.98
Alumina-11	0.14	11.4	3.98
Alumina-19	0.11	19.4	3.98
Alumina-27	0.10	26.8	3.98

using centrifugal sedimentation. The median Stokes diameter decreased from 0.42 to 0.39 mm, while the specific surface area increased from 7.3 to 8.4 m^2/g. Al_2O_3-19 and -27 powders were obtained by classifying as-received AKP-50 powder using different centrifugal sedimentation conditions (RPM and suspension feed rate). Since a powder with broad particle size distribution increases the packing density, attempts were made to broaden the particle size distribution while still satisfying the requirements for an ideal powder. Al_2O_3-10 powder with a broad particle size distribution was achieved by mixing Al_2O_3-8 and Al_2O_3-19 in 1:1 ratio.

Most of the powders used in this study had a considerable fraction of particles <0.1 μm. Gravitational sedimentation methods of size analysis are usually limited to sizes >0.1 μm because Brown motion becomes significant at finer sizes. Therefore, centrifugal photosedimentation technique has been used to obtain the details of particle size distributions below 0.1 μm. Figure 4.1(A) shows cumulative particle size distribution plots for Al_2O_3-7, -8, and -11 powders, obtained by the centrifugal photosedimentation technique. Comparison between Al_2O_3-7 and -8 powders illustrates that small portions of large particles and agglomerates were effectively removed by continuous centrifugal classification method. Figure 4.1(B) shows the plot of cumulative size distributions for Al_2O_3-10 and -27 powders. Virtually all particles greater than 1 μm had been eliminated from both of these powders. The inset in Figure

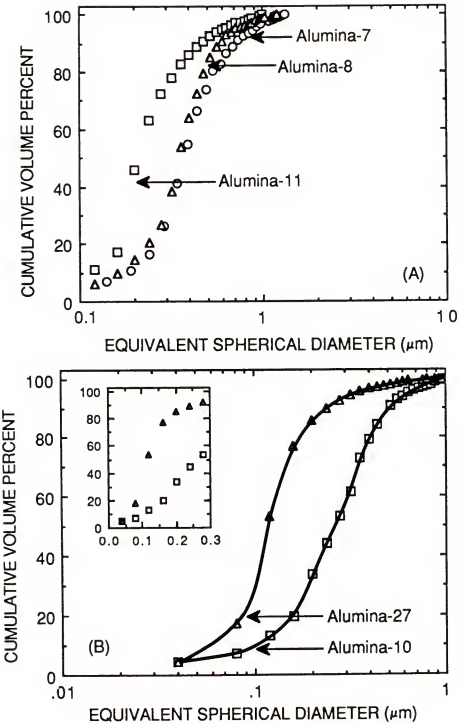

Figure 4.1 Cumulative plot of equivalent spherical particle size for (A) alumina-7, -8, and -11, and (B) alumina-10 and -27.

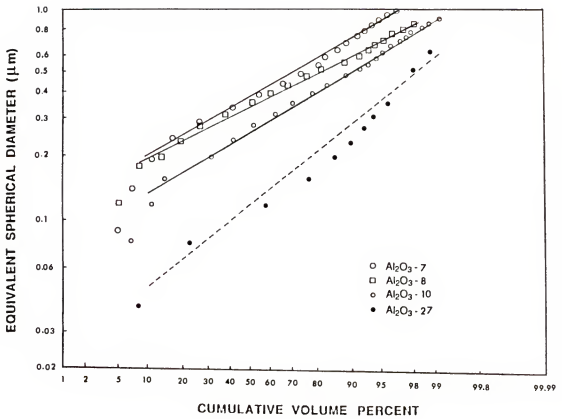

Figure 4.2 Particle size distribution plotted on a log-probability scale for the alumina-7, -8, -10, and -27 powders.

4.1(B) shows a plot on the linear scale in 0.04-0.3 μm range. Al_2O_3-27 powder has ~85 % of particles <0.2 μm, whereas Al_2O_3-10 powder has ~35 % <0.2 μm. The particle size distributions by gravitational sedimentation method are given in the Appendix.

Many fine powders show a good fit to the log normal distribution. The log normal width parameter σ_z is related to the geometric standard deviation σ_g as follows:

$$\sigma_z = \ln(\sigma_g) \qquad (4.1)$$

Figure 4.2 shows plot of particle size distribution plotted on a log-probability scale for Al_2O_3-7, -8, -10, and -27. Al_2O_3-7, -8 and -10 powders fit the log normal distribution reasonably well, while Al_2O_3-27 has a substantial deviation. The geometric standard deviations were estimated graphically from Figure 4.2. The geometric standard deviation of Al_2O_3-7 powder was 1.65, while Al_2O_3-8 decreased to 1.57 after removing large particles and agglomerates from Al_2O_3-7 powder. Al_2O_3-10 powder had a geometric standard deviation of 1.76, indicating that the particle size was broadened by mixing Al_2O_3-8 and -19 powders. Although the median particle diameter of Al_2O_3-27 was very fine (~0.12 μm), the geometric standard deviation (~1.92) shows that the distribution is relatively broad compared to the other powders.

4.1.2 SiC Whisker

Physical characteristics of the SiC whiskers are given in Table 4.2 and Table 4.3. Table 4.2 shows that the aspect

Table 4.2 Characteristics of SiC whiskers

Whisker* type	Average length (μm) #	Average diameter (μm) #	Estimated aspect ratio	Specific surface area (m^2/g)	Pycnometer density (g/cm^3)
TSC-A	7.8	0.37	21.1	3.1	3.19
TSC-B	6.1	0.31	19.7	4.5	3.16
TSC-C	3.6	0.26	13.8	6.3	3.16
TSC-AR	6.3	0.34	18.6	4.1	3.19
TSC-F	5.7	0.34	16.7	4.4	3.21
ASC-AR	7.8	0.39	20.0	3.6	3.18
ASC-F	7.3	0.36	20.3	3.4	3.21

* TSC and ASC represent Tateho and ARCO whiskers, respectively.
\# The average values are obtained on the number basis.

Table 4.3 Calculated surface area and length averaged whisker length

Whisker Designation	Calculated Surface Area (m^2/g)	Length Average Whisker Length (μm)
TSC-A	3.5	14.6
TSC-B	4.1	11.8
TSC-C	5.0	6.6
TSC-AR	3.8	
TSC-F	3.8	12.7
ASC-AR	3.3	15.0
ASC-F	3.5	15.39

ratios are in the range ~14-21. In particular, the aspect ratios of TSC-A, -B, C were 13.8, 19.7, and 21.1, respectively. These three fractions were used to study the effect of aspect ratio on packing and densification behavior of composites. Since the measurements were made with the SEM photographs, the average values of diameter and length were obtained on number basis. The average aspect ratio was calculated based on the number average dimensions.

The calculated average aspect ratio values are relatively lower than those reported in the literature [Tie87; Bul87a]. This can be attributed to the different sample preparation methods for SEM observations. Figure 4.3 shows the scanning electron micrographs for the powder samples prepared using dry and wet sampling techniques. In the case of dry sampling, it is very difficult to measure dimensions of individual whiskers because the whiskers are clustered together. On the other hand, whiskers remain separated when samples are prepared from suspension, as described in Chapter 3. From the number averaged dimensions, the surface area was calculated assuming that whiskers have cylindrical geometry (Table 4.3). The calculated surface area agrees quite well with the measured BET surface area.

Although the calculated average aspect ratio is usually reported in terms of number-based dimensions [Bul87a, Tie87], the packing and densification behavior of composites are predicted, according to percolation theory [Zal83; Cim88] and heterogeneous sintering model [Bor88a; Rah88], to be

(A)

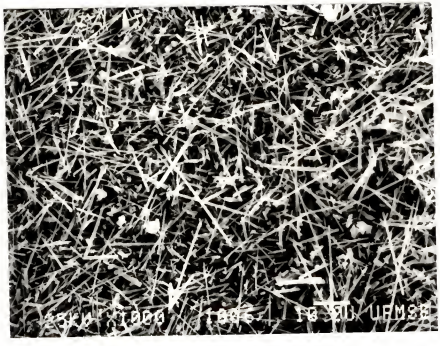

(B)

Figure 4.3 Scanning electron micrographs of the TSC-F whiskers prepared by (A) dry sampling and (B) wet sampling.

dependent on the volume fraction of high aspect ratio whiskers. It is very difficult to measure a volume average size characteristic with microscopic techniques. However, the whisker diameters have a relatively narrow distribution as shown in Figure 4.4. (For example, on a number basis, about 70 % of whisker diameters are in 0.2-0.4 μm range.) Thus, the volume-based distribution of whisker lengths is reasonably equivalent to the length-based distribution.

The length-averaged whisker length are reported in Table 4.3. The length-averaged whisker length was calculated from the microscopic measurements using following equation:

$$\bar{l}_l = \frac{\sum l_i^2 n_i}{\sum l_i n_i} \qquad (4.2)$$

where $\bar{l}_l$ is a length-averaged whisker length, l_i is a whisker length for class i, and n_i is the number of whiskers for class i. Due to the greater contribution of longer whiskers, the length-averaged whisker length values are almost two times larger than those of number-averaged length. Since the majority of studies were carried out with TSC-F whiskers, the number- and length-based distributions are compared in Figure 4.5. The amount of whiskers shorter than 5 μm were ~64 and ~32 % for the number- and length-based distributions, respectively. On the other hand, the amount of whiskers longer than 30 μm were 1.8 % and 12.8 % for the number- and length-based distributions, respectively. When evaluating the size characteristics of whiskers, it is necessary to choose the population quantity which is appropriate for the

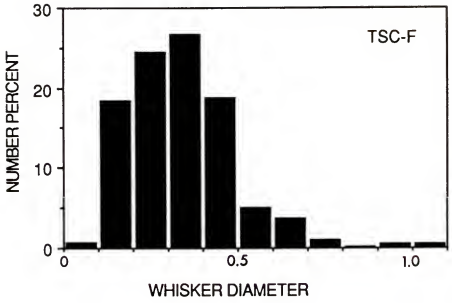

Figure 4.4 Histogram plot of whisker diameter for TSC-F on number basis

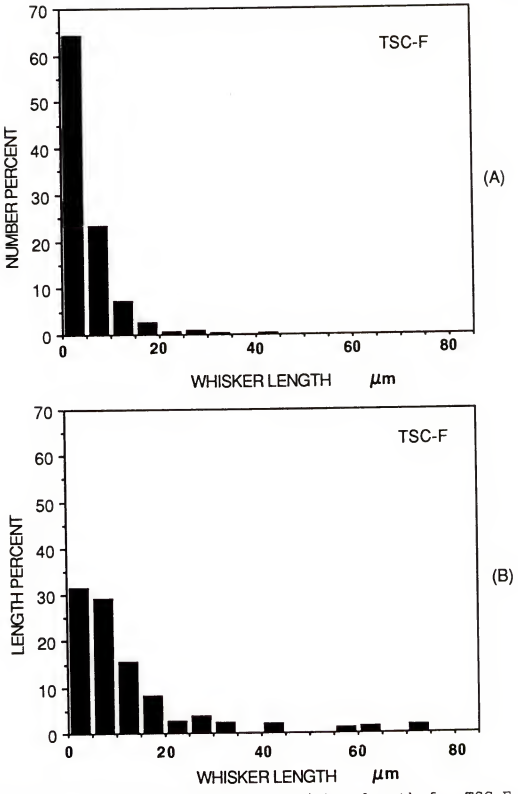

Figure 4.5 Histogram plots of whisker length for TSC-F whisker in (A) number-base and (B) length-base distributions.

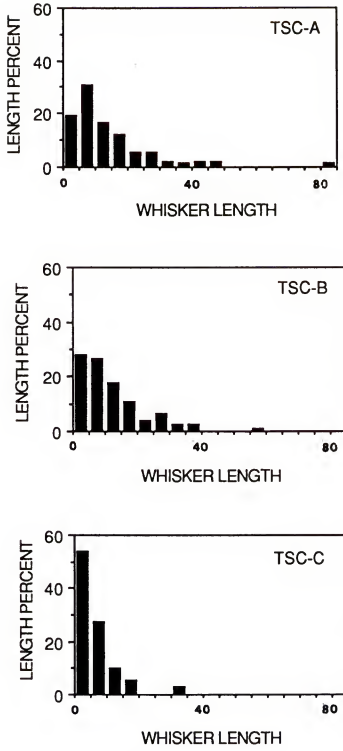

Figure 4.6 Histogram plots of whisker length for (A) TSC-A, (B) TSC-B, and (C) TSC-C on length-base distribution.

Table 4.4 Cation impurities of whisker obtained by ICP.

Element	Base Washing (ppm)	Acid Washing (ppm)
Ca	1.6	14.0
Si	18.6	0.8
Na	2.6	0.0
Mg	0.0	0.2
Al	0.1	0.2
Fe	0.0	0.8
Ni	0.0	0.1

properties.

Figure 4.6 shows the histogram plots of TSC-A, -B, and -C whiskers on length base. As illustrated in Table 4.2 and 4.3, the differences in size characteristics between TSC-A and TSC-B fractions are not significant, but the differences in sizes between TSC-A and TSC-C fractions appear to be large enough to study the effects of whisker aspect ratio on suspension properties, packing and densification behavior. From the length-based distributions (Figure 4.6), the amount of whiskers longer than 20 μm were 20.3 %, 16.3 %, and 2.8 % for TSC-A, -B, and -C, respectively.

Often, the impurity level of the starting powder plays an important role in the subsequent processing steps as well as final properties. The manufacturer's literature reported that major impurities were Ca (0.27 wt%), Al (0.25 %), Mg (0.14%), and Fe (0.03%). The SiC whiskers listed in Table 4.2 have been washed in acid (~0.018 N HNO_3 solution) and base (~0.15 N NH_4OH solution) and the supernatants were analyzed by inductively coupled plasma (ICP) emission spectroscopy. Table 4.4 shows the results of ICP analysis. Calcium was the main impurity washed out in the acid wash, while Si was the major element leached out in the base washing process. Most of these impurities are believed to be leached out of whisker surfaces. These impurities can have profound effects on dispersion of the powder in liquid and sintering by reaction.

4.1.3 Sintering Additives and Infiltrant

The characteristics of MgO and Y_2O_3 powders which were fractionated by gravity sedimentation are shown in Table 4.5. The median sizes (determined by centrifugal photosedimentation) of the MgO and Y_2O_3 were o.24 and 0.32 μm, respectively. The additive powders have sizes fairly comparable to alumina matrix particle sizes. For monosized spheres, the equivalent particle size can be calculated from the BET surface area using the formula $6=d\rho S$, where d is particle diameter (μm), ρ theoretical density (g/cm^3) and S specific surface area (m^2/g). The estimated BET particle sizes of MgO and Y_2O_3 are 0.04 and 0.09 μm. This illustrates that both powders are highly aggregated even after gravity sedimentation classification. Figure 4.7 shows the cumulative particle size distributions for the MgO and Y_2O_3 powders. All the particles (or agglomerates) are smaller than 1 μm. The particle size of Y_2O_3 was slightly finer compared to the results by Akinc and coworkers [Aki86]. The reason is that the gravity sedimentation eliminated most of large particles resulting in finer particle size. In addition, the particle size was further reduced after calcination at 900°C (due to possible shrinkage).

The infiltrant used for increasing green density of composites was $Al(NO_3)_3 \cdot 9H_2O$. The weight loss from thermal gravimetric analysis (TGA) (Figure 4.8) shows that most of thermal decomposition (5 °C/min) was completed below 600°C. After heating to 600°C at 5 °C/min, weight loss was ~83.5 %.

Table 4.5 Characteristics of sintering additives.

Powder	Median Stokes Diameter (μm)	BET Surface Area (m^2/g)	Pycnometer Density (g/cm^3)
MgO	0.24	45.1	3.54
Y_2O_3	0.32	13.0	4.99

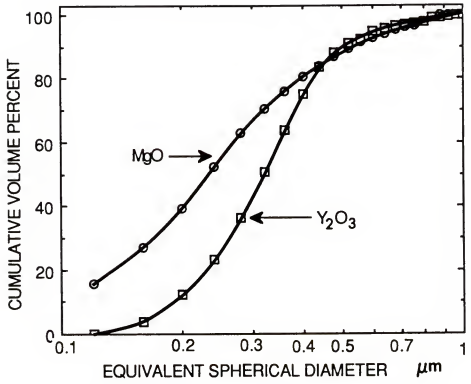

Figure 4.7 Cumulative plots of equivalent spherical diameter for MgO and Y_2O_3.

This is very close to the calculated theoretical value of 82.4 %. Three peaks are observed by differential thermal analysis (DTA). The first endothermic peak (peak A) at ~75°C corresponds to melting of ANN, while the second peak (peak B) at ~170°C corresponds to the decomposition of the hydrate and nitrate. Since the decomposition of the hydrate and nitrate results in a high pressure of reaction product gases (i.e., water vapor and nitrous oxide), it is important to control the decomposition heating schedule in ~100-250°C range in order to avoid the rupture of the samples. The last peak (peak C) can be assigned to the transformation from an amorphous Al_2O_3 to a transition crystalline Al_2O_3. The specific surface area of infiltrant changed from 150 m^2/g at 400°C to 15 m^2/g at 600°C, which indicates that the particle size of the infiltrant increased during heat treatment. Assuming monosized spherical geometry (using 2.6 g/cm^3 as the true density [Bae76]), the particle size after heat treatment at 600°C was calculated to be ~0.15 mm. This is consistent with the reported values by Ciminelli in which the particle sizes were 0.21 and 0.14 mm at 550 and 700°C, respectively [Cim83].

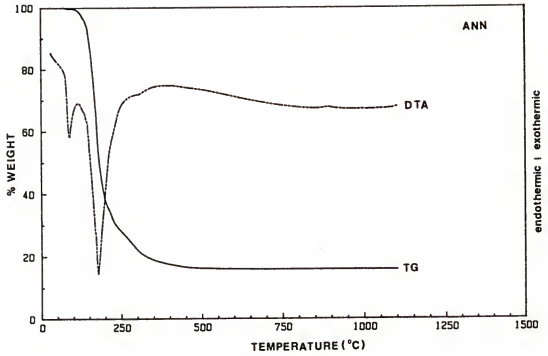

Figure 4.8 Plots of TG and DTA analyses of ANN.

4.2. Suspension Characteristics

4.2.1 Al_2O_3 Suspension

To optimize green microstructural characteristics, it is desirable to utilize well-dispersed suspensions, i.e., suspensions in which interparticle repulsive forces are large. Electrostatic repulsion, in which particles acquire a surface charge and an electrical double layer is created, is a common mechanism for stabilization against flocculation. In many suspensions, pH adjustment can be used to impart a surface charge to particles. This approach was used in the present study, however, since codispersion of Al_2O_3 particles and SiC whiskers was required, it was necessary to identify conditions in which both materials develop a sufficiently large surface charge of the same sign (i.e., both positive or negative). Figure 4.9 shows a plot of zeta potential versus pH obtained using a dilute aqueous suspension (~300 ppm) of alumina-8 powder. It is evident that alumina has quite high zeta potentials at very low and very high values (pH<~2.5 or pH>10.5). However, a somewhat higher pH (~4) was used in processing composite samples (despite the slightly lower zeta potentials) to avoid excessive acid additions. In most processing operations, the zeta potential and the ionic strength are not independently varied. For example, while an acid (or base) may be added to increase zeta potential, the ionic strength is also increased since the acid (or base) is

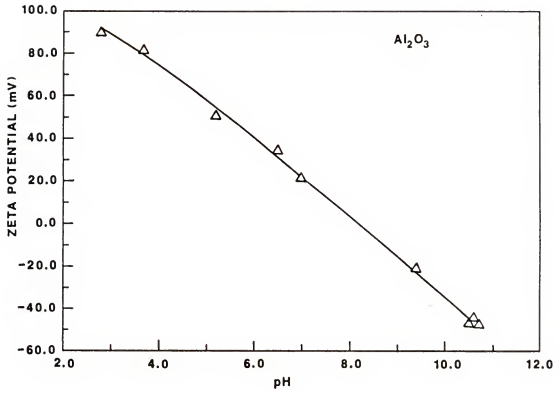

Figure 4.9 Plot of zeta potential as a function of pH for alumina.

an electrolyte which contributes ions to the solution phase. Rojas [Roj88] demonstrated the effect of ionic strength on the suspension properties and green microstructures of alumina and zirconia. In alumina, he found that the suspension viscosity was minimized and the green relative density was maximized at pH~4. He calculated DLVO pair potentials using ionic strength values estimated from the solution conductivities that were measured on supernatant liquids obtained from centrifugation of 40 vol% suspensions. For a pH~4.1 suspension, the calculated energy barrier maximum in the DLVO potential-distance plot was ~130 kT. The energy barrier was zero for suspensions prepared at pH~10.5, despite a moderate zeta potential (~50 mV). This was due to the high ionic strength in these suspensions (i.e., high base concentrations were needed to achieve pH~10.5).

Table 4.6 shows the mercury porosimetry and rheological data for Al_2O_3-7 suspensions (prepared with 50.6 vol% solids) which were aged for 20 hr. Lower viscosity and higher green density, and smaller median pore size were obtained for samples prepared with pH~4 suspensions. In contrast, the pH~10.6 suspension had considerably higher suspension viscosity, much lower green density, and larger median pore channel radius. This is consistent with Rojas' observation [Roj88] on 40 vol% alumina suspensions.

For experiments in which composites were prepared with sintering additives, it was necessary to use a high suspension pH for co-dispersion because one of the components

Table 4.6 Rheological and porosimetry results of suspension.

Dispersion condition			Suspension viscosity (mPa·s)		Porosimetry results	
Disper-sant	Conc. (wt%)	pH	3 s^{-1}	300 s^{-1}	MPR (nm)	% ρ_{th}
no	-	4	280	26	36	68.2
no	-	10.6	26000	413	57	58.6
Tamol 901	1.0	10.6	970	51	45	62.8

* Dispersant was added to suspension based on weight of Al_2O_3.

(i.e., the Y_2O_3) has very high solubility in water at low pH (≤6). To avoid excessive flocculation of the alumina particles at high pH, a polyelectrolyte dispersant (Tamol 901) was used. The Al_2O_3 suspensions prepared with 1.0 wt% Tamol 901 (based on total solid weight) at pH 10.6 showed a relatively low suspension viscosity and improved green relative density compared to the suspension without the dispersant (Table 4.6). To further optimize the dispersion condition, the effect of Tamol 901 polyelectrolyte concentration on the green body characteristics were investigated using suspensions which contained the sintering additive (MgO, Y_2O_3).

Figure 4.10 shows plots of relative density and median pore channel radius vs. concentration of Tamol 901 polyeletrolyte dispersant for suspensions prepared at pH=11.0 with 2 wt% Y_2O_3 and 0.5 wt% MgO, and 45 vol% Al_2O_3. The optimum green body characteristics were obtained with Tamol 901 additions in the range 1.0-1.8 wt%. By comparison with the results in Table 4.6, it is evident that the sintering additives have minimal effect on the green body characteristics.

Although conditions of high zeta potential and low ionic strength produce substantial particle-particle repulsion forces, this does not ensure that the particles in a stable suspension are primary particles, i.e., instead of

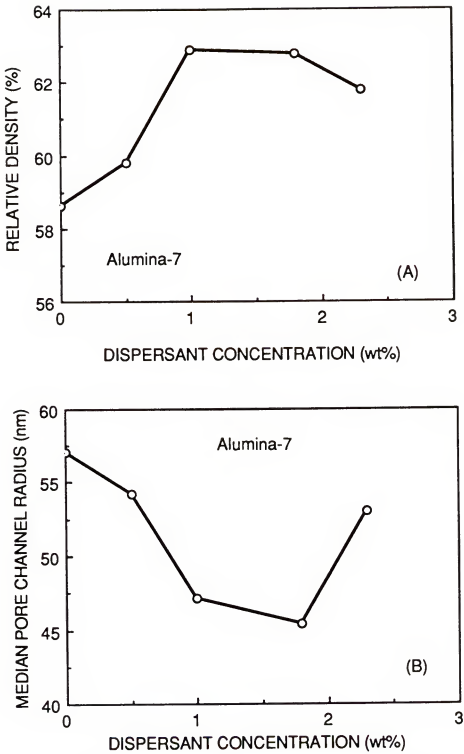

Figure 4.10 Plots of relative density and median pore channel radius as a function of the concentration of Tamol 901 at pH=11.

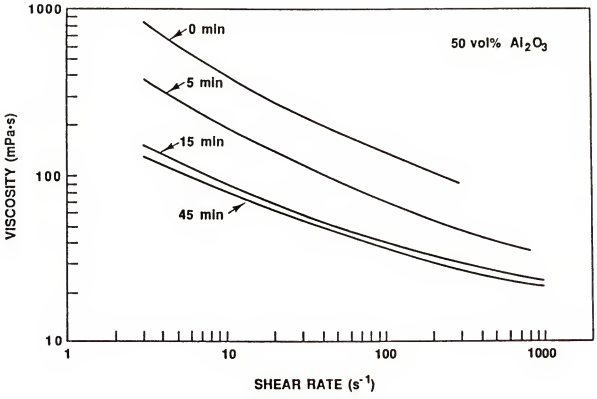

Figure 4.11 Plots of suspension viscosity vs. ultrasonication time for 50 vol% solid (alumina-7) loadings at pH=4.

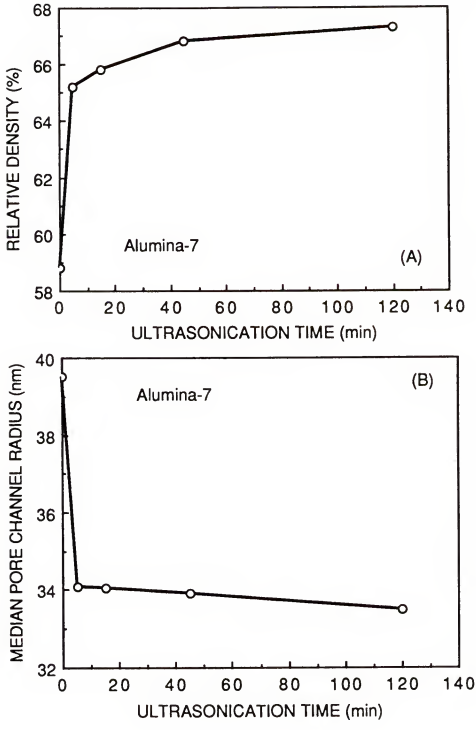

Figure 4.12 Plots of (A) green relative density and (B) median pore channel radius as a function of ultrasonication time.

agglomerates. In the suspension preparation stage, mechanical energy may be required to break down agglomerates which exist in the starting powder due to adsorbed moisture, van der Waals forces, etc. Soft agglomerates can be effectively broken down by ultrasonication treatment. Figure 4.11 shows plots of viscosity vs. shear rate for the alumina (Al_2O_3-7) suspensions prepared at pH=4 and sonicated for various times. Most of soft agglomerates were broken down after ~15 minute ultrasonication treatment, as indicated by the large decrease in viscosities. Aoki and coworkers [Aok87] also observed that the suspension viscosity decreases more slowly after reaching the state where almost all particles exist as primary particles. Improved dispersion with sonication was also confirmed from porosity characteristics of samples slip-cast from the suspensions in Figure 4.11. Figure 4.12 shows plots of relative green density and mean pore channel radius as a function of suspension sonication time. A dramatic increase in relative density and decrease in median pore radius were observed after only 5 min sonication.

4.2.2 SiC Whisker Dispersion

Figure 4.13 shows the plot of zeta potential of TSC-C whisker vs pH using dilute suspensions (~300 ppm). It is obvious that the zeta potential values are relatively high at both low and high pH values. Since the codispersion of Al_2O_3 and SiC whisker are desired, the dispersion behavior of the SiC whiskers was studied at low (~4) and high pH (~10.5) values. Table 4.7 shows the sediment density values

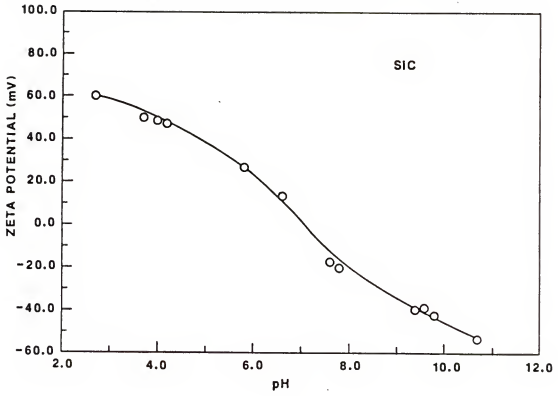

Figure 4.13 Plot of zeta potential of SiC whisker (TSC-C) as a function of pH.

Table 4.7 Sediment density for SiC whisker suspensions

Whisker Type*	Dispersant	Dispersant Conc. (wt%)	pH	Sediment Density (g/cm^3)
TSC-AR	-	-	4.0	0.72
TSC-AR	-	-	10.4	0.72
TSC-AR	Daxad	0.5	4.0	0.90
ASC-AR	-	-	10.6	0.97
ASC-AR	Tamol 901	0.5	10.5	0.97
ASC-AR	Daxad	0.5	4.0	0.73

* The whiskers were washed in dilute acid and base solutions.

obtained for several dispersion conditions. The sediment density values were in the range 0.72-0.97 g/cm3 (22.4-30.2 % relative density), which is similar to or higher than the density value obtained by mechanical packing of fibers of similar aspect ratio (~20) [Mil86]. The sediment densities in Table 4.7 are slightly higher than that obtained by Takao et al. in a study of pressure filtration of SiC whiskers [Tak87]. Relative density values obtained in the latter study were only ~20 %. (However, comparisons with other studies must be made cautiously due to differences in the manner that SiC whisker aspect ratios are measured.)

In addition to sedimentation experiments, the rheological behavior was studied for suspensions prepared with washed and as-received (unwashed) TSC whiskers which contained 0.5 wt% polyelectrolyte dispersant. Figure 4.14 shows plots of suspension viscosity vs shear rate for the above suspensions. Not surprisingly, increasing the solids loading from 3 to 8 vol% increases the suspension viscosity. However, the suspension prepared with washed whiskers showed significantly lower viscosity at the higher loading.

Rheological behavior of whisker suspensions depends on volume fraction of whiskers, aspect ratio, and shear rate [Zie70]. The viscosity of whisker suspensions can be ascribed to two major contributions of whisker movements in the flowing liquid: rotation of high aspect ratio whiskers and formation of network structures [Zie70]. These structural

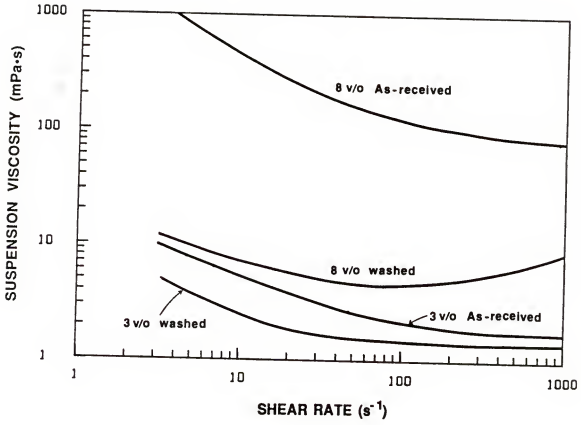

Figure 4.14 Plots of suspension viscosity vs. shear rate for suspensions prepared with washed and as-received whiskers with 3 and 8 vol% solids loading.

contributions are much larger in whisker suspensions compared to spherical particle suspensions. Whiskers can produce greater perturbations during rotation at low solid volume fraction, and, therefore, enhanced energy dissipation and higher viscosities may be obtained. Whisker-whisker interactions and development of network structures occurs at lower solids loading.

Figure 4.14 shows that 3 vol% suspension prepared with washed whiskers have slightly lower viscosities and slightly less shear-thinning behavior compared to suspensions prepared with 3 vol% unwashed whiskers. At higher whisker content, the difference in viscosity was more pronounced, i.e., the viscosity of the 8 vol% washed whisker suspension was nearly 2 orders of magnitude lower than that of the 8 vol% unwashed whisker suspension at low shear rate (3 s^{-1}). The latter suspension showed much more shear-thinning behavior which is indicative of flocculation. Interestingly, the well-dispersed suspension with 8 vol% washed whiskers showed a slightly shear-thickening behavior at high shear rates. This is presumably due to the interlocking between whiskers at high shear rate since high-aspect-ratio whiskers are likely to have more whisker-whisker interactions at lower solids loading.

In order to optimize the concentration of dispersant (Daxad), the rheological behavior of suspensions prepared with 8 vol% washed TSC whiskers was investigated. As shown in Figure 4.15, the suspension with 0.5 wt% Daxad (based on SiC

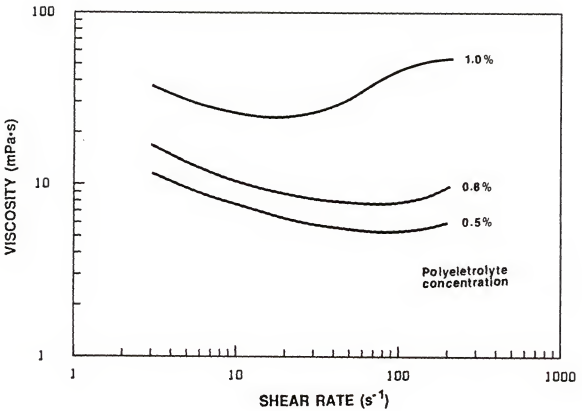

Figure 4.15 Plots of suspension viscosity vs. shear rate for the suspensions prepared with various dispersant concentrations.

whisker weight) showed the lowest viscosity, indicating that suspension stability against flocculation was maximized.

In an effort to identify the dispersion mechanism, the amount of dispersant adsorbed on whiskers and electrophoretic mobility of whiskers with adsorbed dispersant were measured at pH=4. The zeta potential for suspension with dispersant slightly increased from 49 to 65 mV. The amount of dispersant adsorbed on the whisker surface was ~0.11 mg/m^2. It is believed that the Daxad polyelectrolyte provides additional electrostatic stability against flocculation via increased repulsion between whiskers (i.e., due to the increased zeta potential). Although steric stabilization may also contribute to the improved stability, this mechanism seems less likely due to the relatively low amount of adsorbed polymer.

Another consideration in achieving good dispersion of the SiC whiskers is the wetting behavior. The wetting characteristics of a liquid on a solid surface (e.g., ceramic particles) depends upon three specific interfacial energies: solid-vapor (γ_{SV}), liquid-vapor (γ_{LV}), and solid-liquid (γ_{SL}). In the absence of chemical reactions between the solid and liquid, the contact angle, q, for the liquid on the solid surface is given by the Young-Dupre equation:

$$\cos\theta = \frac{\gamma_{SV} - \gamma_{SL}}{\gamma_{LV}} \qquad (4.3)$$

Thus, good wetting is promoted by high γ_{SV}, low γ_{LV}, and low γ_{SL}. The first two conditions are readily satisfied in ceramic particle/water suspensions. The third (low γ_{SL}) is also

satisfied in many aqueous suspensions of oxide powders because the particle surfaces are well-covered with hydroxyl groups. However, in non-oxide powders (e.g., SiC whiskers), surface hydroxylation is often more limited and difficulties in wetting may arise. It was observed that it took a longer ultrasonication treatment to achieve a comparable viscosity value for suspension without dispersant. Dispersion was achieved in about 5 minutes for the 5 vol% whisker suspensions with dispersant, while it took longer than 15 minutes to achieve similar viscosity with the suspension without dispersant. This could be related to the kinetics of liquid penetration into porous whisker clusters since $d^2 \propto \cos\theta$ (eq (2.63)).

4.2.3 Characteristics of Composite Suspensions

By using the combination of pH adjustment and polyelectrolyte addition (Daxad or Tamol), Al_2O_3 particles and SiC whiskers could be codispersed at high overall solids concentration while maintaining relatively low suspension viscosities desired for casting operations.

Figure 4.16 shows plots of suspension viscosity vs shear rate for suspensions containing 50 vol% total solids concentration and varying Al_2O_3 (alumina-8)/SiC (TSC-C) volume ratios. The rheological flow behavior for suspensions with low whisker concentration (5 vol%) is approximately the same as for 100 vol% Al_2O_3 suspensions. However, the suspension viscosity increases at higher SiC whisker contents (15, 30

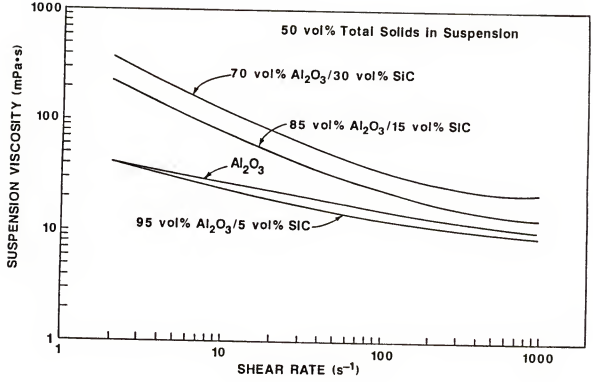

Figure 4.16 Plots of viscosity vs. shear rate for suspensions containing 50 vol% solids and varying Al_2O_3(alumina-8)/SiC whisker(TSC-C) volume ratios.

vol% whisker concentrations). This behavior indicates that the high aspect ratio SiC whiskers tend to form network structures at high concentrations. This tendency is indicated by the observation that suspensions with SiC whiskers alone are difficult to prepare beyond ~15 vol% solids concentration with the smallest aspect ratio whiskers, even under the optimum dispersion condition.

Suspensions with higher aspect ratio whiskers (i.e., TSC-A) have higher viscosities than those with lower aspect ratio whiskers (i.e., TSC-C). Figure 4.17 shows the plots of viscosity vs. shear rate for the 50 vol% suspensions prepared with TSC-A (L/D~21) and TSC-C (L/D~14) whiskers. The alumina used in these suspensions was alumina-8 powder. Again, the suspension viscosity increases with increasing whisker concentrations. At 30 vol% whisker concentration, the suspension prepared with TSC-A whiskers has a significantly higher viscosity than with TSC-C whiskers. At ~10 s^{-1}, the viscosity values are different by one order of magnitude. This illustrates that more whisker-whisker interactions develop with higher aspect ratio. This is consistent with the prediction by Ziegel [Zie70].

The effect of whisker aspect ratio on suspension viscosity was quantitatively analyzed by a number of investigators [Zie70, Kit81]. Ziegel developed a theoretical equation for the shear dependence of the viscosity of fiber suspensions as follows:

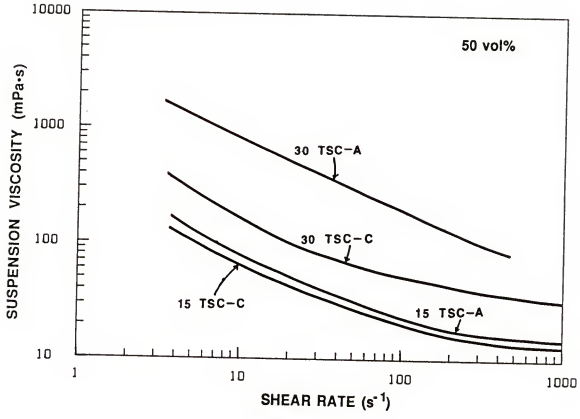

Figure 4.17 Plots of viscosity vs. shear rate for 50 vol% composite suspensions with TSC-A(L/D~21) and TSC-C(L/D~14) whiskers.

$$\eta_r = \left\{ \frac{3Z\mu\beta}{\dot{\gamma}} + 1 - Z \right\} \frac{a_r^{5/3}\,\phi}{9.668} \qquad (4.3)$$

where η_r is relative density of suspension, μ is an interaction parameter, β is a rate constant for the equilibrium between free particles and agglomerates, Z is the degree of agglomeration, a_r is the aspect ratio, and ϕ is the solids concentration. Equation (4.3) also shows a 5/3 power dependence on the aspect ratio. Kitano and Kataoka [Kit81] found in their rheological study on polymer fibers in polymer liquids that $\mu\beta$ product and Z are also dependent upon the volume fraction of fibers and aspect ratio.

Figure 4.18 shows plots of suspension viscosity vs. shear rate for 45 vol% suspensions containing SiC whisker (TSC-F)/Al_2O_3 (alumina-10) with various ratios. The viscosities in Figure 4.18 for the suspension prepared with alumina alone are slightly higher than values obtained in Figure 4.16 despite lower solids loading (i.e., 45 vs 50 vol%). This can be attributed to the fact that Al_2O_3-10 powder has a larger portion of very fine particles. As shown in Figure 4.1, ~34 vol% of the particles of the alumina-10 powder are $\leq$0.2 μm, while only ~15 vol% of the particles of alumina-8 powder are $\leq$0.2 μm. Previous studies have shown that suspensions prepared with finer particles (in the submicrometer range) tend to have higher viscosities, particularly at lower shear rate [Bro65, Kri72, Con60, Yeh88, Yeh89]. This is due to the increased importance of Brownian motion and electroviscous phenomena in suspensions with

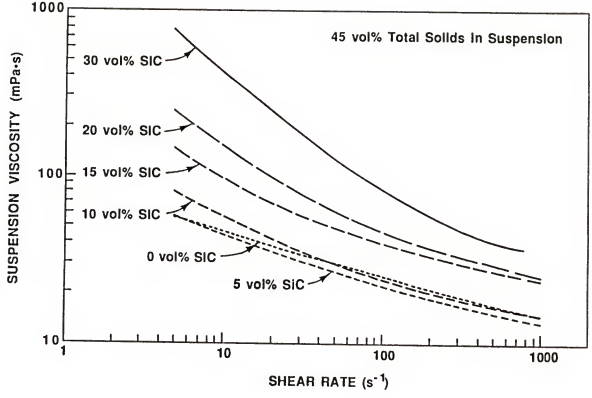

Figure 4.18 Plots of viscosity vs. shear rate for TSC-F SiC whisker/alumina-10 suspensions containing 45 vol% total solids and varying concentrations of SiC whiskers.

ultrafine particles. Krieger [Kri72] showed with dialyzed polystyrene suspensions that the suspension viscosity increased drastically at low shear rates as the particle size decreased from ~0.38 to ~0.16 μm. The increase of viscosity was attributed to the formation, by Brownian motion, of temporary doublets which are destroyed by the strong shear field at high shear rates. The secondary electroviscous effect is attributed to the overlap of double layers on two approaching particles. Since the frequency of such interactions is proportional to ϕ^2, it is introduced as a correction to k_2 in the following equation:

$$\eta_r = 1 + k_1\phi + k_2\phi^2 + \ldots \qquad (4.4)$$

where k_1 is the Einstein coefficient, and k_2 is the interaction coefficient. Russel suggested that k_2 is very sensitive to κ since k_2 is dependent upon $(\kappa r)^{-5}$. The secondary electroviscous effect becomes increasingly important as zeta potential increases, the ionic strength increases, and the particle size decreases.

As observed in Figure 4.16 and 4.17, the rheological flow behavior for suspensions in Figure 4.18 also depends on both whisker concentration and whisker aspect ratio. The suspension viscosities increased more rapidly with increasing whisker concentrations compared with the results obtained for TSC-C whisker/Al_2O_3-8 suspensions. This can be attributed to both the alumina particle size and whisker aspect ratio, as discussed earlier. The aspect ratio of TSC-F is slightly higher than that of TSC-C (17 vs. 14). Since the viscosity of

fiber suspension shows a 5/3 power dependence on the aspect ratio [Zie70], it is expected that the suspensions with whiskers with higher aspect ratio (L/D=17) has higher viscosities.

4.3 Green Body Characteristics

4.3.1 Consolidation Conditions

While well-dispersed suspensions are important in obtaining desirable green microstructures, segregation of particles (e.g., due to differences in particle size, shape, and/or density), during consolidation must also be prevented to avoid inhomogeneities and reduced relative density. In suspensions prepared with a single powder, differences in settling rate during consolidation arise because of differences in particle size. In codispersed suspensions, such as in the present study, differences in the true density of constituent phases will also result in the differences in settling rate. Hence, particles with larger sizes (e.g., whiskers) and/or higher densities tend to accumulate toward the bottom of cast samples, whereas particles with lower densities and/or smaller sizes tend to concentrate near the top of cast samples. This behavior results in less homogeneous samples with broader pore channel size distributions and higher overall pore volumes [Sac85]. The latter effects can be attributed to less-efficient packing of particles, e.g., fine particles are less likely to be located

within the interstices formed by larger particles if segregation occurs.

A variety of methods can be used to minimize segregation of components during consolidation. (1) Suspensions can be consolidated at higher rates, thereby minimizing the time available for segregation to occur. (2) Suspensions can be prepared with higher solids loadings in order to promote hindered settling of particles. (3) The solution viscosity can be increased with additions of soluble polymers in order to decrease the settling rates of the particles in the liquid. (4) Suspension conditions can be chosen to induce heteroflocculation, e.g., segregation is prevented through the formation of flocs with an intimate mixing of the various components. However, the latter approach also has the disadvantage associated with consolidation of flocculated suspensions, i.e., lower green densities and larger pore sizes. The first two approaches are illustrated in the present study.

Suspensions with a 90/10 vol% Al_2O_3 (alumina-7)/SiC(ASC-AR) were prepared using two overall solids concentrations (18 and 54 vol%). Relatively fast consolidation was accomplished by slip casting, whereas relatively slow consolidation was carried out using low-speed (<800 rpm) centrifugal casting. Figure 4.19 shows the pore channel size distributions obtained for cast samples. Figure 4.19 (A) directly compares the effect of the casting methods using suspensions with relatively low (18 vol%) solids loading. The larger median

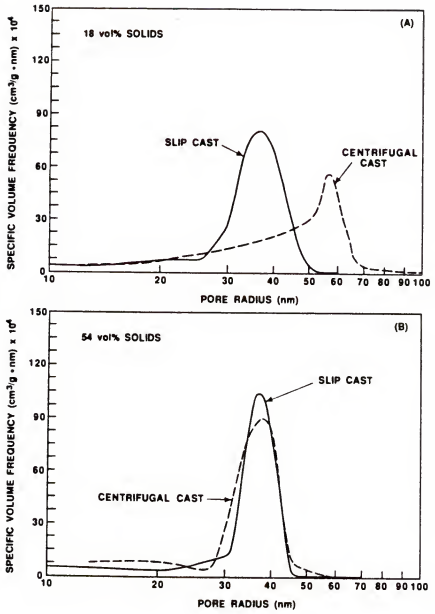

Figure 4.19 Plots of specific pore volume frequency vs. pore channel radius obtained by mercury porosimetry for (A) slip-cast and low-speed centrifugally cast samples prepared using suspensions with 18 vol% solids, (B) slip-cast and low-speed centrifugally cast samples prepared using suspensions with 54 vol% solids.

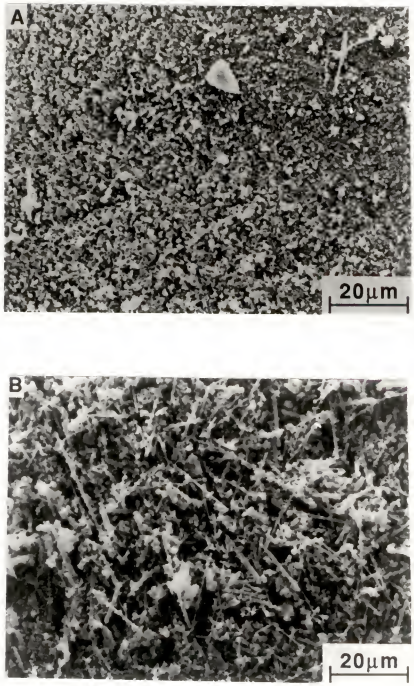

Figure 4.20 Scanning electron micrographs showing (A) depletion of SiC whiskers (ASC-F) near the top surface and (B) accumulation of SiC whiskers near the bottom surface of a low-speed centrifugally cast sample prepared using a suspension with 18 vol% solids.

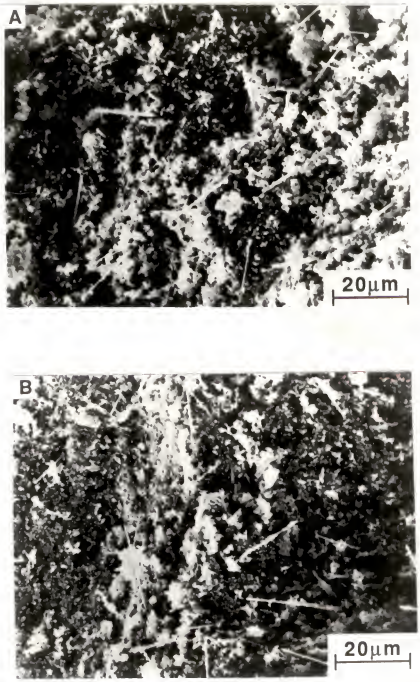

Figure 4.21 Scanning electron micrographs showing a uniform distribution of SiC whiskers (ASC-F) in a slip-cast composite sample prepared using a suspension with 54 vol% solids: (A) region near the top surface and (B) region near the bottom surface of the sample.

pore channel radius and broader pore size distribution for the low-speed centrifugally cast sample indicate that more segregation of the smaller Al_2O_3 particles and larger SiC whiskers occurs with the slower consolidation condition. The total porosity for the centrifugally cast sample, ~35%, is also higher compared to the value of ~32% for the slip-cast sample. Segregation effects for the centrifugally cast sample were also revealed by scanning electron microscopy (SEM) of a sample cross section. Very few whiskers were observed near the top surface of the cast sample (Fig. 4.20(A)), whereas a large accumulation of whiskers was evident near the bottom surface (Fig. 4.20(B)).

In contrast to these results, no significant differences were observed between slip-cast and centrifugally cast samples formed using suspensions with 54 vol% solids. Figure 4.19 (B) illustrates that pore channel size distributions were essentially the same for the two samples. The total porosity was also the same at ~32%. SEM observations (Fig. 4.21) also indicate that the SiC whiskers are homogeneously distributed throughout the matrix for the samples prepared using suspensions with high solids loading.

In summary, homogeneous green microstructures with high green density and small pore size were achieved by slip casting well-dispersed suspensions with high solids loading.

4.3.2. Dry Processing vs. Suspension Processing

Some samples were fabricated by uniaxially dry pressing

composite powders at 103 MPa. A direct comparison of dry processing and suspension processing was made using composite samples prepared with 85 vol% Al_2O_3 (alumina-8)/15 vol% SiC (TSC-B) and 70 vol% Al_2O_3 (alumina-8)/30 vol% SiC (TSC-B) ratios. Figure 4.22 shows the green relative densities for both dry-pressed and suspension-processed Al_2O_3 (alumina-8)/SiC (TSC-B) compacts prepared with several whisker concentrations. As expected, dry-pressed samples have considerably lower green densities. Furthermore, green densities of dry-pressed samples decreased significantly with increasing whisker content, while those of suspension-processed samples have little dependence on whisker concentration.

The advantage of suspension processing over dry processing in achieving high green density is also evident by comparison with results reported by Tiegs and Becher [Tie87]. They consolidated Al_2O_3 powder/SiC whisker mixtures by isostatic compaction at relatively high pressures (280-420 MPa). For mixtures containing less than 10 vol% whiskers, green densities were only in the range 48% to 60%. At higher whisker contents (20 vol%), green densities remained <50%.

As a result of the low density of dry-pressed samples (Figure 4.22), the median pore channel radii are substantially larger compared to suspension-processed samples (35 vs. 59 nm at 15 vol% whiskers and 41 vs. 72 nm at 30 vol% whiskers). Figure 4.23 shows that pore size distributions for

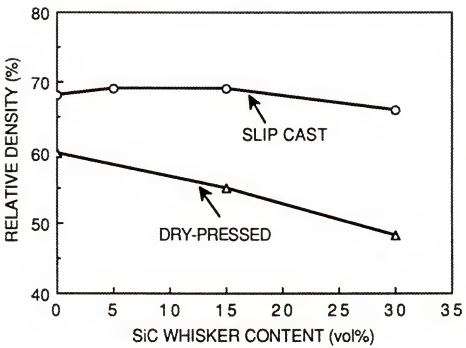

Figure 4.22 Plots of green relative density vs. SiC whisker content for Al_2O_3 (alumina-8)/SiC whisker (TSC-B) samples prepared by slip casting and dry pressing.

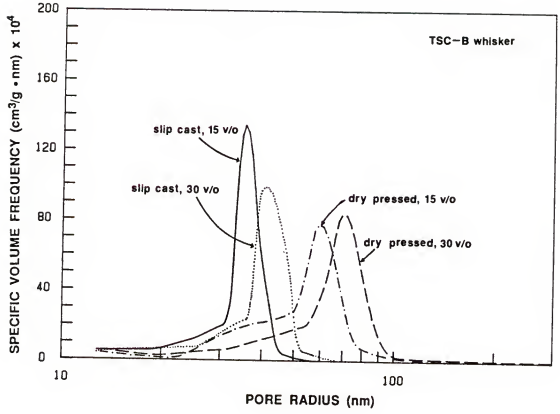

Figure 4.23 Plots of specific pore volume frequency vs. pore channel radius obtained by mercury porosimetry for Al_2O_3 (alumina-8)/SiC whisker (TSC-B) samples prepared by slip casting and dry pressing.

the dry-pressed samples have much broader distributions compared to suspension-processed samples.

Packing behavior of these composite samples can be evaluated more effectively by comparing packing efficiency. Since the calculation of packing efficiency uses the relative densities of both matrix and whisker as references, it is possible to evaluate the adverse effect of whiskers on composite packing. In order to determine the minimum density of dry-pressed samples, the green relative density of SiC whiskers was estimated as 18.7% based on tap density. The rest of the necessary data was obtained from the results shown in Figure 4.22. Table 4.8 shows the results that were obtained using equations (2.40-42) for samples prepared with dry-pressing and slip casting. The packing efficiency of dry pressing is significantly lower than that of suspension processing. The packing efficiencies of dry-pressed samples were only ~6-16% of slip-cast samples and the efficiency decreases with increasing whisker concentrations. This indicates that whiskers form more whisker clusters and rigid network structures at lower whisker content in the dry pressing process. By using the packing efficiency, the degree of whisker percolation effect can be compared. Based on the packing densities of the individual constituents (Table 4.8), the calculated maximum critical whisker concentrations for maximum packing density of composites were 27.7 and 31.6% for dry pressing and slip casting, respectively. From the packing efficiency, it is likely that dry pressing has much higher

Table 4.8 Packing efficiency and maximum achievable whisker concentrations based on bimodal packing theory [Mil78, Mil86]

	Dry pressing*		Slip casting**	
	15 vol% whisker	30 vol% whisker	15 vol% whisker	30 vol% whisker
Minimum density	53.8	47.6	61.8	54.9
Maximum density	63.8	47.6	71.6	75.4
Experimental density	55.0	48.3	69.1	66.1
Packing efficiency	0.12	(0.03)	0.75	0.55

* The packing densities used for calculation of the packing efficiency were 18.9% for SiC whisker compact and 60% for alumina compact for the dry-pressed composites.

** The packing densities used for calculation were 24% for SiC whisker compact and 68.2% for alumina compact for the slip-cast composites.

possibility to form local clusters (i.e., clusters smaller than percolation clusters).

4.3.3 Effect of Whisker Aspect Ratio

Figure 4.24 shows relative green densities for samples prepared with TSC whisker fractions A, B, C and with various Al_2O_3 (alumina-8)/SiC ratios. The key observation is that relative density values are quite high - in the range of 66% to 69% - even with 30 vol% SiC whiskers. In fact, whisker size and concentration have relatively little effect on the green density. The high packing efficiency of the particles and whiskers is also illustrated by comparing the pore size distribution for the composite sample with highest porosity (i.e., 70 vol% Al_2O_3/30 vol% TSC-B) to the distributions for the single-phase (Al_2O_3 and SiC) compacts (Figure 4.25). The pore size distribution for the composite sample is much more similar to the high density Al_2O_3 compact than to the low density SiC compact, illustrating that fine alumina particles effectively fill the interstices formed by large SiC whiskers.

Figure 4.26 shows that the pore size distribution shifts to slightly larger sizes as the SiC (TSC-C fraction) content in the composite samples increases. However, even at 30 vol% SiC, most pore radii are <50 nm. Similar behavior was observed for the composites prepared with TAT-A and -B whiskers.

It is interesting to note that the green densities obtained in this study are higher than values reported for 85

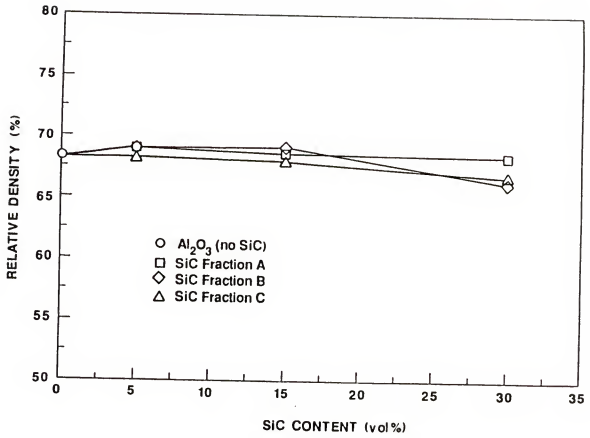

Figure 4.24 Plots of relative green density vs. vol% TSC whiskers for slip-cast samples prepared with different SiC whisker size fractions.

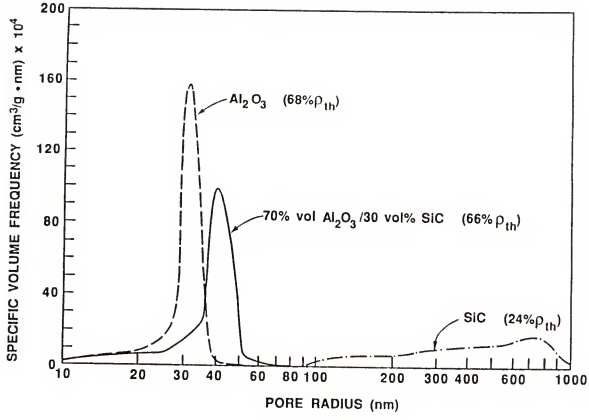

Figure 4.25 Plots of specific pore volume frequency vs. pore channel radius obtained by mercury porosimetry for Al_2O_3, SiC whisker, 70 vol% Al_2O_3 (alumina-8)/30 vol% SiC whisker (TSC-B) compacts prepared by slip casting.

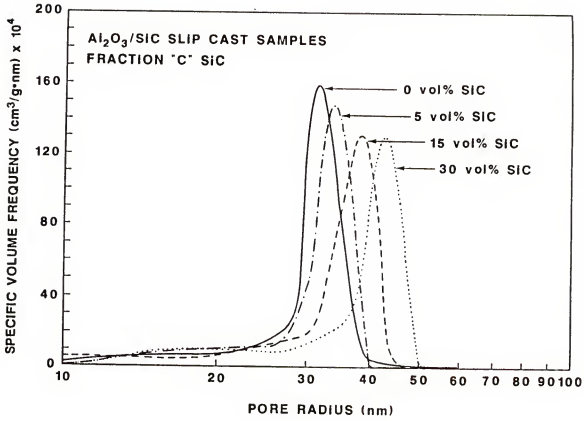

Figure 4.26 Plots of specific pore volume frequency vs. pore channel radius obtained by mercury porosimetry for slip-cast compacts containing various ratios of Al_2O_3 (alumina-8)/SiC whiskers (TSC-C).

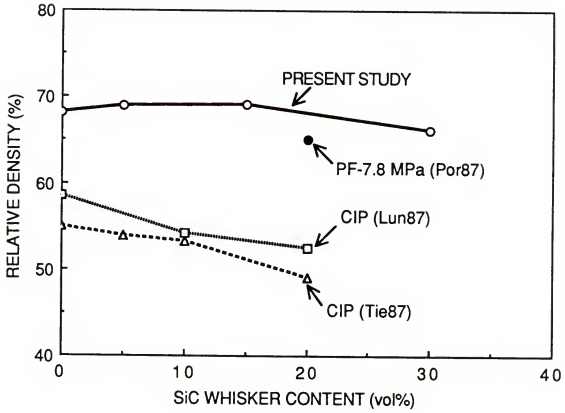

Figure 4.27 Plot of green relative density vs. SiC whisker content for SiC whisker containing composites. Comparisons are made with composites prepared with pressure filtration [Por87] and CIP [Lun87, Tie87].

wt% Al_2O_3/15 wt% SiC whisker suspensions consolidated by pressure filtration (Figure 4.27). Porter et al. obtained green densities in the range of 59% to 65% by varying the consolidation pressure (0.78 and 7.8 MPa) and the suspension pH (2 and 5), which suggests that the Al_2O_3/SiC whisker suspensions prepared in the present study were better dispersed. The green relative densities obtained by cold isostatic pressing are much lower and have strong dependence on whisker concentration, differently from the slip cast compacts in the present study. However, the differences in green density could also reflect differences in the particle and whisker physical characteristics (e.g., whisker aspect ratio, particle and whisker size distributions, etc.).

4.3.4 Effect of Matrix Particle Size

Figure 4.28 shows the relative density of slip cast compacts prepared with the Al_2O_3-10 and Al_2O_3-27 powders and with varying Al_2O_3/SiC whisker (TSC-F) ratios. Samples prepared with both alumina powders produced relative densities in the range of 69-71% for SiC whisker concentrations of 0-30 vol%. In addition, the packing density is independent of matrix particle size and whisker concentration for slip cast samples. Since both powders have similarly high geometric standard deviations, it is expected that the packing behavior (or packing structure) might be similar under the similar consolidation conditions (e.g., interparticle repulsive force, solids loading, casting method, etc.). The packing densities were slightly higher in

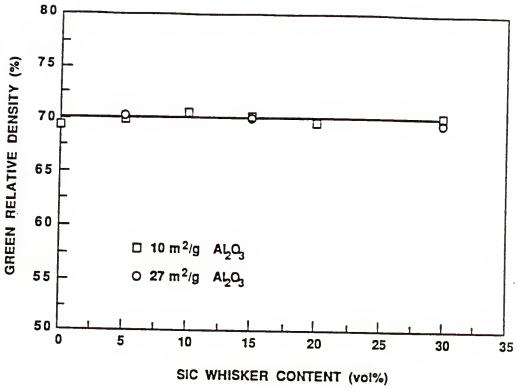

Figure 4.28 Plots of relative green density vs. SiC whisker content for samples prepared with alumina-10 and alumina-27 powders.

comparison to the samples shown in Figure 4.24 (i.e., ~66-69%). This can be attributed to broader particle size distributions for the Al_2O_3 powders used in Figure 4.28 [Mil78, Yeh89].

Figure 4.29 compares the median pore channel radii vs. SiC whisker content for green compacts prepared with alumina-10 and alumina-27 powders. Despite the presence of SiC whiskers, the median pore channel radii increased only slightly with increasing whisker concentration regardless of the matrix particle size. The difference in pore channel sizes for the two series of compacts is attributed to the difference in the alumina particle sizes. This was confirmed in that the median pore channel radius ratios are nearly same as the ratio of median Stokes diameter for the two alumina powders. The median pore channel radius ratio ranged from ~2.2 for pure Al_2O_3 to ~1.8 for 30 vol% whisker composite, whereas the median Stokes diameter ratio was ~2.2.

Figures 4.30 and 4.31 show the pore size distributions for the samples prepared with Al_2O_3-10 and Al_2O_3-27, respectively. Figure 4.30 indicates that pore size distribution shifted to slightly larger sizes as SiC whisker (TSC-F) content increases. However, most pore radii were <35 nm, signifying that particle/whisker packing in the compacts was very homogeneous.

Figure 4.31 shows the pore size distributions for the samples prepared with Al_2O_3-27 powder. In addition to the decrease in median pore channel radii, reducing matrix

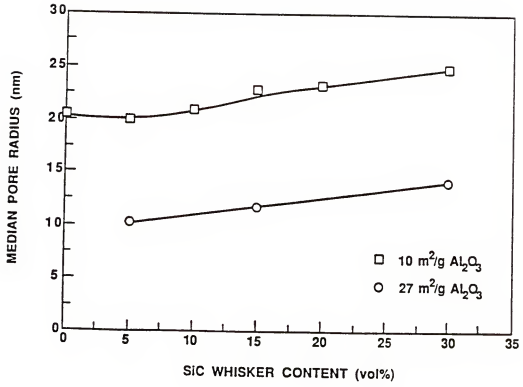

Figure 4.29 Plots of median pore channel radius vs. SiC whisker content for samples prepared with alumina-10 and alumina-27 powders.

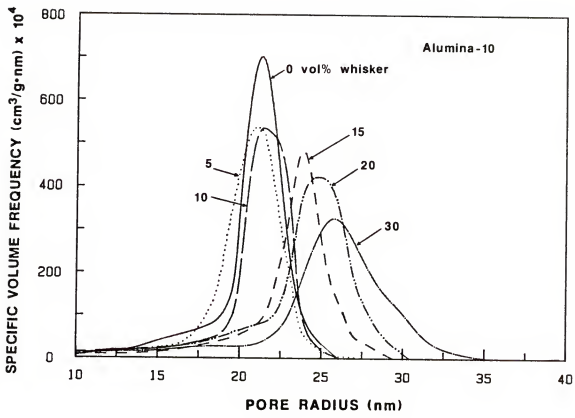

Figure 4.30 Plots of specific pore volume frequency vs. pore channel radius obtained by mercury porosimetry for the samples prepared with alumina-10.

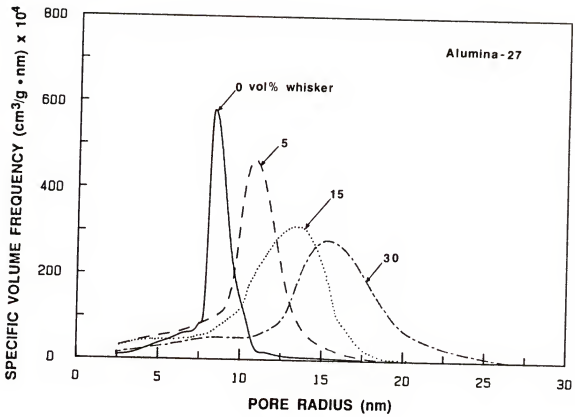

Figure 4.31 Plots of specific pore volume frequency vs. pore channel radius for the samples prepared with alumina-27.

(A)

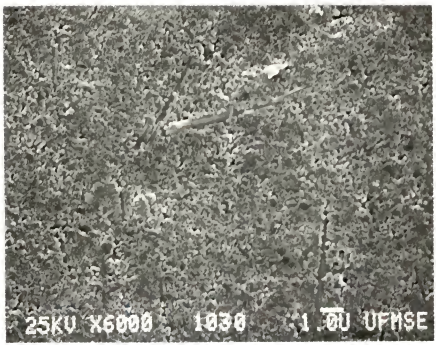

(B)

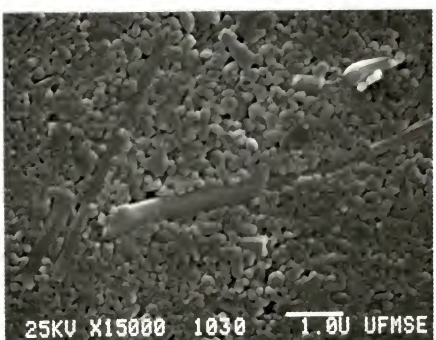

Figure 4.32 Scanning electron micrographs of the top surface of 70 vol% Al_2O_3 (alumina-10)/30 vol% SiC whisker (TSC-F) green compact: (A) low magnification and (B) high magnification.

(A)

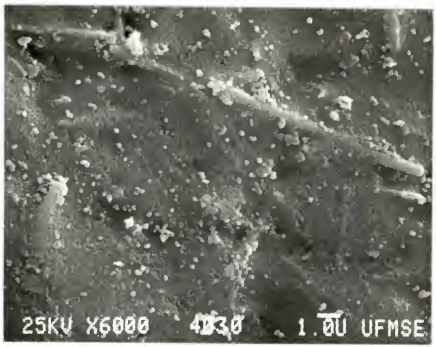

(B)

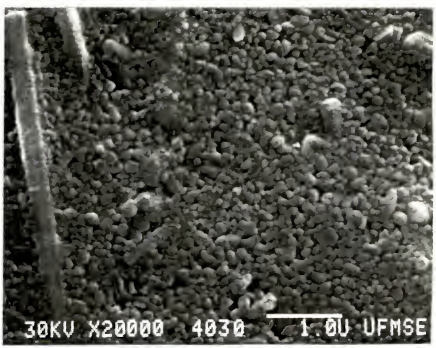

Figure 4.33 Scanning electron micrographs of the top surface of 70 vol% Al_2O_3 (alumina-27)/30 vol% SiC whisker (TSC-F) green compact: (A) low magnification and (B) high magnification.

particle size resulted in the decrease in the largest pore sizes. The largest pore sizes of composites prepared with Al_2O_3-27 powder were ~10 nm smaller than those in composites prepared with Al_2O_3-10 powder. Almost all the pore radii are < ~25 nm.

The homogeneous green microstructures were also confirmed by scanning electron microscopy (SEM) observation. Figures 4.32 and 4.33 show the top surfaces of green compacts containing 30 vol% whiskers with Al_2O_3-10 and Al_2O_3-27 powders, respectively. The SEM micrographs clearly show that whiskers are homogeneously distributed throughout alumina matrix, and that the whiskers and Al_2O_3 particles are densely packed.

4.3.5 Effect of Sintering Additives

This section describes the characteristics of green compacts prepared with sintering aids (e.g., 0.5 wt% MgO and 2.0 wt% Y_2O_3) which were processed at pH=11 with a polyelectrolyte dispersant addition (1.8 wt% Tamol 901).

Figure 4.34(A) shows plots of green density vs. SiC whisker concentration for Al_2O_3-10/TSC-F whisker compacts prepared with and without sintering additives. All of the samples with sintering additives have relatively high green densities (65-66%). The lower green relative densities compared to samples without sintering additives is attributed to slightly less favorable suspension dispersion conditions. As shown in Table 4.6, Al_2O_3 suspensions prepared at pH~11 with polyelectrolyte dispersant (Tamol 901) had significantly

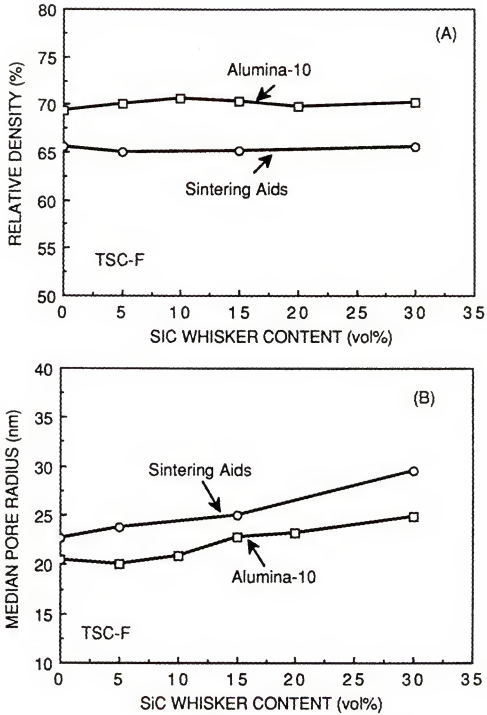

Figure 4.34 Plots of (A) relative green density and (B) median pore channel radius vs. SiC whisker content for Al_2O_3-10/TSC whisker compacts prepared with and without sintering additives.

higher suspension viscosities and higher porosities compared to the suspensions prepared at pH~4. The median pore channel radii were larger in the samples prepared with sintering additives (Figure 4.34B), which is consistent with the green density results. Again, the green density values had little dependence on whisker concentration, similar to the previous results (see Figures 4.24 and 4.28).

Figure 4.35 shows the plots of pore size distributions for different whisker/alumina ratios. The pore channel radii distributions shift slightly to larger sizes compared to those in the samples prepared at pH~4 without sintering additives, which is consistent with the lower green density and higher median pore channel radii. The green density values obtained for the samples with sintering additives are still higher compared to isostatically pressed (280-420 MPa) samples prepared by Tiegs and Becher [Tie87].

Figure 4.36 shows scanning electron micrographs of the samples prepared with sintering additives. As observed in the compacts prepared at pH~4.0, the whiskers are distributed homogeneously throughout the matrix, and the matrix regions are closely packed (Figure 4.36A). Since these samples contain the sintering additives which would form liquid phases at sintering temperatures, the homogeneous distribution of additives is another important consideration along with high green density. Based on the homogeneous distribution of the whiskers, it is likely that the sintering additives are also distributed homogeneously.

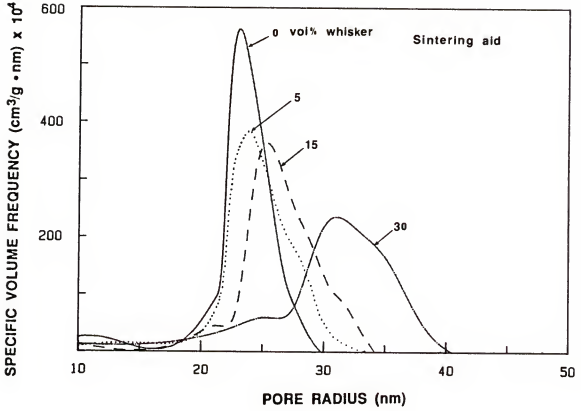

Figure 4.35 Plots of specific pore volume frequency vs. pore channel radius for the samples prepared with sintering additives and varying SiC whisker (TSC-F)/Al_2O_3-10 ratios.

(A)

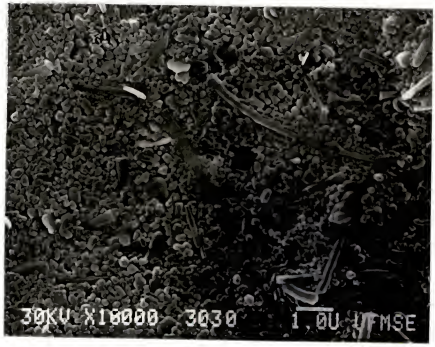

(B)

Figure 4.36 Scanning electron micrographs of the top surface of 70 vol% Al_2O_3-10/30 vol% TSC-F whisker compact prepared with sintering additives: (A) low magnification and (B) high magnification.

4.3.6 Infiltration of Matrix Precursor

Further increases in green densities of samples prepared with Al_2O_3-10 powder was successfully accomplished by infiltrating aluminum nitrate nonahydrate (ANN) into presintered Al_2O_3-10/TSC-F whisker compacts. The precursor materials were readily decomposed to Al_2O_3 during subsequent heat treatment and sintering processes. Most of volatile components from ANN were decomposed below 600°C, resulting in almost constant weight from 600-1100°C (Figure 4.8).

During multiple infiltration processing, the weight gains were monitored after heat treatment at 650°C. Figure 4.37 shows a plot of fractional weight gain (with respect to total weight gain) vs. number of infiltration cycles. The fractional weight gain was gradually decreased with repeated infiltration, indicating that the effective penetration distance increases due to changes in pore structure. This was clearly shown in a plot of filling efficiency vs. number of infiltration cycle (Figure 4.38).

Although it is difficult to predict the infiltration kinetics due to the nonideal pore structure, equation (2.62) is expected to provide a rough estimate of the infiltration depth and necessary infiltration time for a given sample thickness. The infiltration time necessary for complete infiltration was estimated to be ~10.3 minutes, using the values from literature [Gla87] (γ~0.1 J/m^2, η~40 mPa·s) and experiments (r~20 nm, d~0.2 cm). In the infiltration

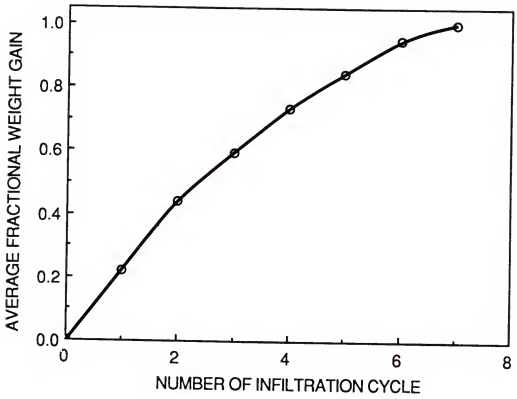

Figure 4.37 Plot of average fractional weight gain as a function of number of infiltration cycles.

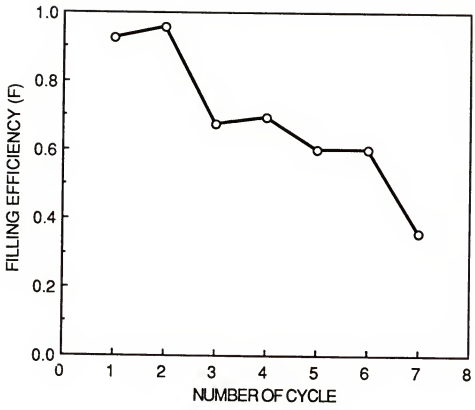

Figure 4.38 Plot of filling efficiency vs. number of infiltration cycle.

experiments, samples were allowed to be penetrated by infiltrant for ~15 minutes. To test the usefulness of the above equation, degree of filling (i.e., efficiency of filling), F, was calculated using the following equation:

$$F = \frac{\text{pore volume occupied by infiltrant}}{\text{total available pore volume}}$$

$$= \frac{\Delta W_d}{W_o} \frac{d_s}{d_i} \frac{G}{1-G} \frac{1}{1-L} \qquad (4.6)$$

where ΔW_d is the weight gain after decomposition, W_o is the original weight of presintered compact, d_s is the true density of the compact, d_i is true density of infiltrant, G is the relative density of the presintered compact, and L is the fractional weight loss of infiltrant. L was determined to be ~0.85 (from TGA result) and d_i was assumed ~1.72 g/cm^3 [Gla87]. Since it is difficult to determine the weight gain immediately following the infiltration of ANN into samples, the weight increase due to infiltrant (ANN) alone was calculated from the weight gain after decomposition at 650°C. As shown in Figure 4.38, the average degree of filling obtained for 12 samples (two samples for each whisker content) was better than 90% up to 2 cycles of infiltration. However, the degree of filling gradually decreased with increasing number of cycles, finally dropping to ~0.35 for the 7th infiltration. These results indicates that the pore tortuosity and decreased pore radii significantly slowed the infiltration rate.

Green density was estimated from the weight gain using the following equation:

$$G = G_o + \frac{\Delta W}{V_o d_i} \qquad (4.7)$$

where G is relative green density after infiltration, G_o is the original green density, ΔW is the weight gain, V_o is the total sample volume (= solid volume + pore volume), and d_i is the density of infiltrant after infiltration. The final whisker content was calculated from the weight gain, assuming from the TGA results that the increased weight converts completely to α-Al_2O_3 (density = 3.98 g/cm^3) at sintering temperatures.

Figure 4.39 shows a plot of relative density vs. whisker content which was calculated from the weight gain data. The relative densities were in the range ~80-82% for the compacts with 0-27.3 vol% calculated whisker concentrations. The relative density values obtained from Archimedes measurement and mercury porosimetry are compared with those calculated from the weight gain data. In order to obtain relative density values, it is necessary to determine the true densities of the compacts after decomposition process. The true density values were calculated from the volume ratios and helium pycnometry densities of the three materials comprising the compacts: (1) α-Al_2O_3 in the original (uninfiltrated) compact, (2) SiC whiskers in the original compact, and (3) infiltrated Al_2O_3 obtained by heat treatment of the aluminum nitrate. The relative density values obtained

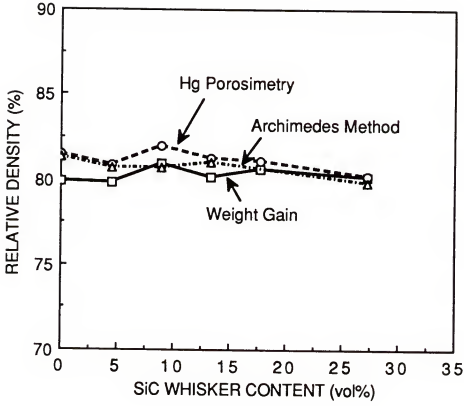

Figure 4.39 Plots of green relative density vs. SiC whisker content for the samples infiltrated with ANN.

from the three methods are in good agreement. It should be noted that the relative densities are for samples heated at 900°C for 30 min. Under these conditions, the infiltrated aluminum nitrate decomposes to a transition Al_2O_3 with a He-pycnometer density of 3.30 g/cm^3. At higher temperatures, the infiltrated Al_2O_3 transforms to α-Al_2O_3 with a concomitant increase in true density to 3.98 g/cm3. This transformation should produce an increase in the pore volume and a decrease in the relative density of the compact. However, this effect may not be observed because bulk densification of the compacts begins at temperatures which are similar to or lower than the transformation temperature.

The densities calculated from the weight gain are somewhat lower than the other methods (i.e., mercury porosimetry and Archimedes methods), especially for the samples with lower whisker contents (e.g., 0 and 4.5 vol% SiC whiskers). This indicates that the samples undergo a small amount of sintering (i.e., densification) during the 900°C heat treatment, which results in a slight reduction in the bulk volume of the samples. Due to the fine particle size of the alumina and the high compact relative density, a small amount of densification at 900°C is plausible. The density values determined from the weight gain give lower values than the other two methods because the calculation is based on the original bulk volume of the uninfiltrated compacts presintered at 650°C for 30 min. In contrast, the Archimedes and mercury porosimetry measurements are calculated using the

bulk volume of the samples heated at 900°C, in which the bulk volume of the original presintered compact does not affect the calculation.

The measured values of the open porosity of the infiltrated samples are consistent with the relative density values calculated from the Archimedes displacement method, as shown in Figure 4.40. The open porosity and relative density values add up to nearly 100% (within 1%) for each sample. Note that the open porosity values are calculated using the dry, saturated, and suspended weights of the samples. In contrast to the relative density calculation, it is unnecessary to know the true density of the sample.

Mercury porosimetry results showed that median pore channel radii decreased with infiltration (Figure 4.41), along with the increase of green relative density. Figure 4.42 shows the plot of pore size distributions for the samples infiltrated with ANN. Pore channel radii decreased with infiltration. Although the median (or mode) pore channel radii show substantially different trend from those of uninfiltrated samples, particularly at low whisker content, the effect of whiskers on pore structures was still observed at higher whisker content. One concern is that the infiltrant can migrate toward free surface during decomposition process, leaving relatively large pores inside the samples. This can result in complex pore structures. The pore size distributions (Figure 4.42) apparently show the complexity of

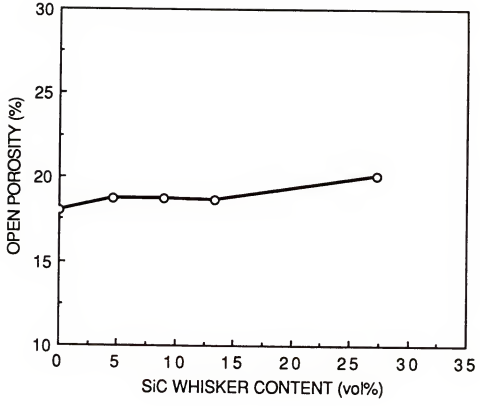

Figure 4.40 Plot of open porosity vs. SiC whisker content for the samples infiltrated with ANN.

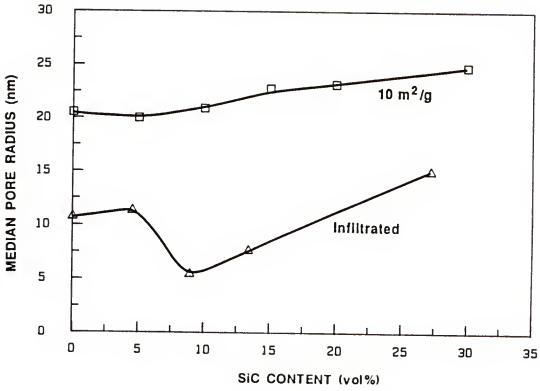

Figure 4.41 Plots of median pore channel radius vs. SiC whisker content for compacts prepared with and without infiltration.

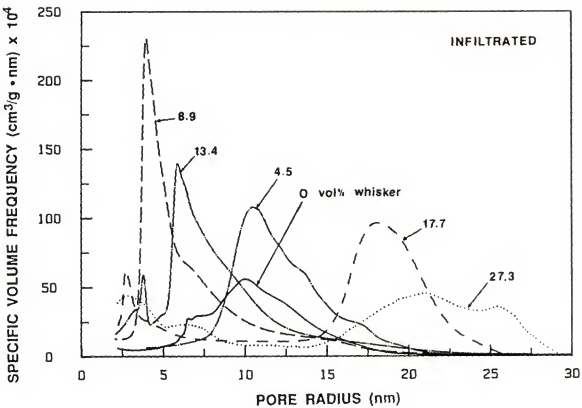

Figure 4.42 Plots of specific pore volume frequency vs. pore channel radius for the samples infiltrated with ANN after decomposition at 900°C.

pore structures and the difficulty in controlling the infiltration and subsequent decomposition process.

4.4 Densification and Microstructure

4.4.1 Dry Processing vs. Suspension Processing

As mentioned in section 4.3.2, samples uniaxially dry-pressed at 103 MPa have much lower green densities and larger median pore channel radii than the suspension-processed samples. More significantly, the green density is strongly dependent upon SiC whisker content, i.e., the green density decreases as the whisker content increases. These characteristics of the green microstructures are directly related to the densification of the composites, as well as alumina compacts prepared without whiskers. Figure 4.43 shows plots of sintered relative density vs. SiC whisker (TSC-B fraction) content of for dry-pressed and suspension-processed samples. Although sintered densities for the composite samples are relatively low at this sintering temperature, suspension-processing clearly has an advantage over dry processing. The differences in green densities between suspension-processed and dry pressed samples are directly related to the differences in sintered densities. The low sintered densities for dry-pressed samples, even at the low whisker content, suggest that more extensive whisker network structures have developed in these samples.

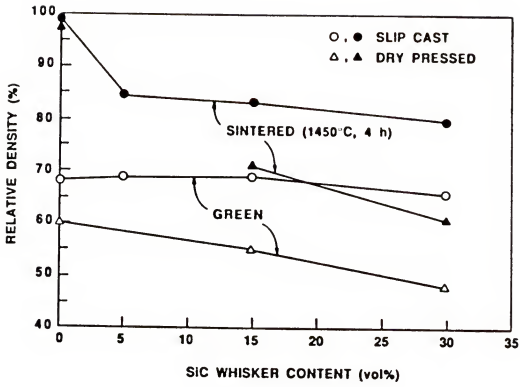

Figure 4.43 Plots of relative density vs. SiC whisker content for the samples prepared by dry-pressing and slip casting.

4.4.2 Effect of Sintering Atmosphere and Sintering Time

Since the constituents of the composites are oxide (Al_2O_3) and carbide (SiC), the sintering atmosphere is a very important processing parameter. Although inert gas (argon) was used in the sintering process, sometimes this passive protection may be insufficient to retain the chemical and physical identities of the original constituents. In this study, several atmospheres have been tested during sintering. When the composite samples with 15 and 30 vol% whiskers were sintered in a vacuum, the weight loss values were 13.6% and 21.6%, respectively. The density for the samples sintered in a vacuum was not measured. Table 4.9 summarizes the effect of sintering atmosphere on densification of Al_2O_3-8/TSC-B SiC whisker composites. In this table, "Ar" designates the stagnant argon gas atmosphere. Sintering in flowing argon, "Ar (flowing)," at 1700°C resulted in weight loss of 11.6%, indicating that the reaction equilibrium could not maintained due to the continuous removal of reaction product gases. The 30 vol% SiC whisker composite sintered in a nitrogen/2% hydrogen atmosphere (N_2/H_2) at 1700°C resulted in extensive weight loss (~12%). This may be due to the decomposition of alumina matrix under very low oxygen partial pressure [Mar86, Sat84].

In order to actively protect SiC, an embedding powder was used to avoid extensive decomposition reactions (and weight loss). Also, reactions leading to weight loss were minimized by using a stagnant argon atmosphere, so that a

Table 4.9 Effect of sintering conditions on the densification and weight loss

Sintering Atmosphere Gas, Embedding powder	Sintering Schedule Temperature (time)	Relative Density (% Weight Loss) 5 vol% whisker	15 vol% whisker	30 vol% whisker
Ar, SiC(w)	1700°C, 15 min	95.5(1.1)	85.0(1.3)	71.8(3.3)
Ar, SiC(w)	1700°C, 30 min	95.2(1.6)	93.4(1.9)	74.3(2.9)
Ar, SiC(w)	1700°C, 60 min	97.3(1.3)	84.7(3.1)	63.7(4.0)
Ar, Al_2O_3/SiC(w)	1700°C, 15 min	99.4(0.9)	82.6(1.0)	68.0(1.1)
N_2/H_2, SiC(w)	1700°C, 30 min	-	-	58.5(12)
Ar (flowing)	1700°C, 30 min	-	- (11.6)	-
Ar, SiC(w)	1800°C, 30 min	95.2(1.5)	92.7(2.1)	76.6(4.0)

high partial pressure of the reaction product gases was maintained near the sample.

The combination of an argon atmosphere and Al_2O_3/SiC(w) embedding powder showed significantly lower weight losses. The reduced weight loss may be attributed to the high partial pressure of Al_2O and SiO gases in the stagnant argon atmosphere which can subdue or reverse the decomposition reactions of SiC whiskers and Al_2O_3. Even though the combination of argon and Al_2O_3/SiC(w) embedding powder was effective in reducing weight loss, there was an extensive surface reaction in which the embedding powder reacted with composite samples with 30 vol% whiskers. (The reaction products were not identified.) This reaction was not observed in samples sintered with the combination of argon atmosphere and SiC(w) embedding powder. Furthermore, slightly higher sintered relative densities were obtained for the 15 and 30 vol% SiC whisker composites compared to the combination an argon atmosphere and Al_2O_3/SiC(w) embedding powder. In addition, the weight loss values obtained in the combination of argon and SiC(w) are still relatively low. These values are similar or lower compared to values reported by Tiegs and Becher for hot pressed samples [Tie86]. Since the combination of stagnant argon atmosphere and SiC(w) protection powder was effective in reducing extensive weight loss and gave clean sintered surface for all whisker concentrations, this combination was used for the rest of the sintering study.

Another condition to be determined was the sintering time. Table 4.9 shows that too long sintering time (e.g., 60 min) led to desintering, presumably due to a high pressure of entrapped gases. Thus, the sintering time used in the rest of this study was 30 min. However, for the best results, the sintering time should be adjusted, depending upon the sintering temperature and SiC whisker concentration.

4.4.3 Effect of Whisker Aspect Ratio

Figure 4.44 shows plots of relative density vs. sintering temperature for the samples prepared with the whisker aspect ratios of 14 (TSC-C) and 21 (TSC-A). Figures 4.44(A) and 4.44(B) show that shorter whisker aspect ratio eventually improved densification behavior of composites at 5 and 15 vol% whisker content, as expected, but not until sintering temperatures of 1600-1700°C were reached.

At 5 vol% whisker content, the relative density for the samples prepared with TSC-C whiskers (L/D=14) was lower up to 1600°C, above which the relative density for the samples with TSC-C whiskers was higher than those with TSC-A (L/D=21).

At 15 vol% whisker content, the relative density of samples with TSC-A (L/D=21) was higher than those with TSC-C (L/D=14) up to 1700°C, above which the sintered density for the samples with lower aspect ratio was finally higher.

The unexpected difference in the sintered density values at lower sintering temperature can be explained in terms of green microstructures. Table 4.10 shows the characteristics of green microstructures for composites with TSC-A (L/D=21)

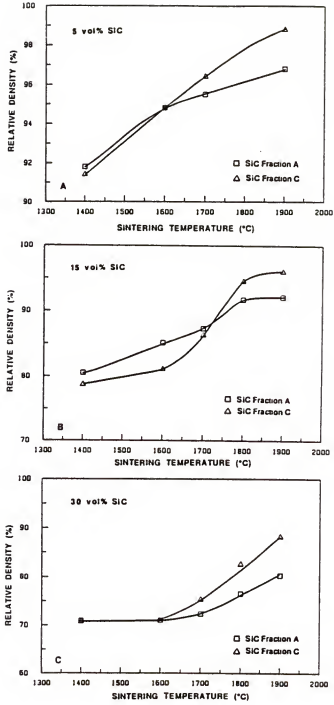

Figure 4.44 Plots of relative density vs. sintering temperature for the samples prepared with whisker aspect ratios of 14 and 21 at whisker concentration of (A) 5 vol%, (B) 15 vol%, and (C) 30 vol%.

Table 4.10 Green microstructural characteristics of green compacts prepared with different whisker aspect ratios

Whisker Type	SiC whisker Content (vol%)	Green Density (%)	Median Pore Radius (nm)
TSC-A	5	68.9	31.8
TSC-A	15	68.5	33.7
TSC-A	30	68.3	39.6
TSC-C	5	68.2	33.3
TSC-C	15	67.9	36.7
TSC-C	30	66.7	41.7

and TSC-C (L/D=14) whiskers. The compacts with TSC-A whiskers have higher green relative densities and smaller pore sizes for each whisker concentration. As a result, in the early stage of sintering, the sintered density for the samples with TSC-A whiskers was higher despite higher aspect ratio (or whisker length). However, as sintering proceeded, the sintered density for the samples with TSC-C whiskers was higher due to the reduced whisker aspect ratio (or length). For example, the sintered relative densities for the samples prepared with 15 vol% TSC-A and TSC-C whiskers were ~91.4 and 94.0% at 1800°C, respectively.

At 30 vol% whisker content, composites did not densify at temperature of 1400-1600°C even though these temperatures are high enough to densify matrix Al_2O_3. At temperatures higher than 1700°C, the reduced whisker aspect ratio (e.g., TSC-C whiskers) resulted in enhanced densification behavior of composites. At 1900°C, the sintered relative densities for the samples with TSC-A and TSC-C whiskers were ~79.9 and 87.5%, respectively.

The difference in sintered densities between samples prepared with whiskers of different aspect ratios at 1800-1900°C increases as whisker content increases. As predicted in percolation model and fiber packing studies [Zal83; Boi83; Hol89; Mil78], this indicates that the resistant whisker networks form at lower whisker content in the samples containing whiskers with higher aspect ratio. This behavior is consistent with the work by Tiegs and Becher [Tie87], in

which they reduced whisker aspect ratio by ball-milling for 4 hr. The densification behavior was greatly enhanced with milled whiskers. Even though the theory predicted that densification rate is only dependent upon the volume fraction of the non-sintering phase [Hsu86, Rah87, Rah88, Raj84], the results obtained by present study illustrate that the densification behavior of composites is dependent on not only the volume fraction of inert particles, but also their sizes.

In addition to the difficulty in achieving high relative densities, samples with higher whisker contents also lose more weight during the sintering process. Table 4.11 shows the weight loss for Al_2O_3-8/TSC whisker compacts sintered at 1700°C and 1800°C. In order to minimize the effect of absorbed water vapor, the green compacts were treated at 180°C for 48 hr before sintering at given temperatures.

Measured weight losses with 5 and 15 vol% SiC whiskers were typically in the range of ~0.6-1.2% and ~1.6-1.8% following sintering at 1700°C and 1800°C, respectively, while considerably higher weight losses were observed for 70 vol% Al_2O_3/30 vol% SiC whisker samples (~1.7-1.9% and ~2.8-4.3% after sintering at 1700°C and 1800°C, respectively). Although differences in intrinsic volatilization rates of Al_2O_3, SiC, and/or reaction product could account for the weight loss difference, the slow densification rate in 70 vol% Al_2O_3/30 vol% SiC whisker samples is probably the most important factor contributing to the higher weight losses. In these samples, there is a large amount of internal surface area

Table 4.11 Percent weight loss for samples prepared with TSC-A (L/D=21) and TSC-C (L/D=14) whiskers

Whisker type	Whisker content (vol%)	Weight loss (%) 1700°C	1800°C
TSC-A	5	0.72	1.73
TSC-A	15	1.19	1.79
TSC-A	30	1.68	2.80
TSC-C	5	0.56	1.59
TSC-C	15	1.06	1.67
TSC-C	30	1.94	4.33

(i.e., open porosity) of the compacts which remains accessible for direct volatilization, vapor transport out of the samples, and continuous contact between reaction gases and samples.

Tiegs and Becher [Tie86] reported the weight losses for 80 vol% Al_2O_3/20 vol% SiC whisker samples prepared with whiskers of different commercial sources after hot-pressing at 1850°C. The weight losses in their samples were in the range of 0.8-4.85% depending on the sources of whiskers. The weight loss was 1.53% for the same whiskers as used in the present study, which is slightly lower than the weight loss obtained for the samples with 15 vol% whiskers. This can be attributed to the higher density of hot-pressed samples in comparison with the pressureless sintered samples.

Homeny et al. [Hom87] suggested that hot pressing would suppress the partial pressure of production gases to a minimum level which is not sufficient for substantial reaction to take place. However, a comparison between the present study and the work by Tiegs and Becher [Tie86] indicates that even pressureless sintering can minimize the weight loss by enhancing densification through green microstructures, and by using a relatively active protection atmosphere.

4.4.4 Effect of Matrix Particle Size

4.4.2.1 Densification of Al_2O_3 without SiC whiskers. Figure 4.45 shows plots of relative density vs. sintering temperature for pure Al_2O_3-10 samples. The relative

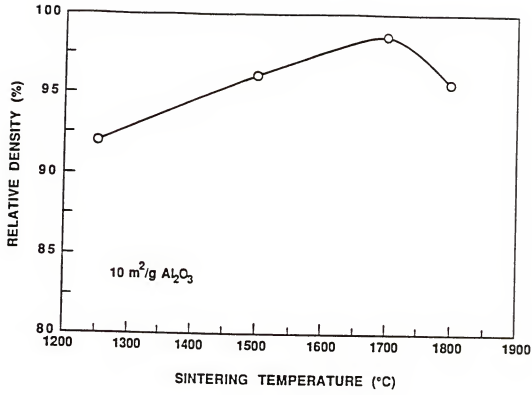

Figure 4.45 Plot of relative density vs. sintering temperature for the alumina-10 samples.

density at 1250°C was ~92 % in the atmosphere used in this study, while the sintered density in air was ~95 %. The pure Al_2O_3 sample reached almost theoretical density after sintering in air at 1500°C for 30 minutes, whereas, the density of the sample sintered in a SiC whisker packing powder under static argon atmosphere was only ~96 %. When the sintering temperature was increased to 1700°C, the relative density reached ~99% in the SiC whisker packing powder/static argon atmosphere before decreasing to ~94 % at 1800°C. This decrease in density at 1800°C is attributed to bloating (i.e., pore volume expansion) which arises from higher pressures of gases entrapped within the closed pores at higher temperatures [Bur57].

As shown in the SEM micrographs (Figure 4.46), the sample sintered at 1250°C shows substantial grain growth occurs while still maintaining relatively equiaxed grain shapes. However, large abnormal grains are observed at 1500°C which are much larger than the average grain intercept size. It is likely that the appearance of the abnormal grains is related to the sintering atmosphere (i.e., SiO) [Kay87; Han89], since the surface silica on the packing SiC powder can be decomposed to SiO gas under the reducing atmosphere. The sample sintered at 1700°C returns to relatively equiaxed and uniform grain structure, which is the result of highly irregular movement of the grain boundaries to form metastable grain structure upon the impingements between large abnormal grains in the fine matrix grains [Cob59]. There are a few

(A)

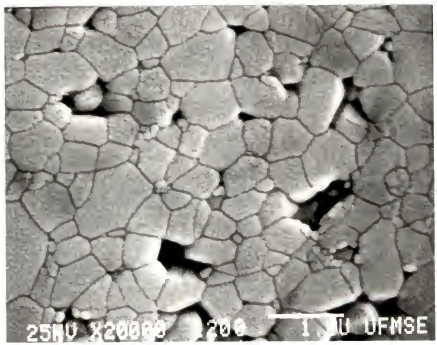

(B)

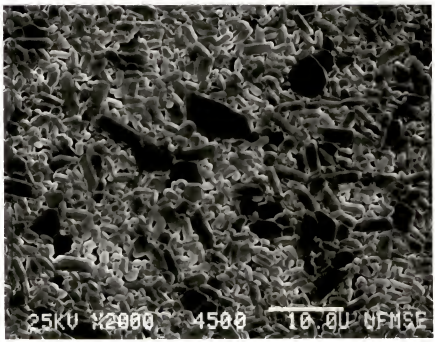

Figure 4.46 Scanning electron micrographs showing the changes in grain and pore microstructures for pure alumina-10 samples sintered at (A) 1250°C and (B) 1500°C.

(C)

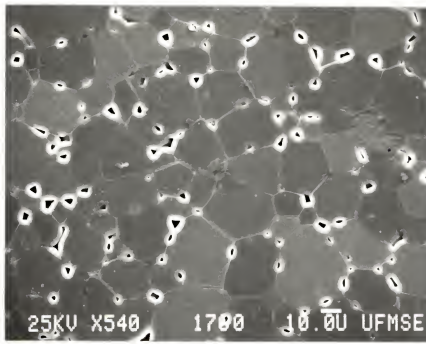

(D)

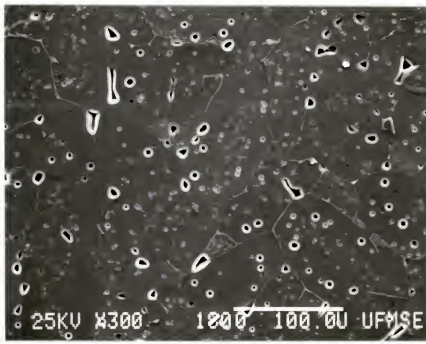

Figure 4.46 Scanning electron micrographs showing the changes in grain and pore microstructures for pure alumina-10 samples sintered at (C) 1700°C and (D) 1800°C.

spherical pores (or bubbles) inside the grains. Most of the spherical pores inside the grains have much smaller dimensions in comparison to the pores located at the grain boundaries and grain corners. In contrast to the microstructure observed in the sample sintered at 1700°C, the sample sintered at 1800°C had very large abnormal grains of about several hundred micrometers, with many large spherical pores within the grains. These pores, which indicate that bloating occurs, are consistent with the densification data in Figure 4.45.

4.4.2.2 Densification behavior of composite. Figure 4.47 shows the relative density as a function of sintering temperature for compacts prepared with Al_2O_3-10 and Al_2O_3-27 powders at three different whisker concentrations (5, 15, and 30 vol%). The importance of the sintering activity of the matrix phase is evident in the samples prepared with 95 vol% Al_2O_3/5 vol% SiC whiskers (Figure 4.47A). The Al_2O_3-27 sample sintered to ~97% relative density at only 1250°C. Those samples reached relative densities above 98% at 1500°C before decreasing at the higher sintering temperatures (1700-1800°C). The decrease in density above 1500°C may be due to bloating. This interpretation is suggested by open porosity measurements which show that almost all of the residual porosity is closed after sintering at only 1250°C (Figure 4.48A). After pore closure occurs, entrapped argon (i.e., the gas atmosphere during sintering) would be difficult to remove

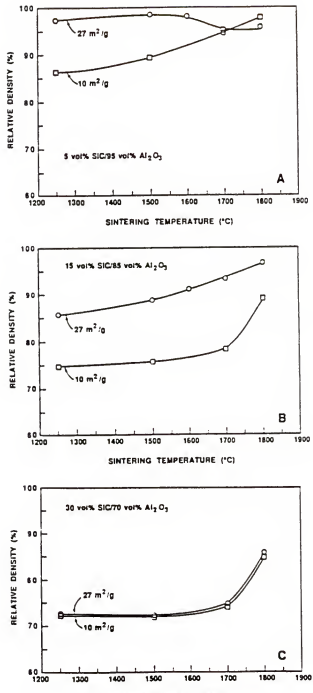

Figure 4.47 Plots of relative density vs. sintering temperature for samples prepared with Al_2O_3-10 and 27 powders and with varying Al_2O_3/SiC whisker ratios: (A) 5 vol% SiC/95 vol% Al_2O_3, (B) 15 vol% SiC/85 vol% Al_2O_3, and (C) 30 vol% SiC/70 vol% Al_2O_3.

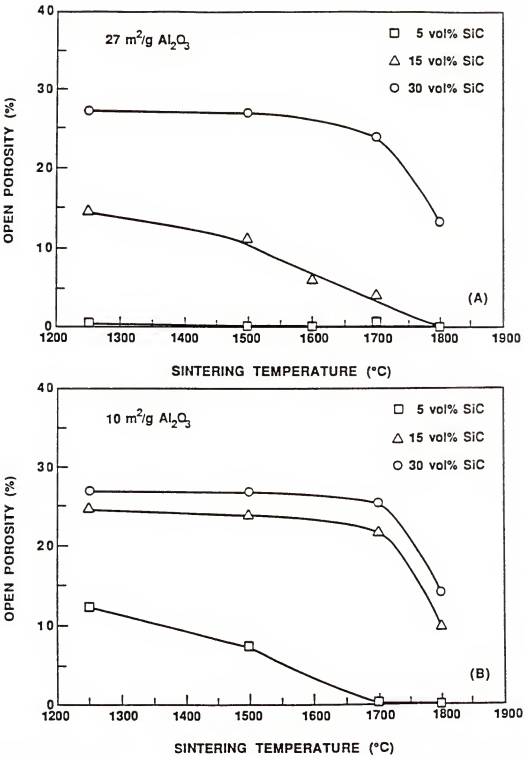

Figure 4.48 Plots of open porosity vs. sintering temperature for samples prepared with varying Al_2O_3/SiC whisker ratio and with different matrix particle sizes: (A) alumina-27 and (B) alumina-10.

since the diffusion rate of the gas molecules through the high density Al_2O_3/SiC compact is expected to be low.

In contrast to the densification behavior of the Al_2O_3-27 samples, compacts prepared from the lower surface area powder (Al_2O_3-10) densified much more slowly. The relative density eventually reached ~98%, but not until the sintering temperature was 1800°C. This temperature was also required to produce samples with no open porosity (Figure 4.48B).

Figure 4.49 directly illustrates the adverse effect of even small concentrations of whiskers on densification of composites. Plots of relative density vs. whisker concentration are shown for samples prepared with Al_2O_3-10 and sintered at 1250°C and 1500°C. The addition of only 5 vol% SiC whiskers reduces the sintered relative density from ~92 to ~86% for the samples sintered at 1250°C, and from ~96% to ~89% for the samples sintered at 1500°C. The same effect is observed for the samples prepared with alumina-27 powder. For example, an alumina sample sinters at 1250°C to ~99%, compared with a composite sample with 5 vol% SiC whiskers which sinters at 1250°C to ~97%.

The matrix particle size still has an important effect on densification for samples prepared with 85 vol% Al_2O_3/15 vol% SiC whiskers (figure 4.47B). However, it is evident from Figure 4.47-49 that the higher whisker concentration severely inhibits densification for both Al_2O_3-10 and Al_2O_3-27 samples. The Al_2O_3-10 sample reached only ~89% relative density at 1800°C, and Figure 4.48B shows that a

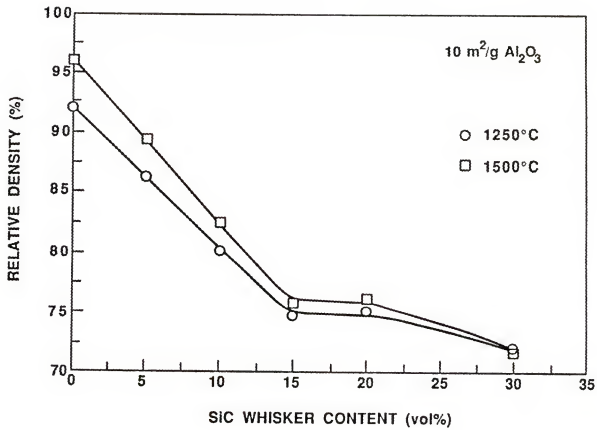

Figure 4.49 Plots of sintered relative density vs. SiC whisker content for samples sintered at 1250 and 1500°C. Samples were prepared with alumina-10 powder.

large amount of open porosity remains (~10%). With the Al_2O_3-27 samples, it was still possible to achieve high relative densities (~97%) after sintering at 1800°C. In addition, all of the residual pores in this sample are closed, as shown in Figure 4.48A. (Thus, samples could be densified further by hot isostatic pressing (HIP) without glass encapsulation, which is an expensive and time consuming process.) Due to the relatively high aspect ratio of the SiC whiskers, considerable development of a continuous network structure is expected in the green compacts prepared with 15 vol% whiskers. As the bulk compact densifies, whiskers are brought into closer proximity and even more extensive development of the network occurs. This results in considerable constraint upon densification for both the Al_2O_3-10 and Al_2O_3-27 composites.

Although reducing the matrix particle size can be used to enhance densification behavior of composites, the effect is dependent on the magnitude of the constraints upon densification that are introduced into the system. This is illustrated in Figure 4.47C for samples with 70 vol% Al_2O_3/30 vol% SiC whiskers prepared with Al_2O_3-10 and Al_2O_3-27 powders. The matrix particle size has negligible influence on the densification behavior of composites. For both the Al_2O_3-10 and Al_2O_3-27 samples, very little densification occurs due to the high loadings of whiskers until sintering temperature exceeds 1700°C. Even at 1800°C, sintered relative densities for Al_2O_3-10 and Al_2O_3-27 samples were only ~85 and ~86%,

respectively. In addition, significant amounts of open porosity remain in these samples (Figure 4.48).

Even though there have been a number of theoretical predictions on the constrained sintering, the lack of isothermal sintering data made it impossible to apply these theories to the present study. Thus, Lange's constrained network model was applied to evaluate the densification behavior (see eq (2.37)). In the constrained network model, the density of the composites was related to that of the matrix alone by adjusting the numerical constant (α) depending on the inclusion volume fraction. The numerical constant, α, represents the interspacing distance between inclusions located on lattice points in the tetrakaidecahedron unit cell, which, in turn, is an indicator of the degree of restraining force imposed by inclusion particles against sintering force (i.e., at a given inclusion concentration, a small α value indicates more constraints of the matrix densification). In Figure 4.50, the numerical constant values obtained for Al_2O_3-10 composites sintered at 1700°C were compared with those calculated by Lange [Lan87] from densification data for SiC/ZnO composites reported by DeJonge et al. [DeJ86]. The numerical constants at lower whisker contents are much higher in the present study compared to Lange's calculated values. For example, α is 5.1 for the sample with 5 vol% whiskers in the present study while it is 1.4 for the sample with 6 vol% SiC inclusion in Lange's data. This indicates that a stronger resistance

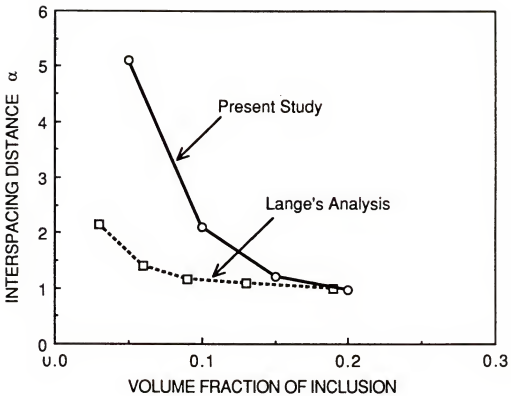

Figure 4.50 Comparison of the parameter α calculated from the present study and obtained by Lange from the work by DeJonge and coworkers [Lan87].

against matrix sintering deformation arises from SiC whiskers in an Al_2O_3 matrix than from SiC particles in a ZnO matrix.

The discrepancy can be explained in several ways. First, the model assumes a wrong lattice structure for the packing of inclusion particles. For example, Lange assumed that the limiting inclusion volume fraction is 0.277 based on tetrakaidecahedron lattice [Lan87]. The model predicts, with the limiting volume fraction of 0.277, that the maximum α value is 3.16, but the sample with 5 vol% whisker has 5.10. This indicates that the assumption made for this model overestimates the effect of inclusions on densification of composites. Second, The overestimated inclusion effect on the composite densification is partly due to the additional retardation of densification in the presence of the inhomogeneities (e.g., agglomerates) in the compacts . He attempted to fit the sintered densities of the dry-pressed SiC/ZnO composites to his model. The microstructural inhomogeneities have been commonly observed in the dry-pressed samples [Dyn84; Yeh89]. Third, there is a possibility that the whiskers in the present study have preferred orientation as observed by Hoffmann et al. [Hof89]. However, even with preferred whisker orientation, the calculated α is still higher at 5 vol% whisker content since the maximum distance/lattice parameter ratio between lattice points in any two dimensional lattice is much smaller than 5.1.

However, at higher inclusion contents (>15 vol%), the difference is quite small indicating that the model is insensitive to small densification at high inclusion contents.

Even though viscoelastic models in heterogeneous sintering have been studied for the past few years, it is very difficult to apply theses theories to experimental data due to the lack of viscoelastic data of porous compacts. In order to illustrate the stress level arising in the presence of whiskers, the relative sintering driving force was calculated using the approach by Dynys and Halloran [Dyn84]. They evaluated the effect of aggregates on the sintering driving force of Al_2O_3 using Coble's hot pressing model [Cob70]. Using equation (2.24), the driving force for composite densification was calculated in reference to the densification of sample without whiskers, i.e., relative driving force. The variation of driving force with whisker content is summarized in Table 4.12.

Even though the model can be applied only to the early stage of sintering, samples with >85% relative density were included for comparison. However, the ratio of the relative sintering driving forces between two arbitrary samples in the early stage of sintering is still valid. In general, the relative driving forces increase as the sintering temperature increases. This behavior is consistent with the theoretical and experimental results [Hsu86; Bro88a; Bro88b]. The relative sintering driving forces decrease rapidly as SiC

whisker content is higher than 15 vol%. For example, the driving force ratio of 30 vol% whisker composite to 10 vol% whisker composite is only 0.04 at 1500°C, indicating that the sintering driving force for the 30 vol% whisker composite is dramatically reduced in the presence of whiskers and/or whisker network structures.

Dynys and Halloran [Dyn84] found that increasing aggregates amount from 6 to 20 vol% reduces the driving force by about 30%. In contrast, increasing whisker content from 5 to 20 vol% in whisker composites sintered at 1500°C reduces the driving force by ~85%. The degree of driving force reduction in whisker composite is much more rapid compared to that obtained by Dynys and Halloran [Dyn84]. The difference between results obtained in the present study and Dynys and Halloran's suggests that the constrained sintering in the presence of inclusions is strongly dependent not only upon the volume fraction but also the geometry of the inclusions.

The densification behavior of composites containing non-sintering inclusions is dependent upon the creep response of the matrix to the stresses caused by inclusions. Theoretical and experimental works showed that the stress relaxation process depends upon the spacing of the inhomogeneities and the rate at which matter can flow. In polycrystalline ceramics, it is related to Nabarro-Herring or Coble creep. Thus, in addition to the diffusion coefficient it is also depends on the grain size since matter must be transferred across a distance of grain size to achieve shear deformation

Table 4.12 Relative sintering driving force for the samples prepared with alumina-10

SiC Whisker Content (vol%)	Sintering Temperature (°C) 1250	1500	1700
0	1.00	1.00	1.00
5	0.57	0.58	0.78
10	0.21	0.24	0.44
15	0.05	0.06	0.11
20	0.07	0.08	0.08
30	0.01	0.01	0.03

to accommodate the stresses imposed on the matrix grains by inclusions. A polycrystalline material which deforms by grain boundary sliding with diffusional accommodations behaves as if it had a Newtonian viscosity, η, defined by

$$\dot{\gamma} = \frac{\tau_a}{\eta} \tag{4.8}$$

where τ_a is the applied shear stress arising from the inhomogeneities. For volume diffusion [Her50],

$$\eta_v = \frac{1}{42} \frac{d^2 kT}{D_v \Omega} \tag{4.9}$$

and for boundary diffusion [Cob63],

$$\eta_B = \frac{1}{132} \frac{d^3 kT}{\delta D_B \Omega} \tag{4.10}$$

where d is the grain size, D_v is the volume diffusion coefficient, D_B is the grain boundary diffusion coefficient, Ω is the atomic volume, and δ is the effective cross-section of a grain boundary for diffusional transport. From equations (4.9) and (4.10), it is obvious that shear viscosity is a strong function of the grain size. Therefore, the samples prepared with the Al_2O_3-27 powder can effectively release the stresses developed by whiskers due to the decreased shear viscosity at low whisker contents (<15 vol%).

4.4.2.3 Microstructure characterization. Figure 4.51 shows a X-ray diffraction pattern for the 30 vol% whisker composite prepared with Al_2O_3-27 powder which was sintered at 1800°C. X-ray diffraction analysis reveals that only α-Al_2O_3 and SiC (α and β) exist, indicating that no reaction between

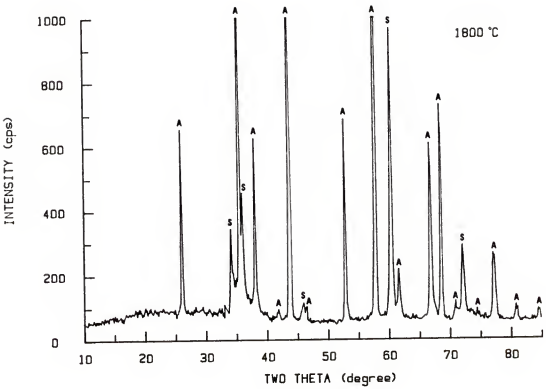

Figure 4.51 X-ray diffraction pattern for the 30 vol% SiC whisker composite prepared with the alumina-27 powder and sintered at 1800°C for 30 min.

constituents occurred. Observations by transmission electron microscopy also did not reveal any interfacial reactions between the Al_2O_3 and SiC whiskers (Figure 4.52). As shown in Figure 4.52, the interface between Al_2O_3 and SiC whiskers and the triple grain junction of alumina showed no indication of any reaction. Although x-ray photoelectron spectroscopy showed that there were Si-O bonds on the surfaces of the starting SiC whiskers [Ada88], no evidence for a reaction between silica and alumina (i.e., to form mullite) was detected in the sintered samples. The lack of reaction between the Al_2O_3 and SiC whiskers is consistent with the results obtained by Becher and Tiegs [Beche86]. Any silica-rich layer on the whisker surfaces was presumably removed during sintering process. At low oxygen partial pressures, silica would be unstable during sintering and volatilization of silicon monoxide would be expected [Fit74]. It is reasonable to assume that SiC whiskers possess ~1.5 wt% of SiO_2 based on the oxygen amount determined from the elemental analysis [Mah85]. If all the SiO_2 is removed during sintering, the volatilization of surface silica alone can account for a weight loss of ~0.4% for the 70 vol% Al_2O_3/30 vol% SiC whisker compacts [Mah84].

Figure 4.53 shows the average grain intercept size of the alumina matrix as a function of sintering temperature for compacts prepared with alumina-10 powder and various SiC whisker concentrations (0-30 vol%). At each sintering temperature, smaller average grain intercept sizes were

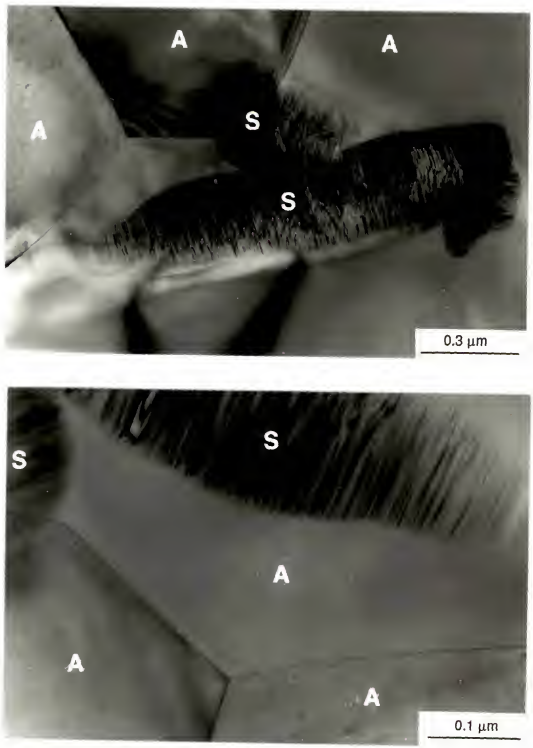

Figure 4.52 Transmission electron micrographs of the sample prepared with 85 vol% Al_2O_3-10/15 vol% TSC-F SiC whisker sample sintered at 1800°C.

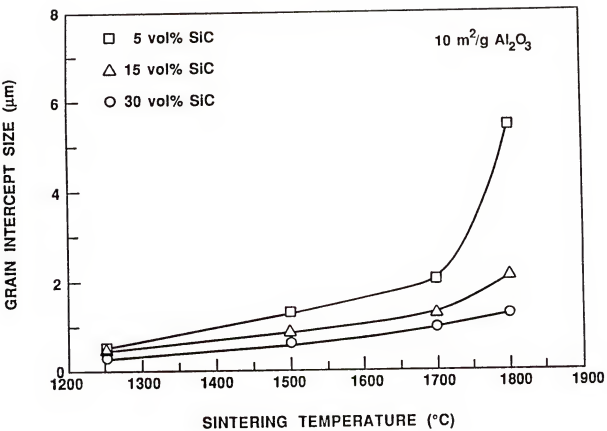

Figure 4.53 Plots of average grain intercept size vs. sintering temperature for samples prepared with varying Al_2O_3/SiC whisker ratio. Samples were prepared with alumina-10 powder.

measured for samples with higher whisker concentrations. There are two probable reasons for this observation. First, it is well known that inclusion particles are effective in pinning grain boundaries, thereby, reducing grain growth rates. Less grain growth would be expected with higher concentrations of inclusion particles (i.e., whiskers). Second, at a given sintering temperature, samples with higher whisker concentrations have a larger volume fraction of pores (i.e., lower relative density). Pores are also very effective in pinning grain boundaries. Figure 4.53 shows that the grain size increases substantially between 1700°C and 1800°C for the samples with 5 vol% SiC whiskers. The sample sintered at 1700°C has a relative density of ~95%, and there is essentially no open porosity. Thus, there is limited restraint on grain growth from pores. The large increase in grain size between 1700°C and 1800°C suggests that many of the Al_2O_3 grains have grown to sizes comparable to the whisker lengths, i.e., large enough for the grain boundaries to sweep past the whisker inclusions. This is evident from microstructure observations which show a large amount of SiC whiskers entrapped within Al_2O_3 grains (Figure 4.60).

Despite this relatively rapid grain growth, a comparison with pure Al_2O_3 samples suggests that even small concentrations of whiskers provide some restraint on grain growth especially in high density samples in which grain boundary pinning from pores is less important. Figure 4.54 shows a plot of average grain intercept size vs. sintering

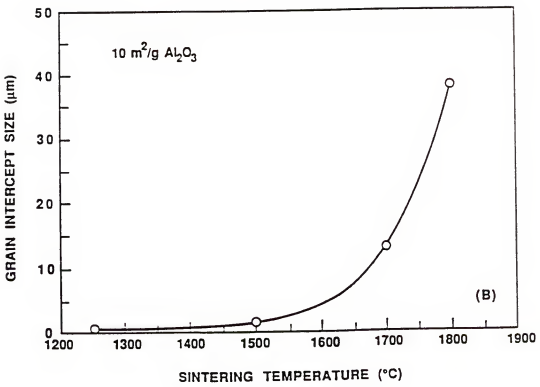

Figure 4.54 Plots of average grain intercept size vs. sintering temperature for pure alumina-10 powder compacts.

temperature for pure Al_2O_3-10 samples which were sintered under the same conditions as the Al_2O_3/SiC composites. At sintering temperatures above 1500°C, where the samples have relative density >96% and no open porosity, there is extremely rapid grain growth, including the development of large abnormal grains (Figure 4.46 and Figure 4.54). The Al_2O_3 sample sintered at 1700°C has an average grain intercept size (~12.9 μm) more than twice that of the 95 vol% Al_2O_3/5 vol% SiC whisker composites (~5.5 μm) sintered at 1800°C, even though the samples have approximately the same relative density.

Although the SiC whiskers provide some restraint on grain growth, increase in grain size begins at considerably lower relative densities in the composite samples as compared to pure Al_2O_3 samples. This is true at all whisker concentrations, but is particularly evident in samples with the highest whisker concentration. For example, between 1250°C and 1700°C, the relative density of 70 vol% Al_2O_3-10/30 vol% SiC whisker composites increases only from ~72 to ~74%, but the average grain intercept size increases more than three-fold (i.e., ~0.28 μm to ~0.94 μm). In suspension-processed samples without SiC whiskers, there is no grain growth until relative densities approach ~90% [Yeh89]. It is apparent that the whiskers are more effective in inhibiting densification compared to grain growth.

The microstructure evolution in the samples with high whisker concentrations is somewhat analogous to the case of

sintering of powder compacts in which the particle size distribution is bimodal and the volume of coarse particles is large enough to form a continuous network [Ono77a; Ono77b; Smi84]. In such cases, the fine particles located in the interstitial space formed by the coarse particle network can undergo local densification and grain growth at relatively low temperatures, but the bulk compact shows negligible macroscopic densification until considerably higher temperatures are reached. In whisker-containing composites, the high aspect ratio whiskers can form network structures at relatively low volume fractions [Boi83; Hol89]. These networks prevent densification of the bulk compact at low sintering temperatures. However, regions containing the Al_2O_3 particles can undergo considerable local densification and grain growth. This is shown in Figures 4.55 and 4.56 in which green and sintered (at 1250°C) compacts are compared for both alumina-10 and alumina-27 composites with 30 vol% SiC whiskers. Despite the extensive local densification and grain growth, the composite relative density only increases from ~70% for the green compacts to ~72-73% after sintering at 1250°C. Note that the pure Al_2O_3 samples sinter at 1250°C to ~92% relative density for Al_2O_3-10 powder, and ~99% relative density for the Al_2O_3-27 powder.

The local densification and the coarsening of the Al_2O_3 particles reduce the driving force and increase the diffusion path lengths for macroscopic densification of the composites as discussed earlier. In addition, as regions of densely-

(A)

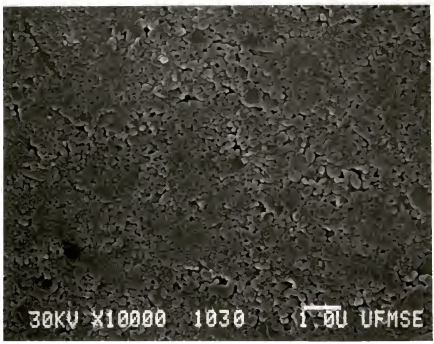

(B)

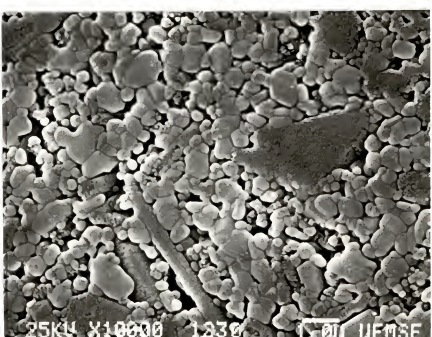

Figure 4.55 Scanning electron micrographs showing 70 vol% /30 vol% SiC whisker samples (A) before and (B) after sintering at 1250°C (30 min). Samples are prepared with alumina-10 powder.

(A)

(B)

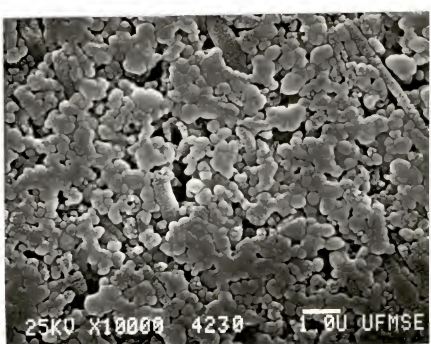

Figure 4.56 Scanning electron micrographs showing 70 vol% Al_2O_3/30 vol% SiC whisker samples (A) before and (B) after sintering at 1250°C (30 min). Samples are prepared with alumina-27 powder.

packed alumina particles shrink (i.e., as densification proceeds), large porous regions open up pulling away from whiskers, which is shown in Figure 4.57-64.

The average pore size increases with increasing sintering temperature in a manner similar to the increase in grain size. This is clearly shown in Figure 4.57-59 for the alumina-10 composites with 30 vol% SiC whiskers which were sintered in the range 1250-1700°C.

Since the grains and larger pores in Figure 4.59C have similar sizes, the possibility that the pores resulted from grain pull-outs during the polishing process was considered. However, quantitative microscopy measurements of the pore volume fraction, V_p, for composite samples prepared with both the alumina-10 and alumina-27 powder showed that this was not the case. Figure 4.65 shows that there is excellent agreement between the relative density values determined independently from the point counting method and the Archimedes displacement method.

Coarsening of the microstructure during sintering was also confirmed by measurements of the specific surface area by the BET method for 70 vol% Al_2O_3/30 vol% SiC whisker compacts sintered at various temperatures. Measurements were made for composites prepared with both the Al_2O_3-10 and Al_2O_3-27 powders. As shown in Table 4.13, the surface area for the alumina-10 composites decreases from ~7.2 m^2/g for a compact calcined at 700°C for 30 min, to ~1.0 m^2/g for a sample sintered at 1700°C for 30 min. The surface area

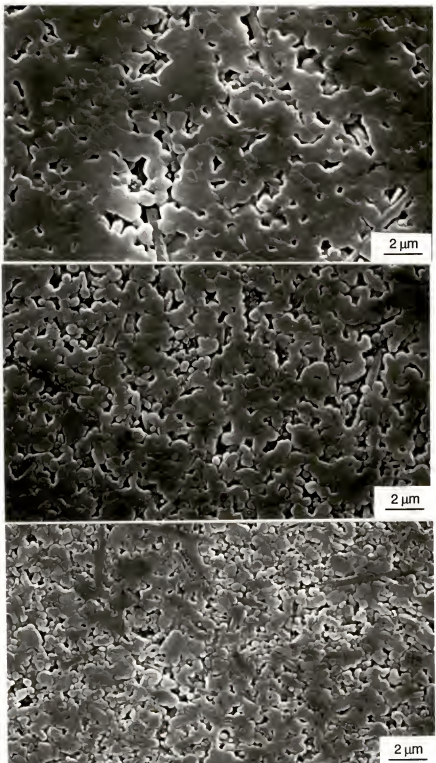

Figure 4.57 Scanning electron micrographs for the composites prepared with alumina-10 at the sintering temperature of 1250°C: (A) 5 vol%, (B) 15 vol%, and (C) 30 vol% whiskers.

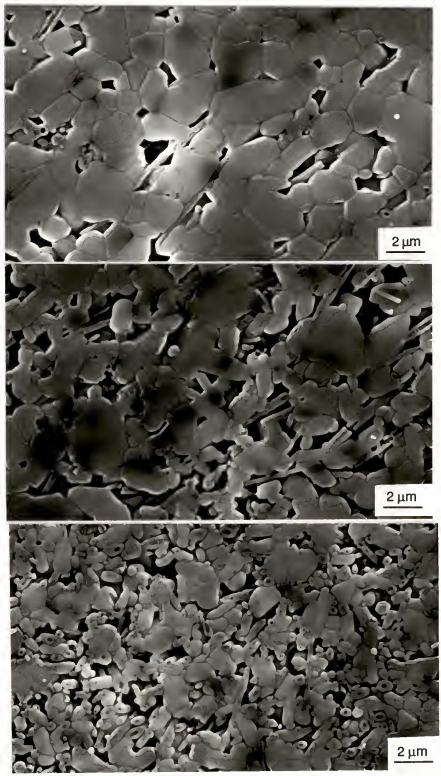

Figure 4.58 Scanning electron micrographs for the composites prepared with alumina-10 at the sintering temperature of 1500°C: (A) 5 vol%, (B) 15 vol%, and (C) 30 vol% whiskers.

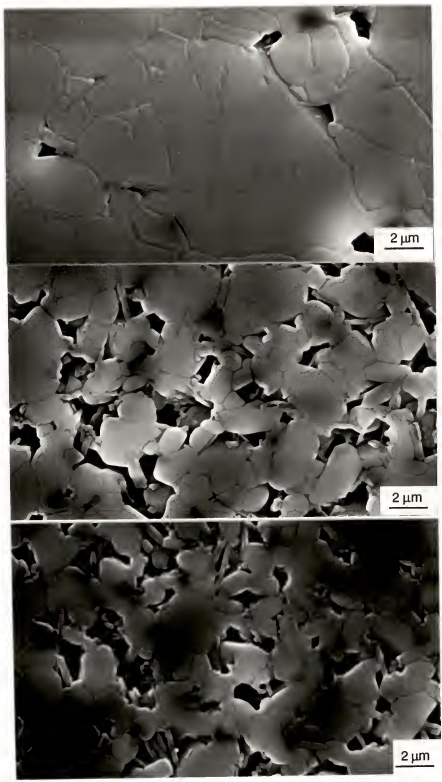

Figure 4.59 Scanning electron micrographs for the composites prepared with alumina-10 at the sintering temperature of 1700°C: (A) 5 vol%, (B) 15 vol%, and (C) 30 vol% whiskers.

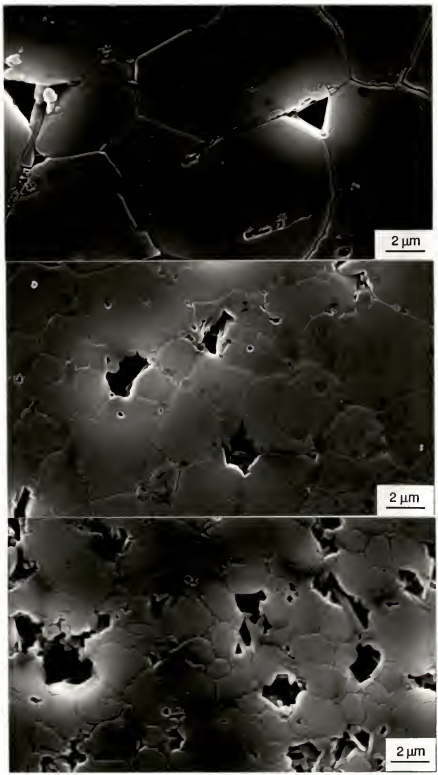

Figure 4.60 SEM micrographs for the composites prepared with alumina-10 at the sintering temperature of 1800°C: (A) 5 vol%, (B) 15 vol%, and (C) 30 vol% whiskers.

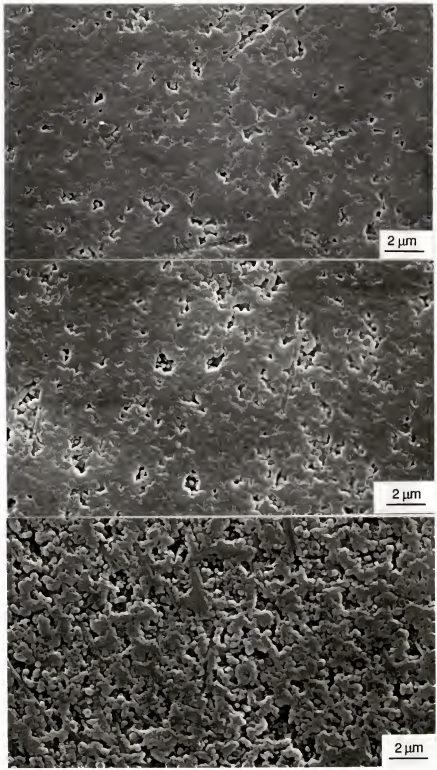

Figure 4.61 SEM micrographs for the composites prepared with alumina-27 at the sintering temperature of 1250°C: (A) 5 vol%, (B) 15 vol%, and (C) 30 vol% whiskers.

(A)

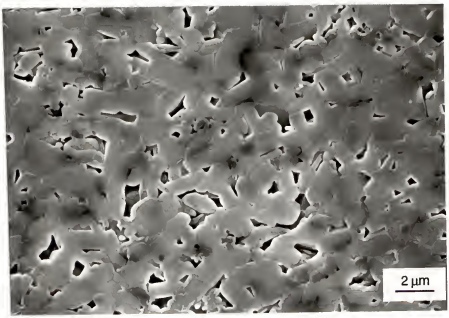

(B)

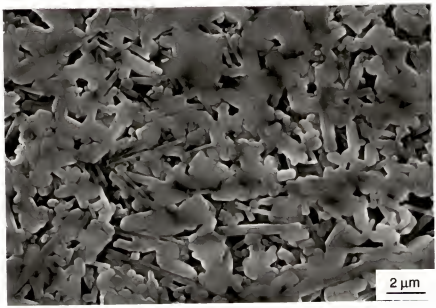

Figure 4.62 SEM micrographs for the composites prepared with alumina-27 at the sintering temperature of 1500°C: (A) 15 vol% and (B) 30 vol% whiskers.

(A)

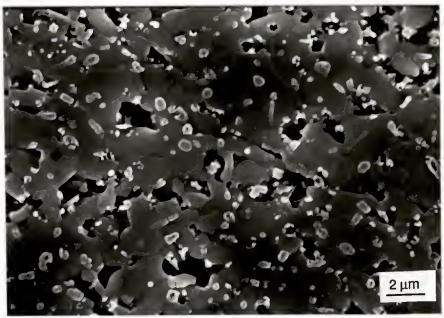

(B)

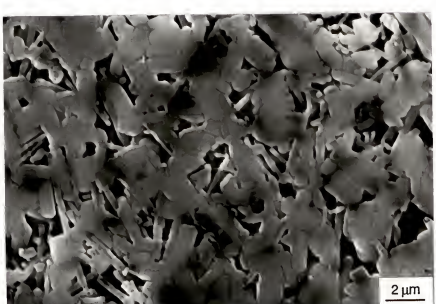

Figure 4.63 SEM micrographs for the composites prepared with alumina-27 at the sintering temperature of 1700°C: (A) 15 vol% and (B) 30 vol% whiskers.

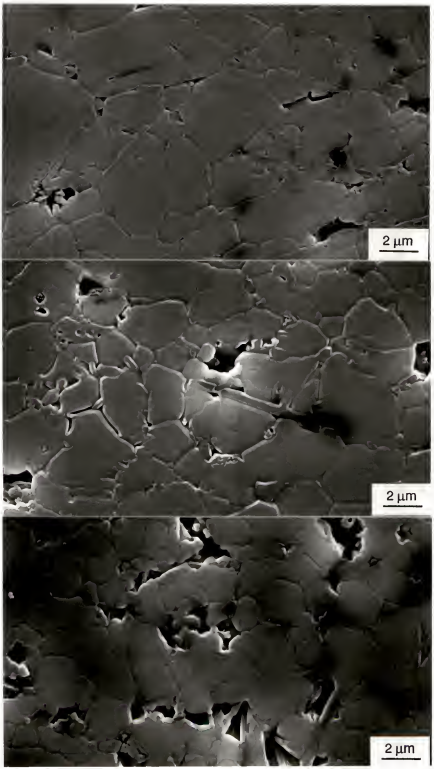

Figure 4.64 SEM micrographs for the composites prepared with alumina-27 at the sintering temperature of 1800°C: (A) 5 vol%, (B) 15 vol%, and (C) 30 vol% whiskers.

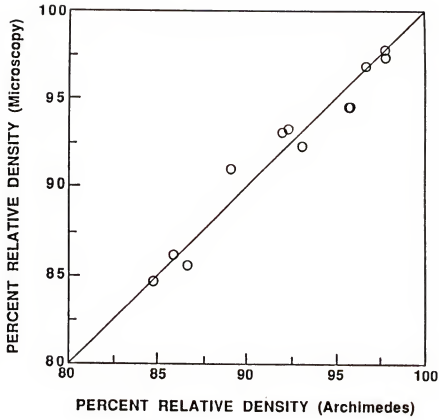

Figure 4.65 Plots showing relative density for composite samples determined by the Archimedes displacement method and quantitative microscopy measurement of the pore volume fraction. The straight line represents the ideal case where the two methods of measurement give the exact same value.

Table 4.13 Specific surface areas of 70 vol% Al_2O_3/30 vol% SiC whisker composites

Heat Treatment Temperature (°C)	Al_2O_3-10 Composite Surface Area (m^2/g)	Al_2O_3-27 Composite Surface Area (m^2/g)
700	7.2	18.4
1250	3.3	3.7
1500	1.4	1.7
1700	1.0	1.1

decreases even more rapidly for the Al_2O_3-27 composites, i.e., from ~18.4 m^2/g for a calcined compact, to ~1.1 m^2/g for a sample sintered at 1700°C. Since open porosity of these compacts decreases only slightly during sintering, the large decreases in measured specific surface area cannot be attributed to the closure of pore channels. The results are consistent with coarsening of the pore structure. This coarsening amplifies the problem of achieving high relative densities in samples containing high whisker concentrations.

The measured surface area for the calcined Al_2O_3-10 and Al_2O_3-27 composite compacts are somewhat lower than values calculated from the surface area of the starting powder and whisker for loose-stack mixtures (i.e., ~8.6 m^2/g and ~21.2 m^2/g, respectively). The values for the compacts are probably lower for two reasons. First, compacts have more particle-particle contacts which reduces the available surface area for gas adsorption. Second, even at the relatively low calcination temperature of 700°C, the finest Al_2O_3 particles may undergo slight surface rounding and neck formation via surface diffusion.

Figure 4.66 shows the average intercept size the Al_2O_3 grains as a function of sintering temperature for compacts prepared with the Al_2O_3-27 powder and various whisker concentrations. As observed in Figure 4.53 for the samples prepared with the Al_2O_3-10 powder, smaller average grain intercept sizes are measured at each sintering temperature for samples with higher whisker concentration.

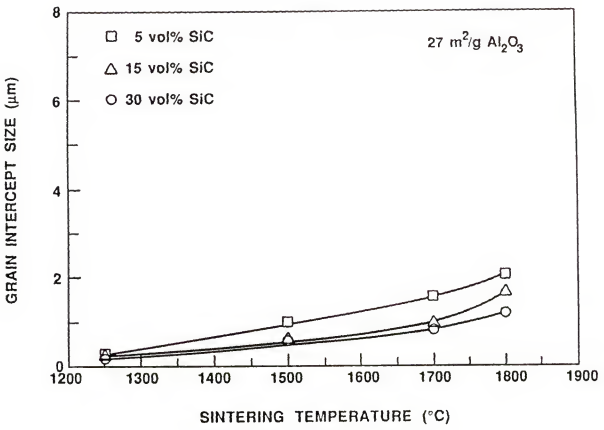

Figure 4.66 Plots of average grain intercept size vs. sintering temperature for samples prepared with varying Al_2O_3/SiC whisker ratio. Samples were prepared with the Al_2O_3-27 powder.

Comparison of Figures 4.53 and 4.66 shows that the average grain intercept sizes are larger at any given sintering temperature and Al_2O_3/SiC whisker ratio for samples prepared with the Al_2O_3-10 powder. This is not surprising considering that the starting particle size is larger for these samples. However, it is noted that the magnitude of the differences in average intercept sizes for composites prepared with the two Al_2O_3 powders is highly dependent upon the whisker concentration. For example, there is only a small difference in the average intercept sizes for Al_2O_3-10 and Al_2O_3-27 composites prepared with 30 vol% SiC whiskers and sintered in the range 1500-1800°C. This illustrates the dominant influence of the whisker network on constraining bulk densification in both composites, which in turn controls the size to which the alumina grains can grow.

As discussed earlier, an analogy can be drawn with a powder compact prepared with coarse and fine powders in which the coarse volume fraction is high enough to form a continuous network. The growth of the fine grains is constrained by the size of the interstices between the coarse particles. Furthermore, regardless of the initial particle size, the fines will grow to the same limiting grain size due to the constraints from the coarse particle network after sintering at high temperatures. For the Al_2O_3-10 and -27 composites with 30 vol% whiskers, this is illustrated not only by the similar size of the grains in sintered samples

(Figures 4.53 and 4.66), but also by the similarity in measured surface area values (Table 4.13).

In contrast to the results with 30 vol% whiskers, the composites with lower whisker contents show greater difference in average grain intercept sizes (Figures 4.53 and 4.66) because densification is constrained to different degrees. For example, the Al_2O_3-27 composites with 5 vol% whiskers sinters at only 1250°C to ~97% relative density with an average intercept size of ~0.28 μm. The Al_2O_3-10 composites densify much more slowly, so a temperature between 1700°C and 1800°C is needed to reach ~97% relative density. However, grain boundary mobilities increase rapidly with increasing temperature, so the grain growth rate is considerably higher for these samples. Thus, an Al_2O_3-10 composite with 5 vol% whiskers would develop an average grain intercept size between ~2.0 and ~5.5 μm when the density is ~97%.

The sharp increase in grain size at high temperatures for the alumina-10 composite with 5 vol% whiskers is not observed for the Al_2O_3-27 composites with 5 vol% whiskers. As noted earlier, a significant fraction of the alumina grains in the former sample grow to sizes large enough to sweep past the whisker inclusions. However, even after sintering at 1800°C, the grains in the Al_2O_3-27 samples remain small enough to be restrained by the whiskers. The average grain intercept size for the samples with 5 vol% whiskers does not increase with temperature much faster than for samples with 15 or 30 vol% whiskers (Figure 4.66). Since the Al_2O_3-27 samples with 5

vol% whiskers approach maximum sintered density at 1250°C, it is clear that there is little constraint on grain growth from pore pinning. This is consistent with earlier observations that the small concentration of whiskers provides a significant constraint on grain growth in high density samples.

4.4.5 Effect of Sintering Additives

Figure 4.67 shows the relative density as a function of SiC whisker content for the samples sintered at 1700°C and 1800°C. Sintered densities are compared for samples with and without the Y_2O_3/MgO sintering additives are compared to the samples without sintering additives. It is evident that there is a large improvement in densification of composites with sintering additives at 1700°C. For example, at 15 vol% whisker concentration the sintered relative density increased from ~78% to 93% with the additives.

At 1800°C, however, the sintering additives result in higher density only for the samples with 30 vol% whiskers. In fact, there is a decrease in density between 1700 and 1800°C for the 5 and 15 vol% SiC whisker composites prepared with the additives. This decrease in relative density for the samples with 5 and 15 vol% is probably due to bloating. (If gases become entrapped within closed pores, the internal pressure can increase significantly as sintering temperature increases. This results in pore expansion, i.e., bloating.) This is suggested by microstructure observations (Figures

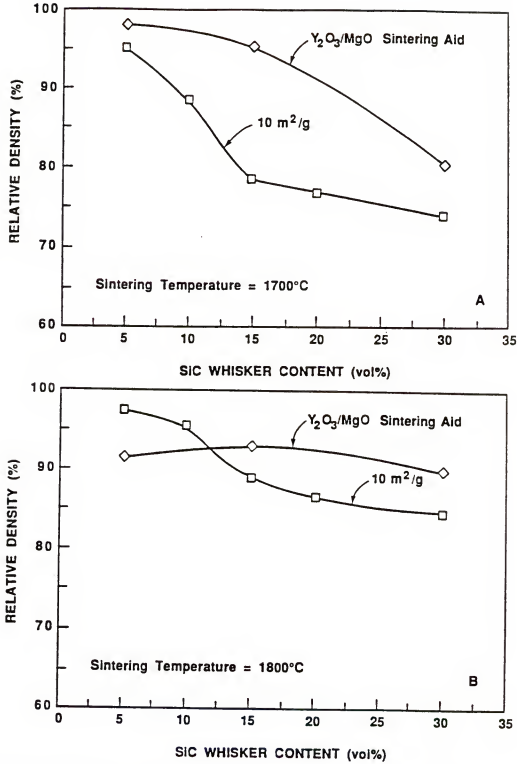

Figure 4.67 Plots of relative density vs. SiC whisker content for the samples prepared with and without sintering additives and sintered at (A) 1700 and (B) 1800°C.

4.70 and 71) which show that the size of the residual pores increases significantly as the sintering temperature increases from 1700°C to 1800°C.

In Figure 4.67, relative density values for the samples with sintering additives were determined by Archimedes displacement method. Since extensive reactions took place between constituents, the accuracy of the density values may be questioned due to the uncertainty in true density values. To confirm the accuracy of the true density values used to calculate these relative densities, independent measurements of the pore volume fraction were made using the point counting method. Figure 4.68 shows close agreement between the relative density values obtained by the two different methods.

Figure 4.69 compares the sintered relative densities achieved in this study with values reported by Tiegs and Becher [Tie87], using the same additive concentrations and similar sintering conditions. Improved densification was observed in the present study, especially at higher whisker contents. This is attributed primarily to the improved green microstructures of the suspension-processed samples. Although suspension-processed samples containing sintering additives have lower green densities and larger median pore channel radii, as compared to the samples without additives (Figure 4.34), the green relative densities are still higher compared to the dry-processed samples produced by Tiegs and Becher. In

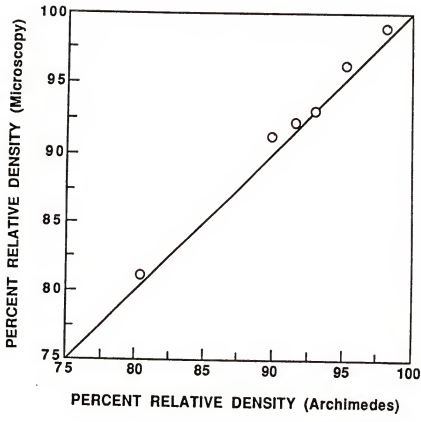

Figure 4.68 Comparison between the relative density values determined by Archimedes method and point counting. The straight line represents the ideal case.

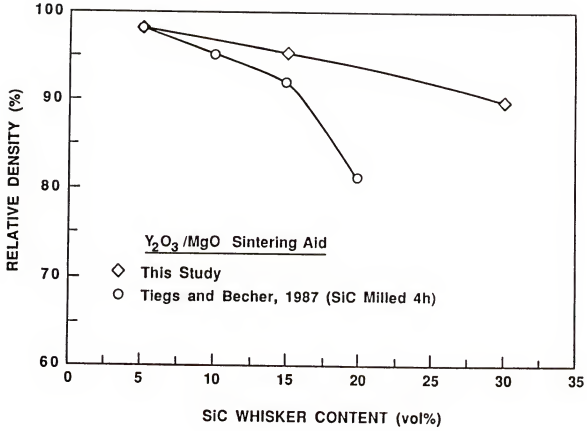

Figure 4.69 Plots of the optimum sintered density vs. SiC whisker content for samples with sintering additives. The results are compared with the results reported by Tiegs and Becher [Tie87].

addition, suspension-processed samples have more homogeneous green microstructures with finer pore sizes.

However, in comparing data from this study and Tiegs and Becher's study, it should be recognized that there may be significant differences in the physical and chemical properties of the starting powder and whisker. For example, the whiskers used by Tiegs and Becher were ball milled for 4 hrs, while the whiskers used in this study were prepared by fluid classification. Since the aspect ratio and size distribution of the whiskers affect the densification behavior of composites, some uncertainty arises in comparing the sintered densities.

The reason for the improved densification in samples with sintering additives is presumably due to the formation of liquid phases at the sintering temperature. Liquid phase could enhance particle and whisker rearrangement processes, resulting in close packing of compacts. The liquid could also result in increased material transport along grain boundaries, i.e., due to increased diffusivities. The latter mechanism may be less important in the present system, however, since the microstructure observation revealed that the phases formed during sintering are located primarily in relatively large isolated pockets (Figures 4.70 and 71).

The amount of liquid phase formed during sintering (at 1700°C) of samples with 5 vol% whiskers was crudely estimated from the amount of new phases measured in the polished microstructure (using point count method). The measured

(A)

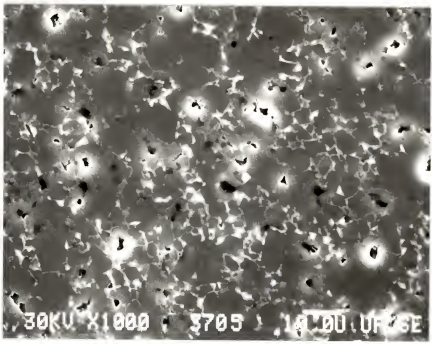

(B)

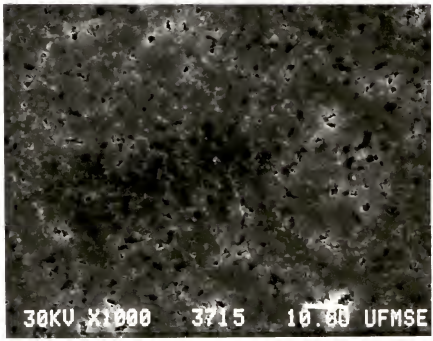

Figure 4.70 SEM micrographs of the samples with sintering additives and sintered at 1700°C with (A) 5 vol% and (B) 15 vol% whiskers.

(A)

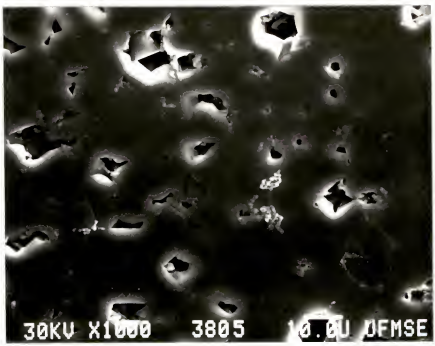

(B)

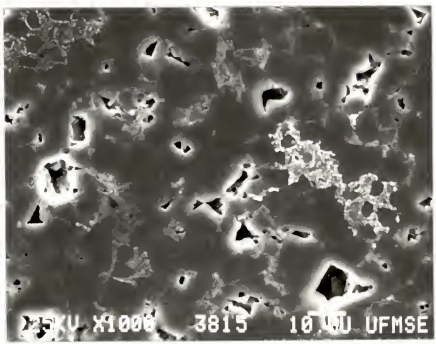

Figure 4.71 SEM micrographs of the samples with sintering additives and sintered at 1800°C with (A) 5 vol% and (B) 15 vol% whiskers.

volume fraction of new phases was 0.05. The low volume fraction of new phase is not surprising since the amount of Y_2O_3 and MgO added was small. The amount of liquid phase formed during sintering is insufficient to allow full densification in composites prepared with high volume fraction of SiC whiskers (e.g., 30 vol%). In addition to the limited amount of liquid phase, the new phases are found primarily in isolated pockets, indicating that the liquid phase(s) only partially wets the grain boundaries. This is less favorable for densification by liquid phase sintering.

Despite the low volume fraction of liquid and incomplete wetting, significant improvement in densification is observed for all whisker loading. One of the important roles of liquid phase in enhancing densification of whisker composites is presumably to provide lower shear viscosity which facilitates the stress relaxation in the matrix.

Figure 4.72 shows X-ray diffraction patterns obtained from the samples with sintering additives and sintered at 1700°C and 1800°C. They revealed that yttrium aluminum garnet (YAG; $3Y_2O_3 \cdot 5Al_2O_3$) formed. In the alumina-rich region of the Y_2O_3-Al_2O_3 equilibrium phase diagram, there is eutectic temperature at ~1760-1790°C. Therefore, in the 1700°C samples, it is possible that the YAG phase form only by solid-state reaction. However, this does not seem likely because the significant increase in the densification rate at this temperature is indicative of liquid formation. It seems plausible that other minor components in the composites may

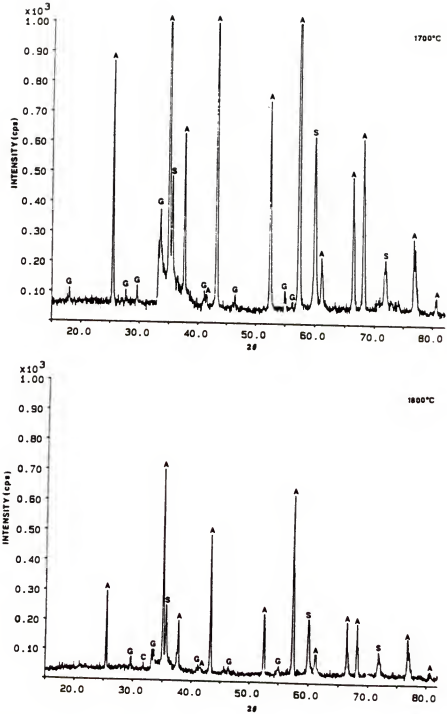

Figure 4.72 X-ray diffraction patterns for the samples with 15 vol% whiskers and sintered at (A) 1700 and (B) 1800°C (A=Al_2O_3, S=SiC, G=$3Y_2O_3 \cdot 5Al_2O_3$, C=$CaYO_4$).

have contributed to the formation of a multicomponent liquid with a lower melting temperature. The other components that may have contributed to liquid formation at lower temperatures include: (1) MgO (which was the minor component of the sintering additive), (2) silica (which formed on the surface of the whiskers during aqueous processing), and (3) calcium (which is known to be major impurity in the SiC whiskers [Ada88]). Analysis of the new phases by EDS provided evidence that a multicomponent phase formed in the 1800°C-sintered composites with 15 vol% SiC whiskers. As shown in Figure 4.73, the major elements detected in the EDS spectrum were identified as Al and Y, but smaller Ca and Si peaks were also observed. Ca was also detected by XRD analysis of the 1800°C samples as a crystalline CaY_2O_4 phase. The Ca was presumably due to the dissolution from the SiC whiskers. This phase was not observed in the samples sintered at 1700°C.

It is interesting to note that Mg was not detected by EDS in either the matrix or the precipitated new phases by EDS in the 1800°C-sintered composite samples. However, an alumina compact with sintering additives, sintered at 1630°C in air, showed $MgAl_2O_4$ peaks in XRD analysis. This suggests that most of MgO volatilized during sintering. It is well known that MgO has a high volatilization rate at elevated temperatures, especially at low oxygen partial pressures [Sat84].

One concern with using sintering additives is that high temperature mechanical properties of the composites may be

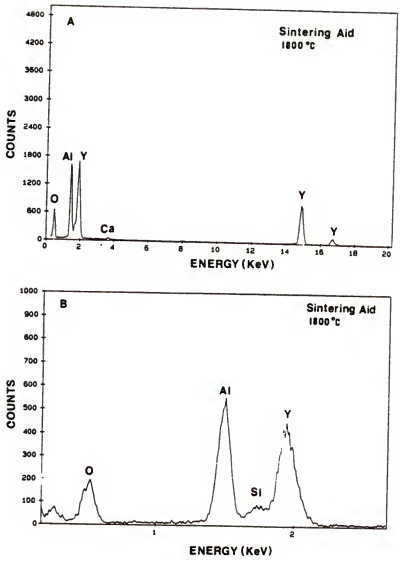

Figure 4.73 EDS spectra at different sensitivities for the 15 vol% SiC whisker composites prepared with sintering additives which were sintered at 1800°C.

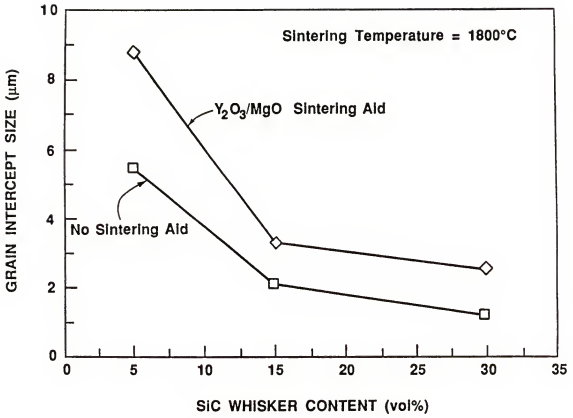

Figure 4.74 Plots of grain intercept size vs. SiC whisker content for samples prepared with and without sintering additives.

adversely affected if liquids with low-melting temperatures form under operating conditions. The samples prepared with the sintering additives also show increased grain growth during sintering, especially low whisker concentration. This is shown in Figure 4.74 for samples sintered at 1800°C. There are several possible reasons for the increase in grain size, including (1) less pinning of grain boundaries by pores due to the enhanced densification rate, and (2) increased grain boundary mobility due to enhanced diffusivities in the presence of liquid phases. Despite the large increase in grain intercept size in the composites with 5 vol% whiskers, the whiskers still provide considerable constraint on grain growth. This is evident by comparison with the grain growth of the pure alumina-10 samples without SiC whiskers. As shown in Figure 4.54, alumina samples have average grain intercept sizes of 13 and 38 μm after sintering at 1700°C and 1800°C, respectively. In contrast, the samples with sintering additives and 5 vol% whiskers have average grain intercept sizes of ~2.9 and ~8.8 μm, respectively. The samples sintered at 1700°C have similar relative densities (~98%). Therefore, the lower grain growth rate for the samples with sintering additives cannot be attributed to pinning of grain boundaries by pores.

4.4.6 Effect of Green Body Infiltration

Figure 4.75 shows the relative density as a function of SiC whisker content for infiltrated samples which were sintered at 1700°C and 1800°C, respectively. For comparison,

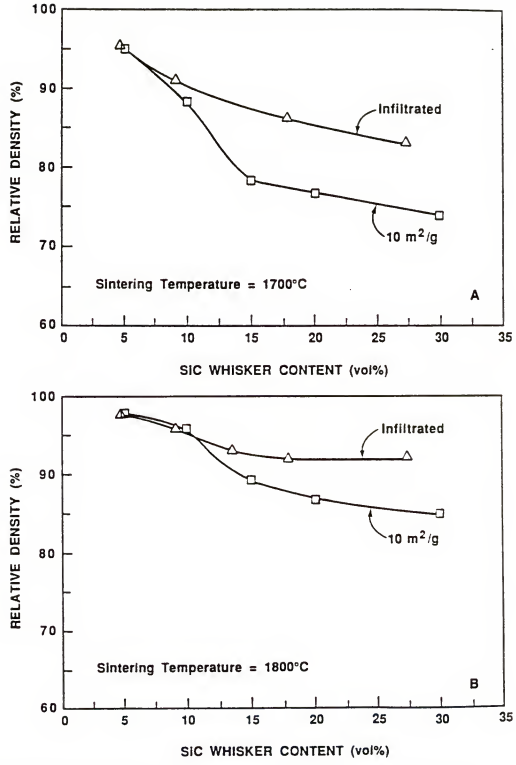

Figure 4.75 Plots of relative density vs. SiC whisker content for samples prepared with and without infiltration and sintered at (A) 1700 and (B) 1800°C.

the sintered relative densities for uninfiltrated samples are also shown in Figure 4.75. It is evident that the increase in green density due to infiltration leads to increased sintered densities, especially in samples with higher whisker concentrations. For example, the sample with ~27 vol% whiskers reached ~93% relative density after sintering at 1800°C.

The higher starting density of the infiltrated samples is beneficial for achieving high sintered densities in that less pore volume must be removed in order to reach a given sintered density. Furthermore, since less shrinkage occurs, the amount of new contacts between approaching SiC whiskers is reduced and less constraint is developed by deformation-resistant whisker networks. In addition, the measured surface area of infiltrated samples with ~27 vol% whiskers was higher (~10.2 m^2/g after heat treatment at 900°C) compared to the sample without infiltration (~7.2 m^2/g after 700°C heat treatment). The increased surface area is attributed to the fine pore sizes in the infiltrated compact and to the ultrafine infiltrant particle sizes. The higher surface area is indirect evidence that the infiltrated samples have higher sintering driving force compared to the samples without infiltration. Thus, the enhanced densification behavior of infiltrated composites is due to the combined effects of less required shrinkage and higher sintering driving force.

The relative density values in Figure 4.75 for the infiltrated samples were determined by Archimedes

displacement method. The accuracy of the true density values used to calculate these relative densities was confirmed by independent measurements of pore volume fraction using point counting method. Figure 4.76 shows that there is relatively good agreement between the relative densities obtained by the two different methods.

Since there is a large difference in starting densities between the samples with and without infiltration, sintering parameters are compared in order to exclude the green density effect on densification of composites. The sintering parameter is defined as follows:

$$\text{Sintering Parameter} = \frac{SD - GD}{TD - GD} \qquad (4.11)$$

where SD is sintered density, GD is green density, and TD is a theoretical density. As shown in Table 4.14, the sintering parameters of infiltrated samples are indeed higher at high whisker content. On the other hand, the sintering parameters of infiltrated samples are lower at lower whisker contents. Since the infiltration process alone can exceed 80% relative density for the suspension-processed samples, the infiltration processing can minimize the constraint effect of whiskers on composite densification, particularly in the early stage of sintering [Bor88b, Hsu86].

The infiltrated samples also sinter to considerably low open porosity. Figure 4.77 shows the open porosity as a function of whisker content for 1800°C-sintered samples prepared with and without infiltration. Infiltrated samples

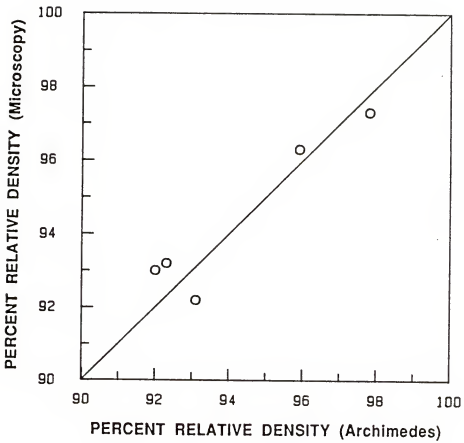

Figure 4.76 Comparison between the relative density values determined by Archimedes method and point counting. The straight line represents the ideal case where the two methods of measurement give the exact same value.

Table 4.14 Sintering parameter of the samples with and without infiltration

SiC whisker content (vol%)	Sintering parameter			
	Uninfiltrated		Infiltrated	
	1700°C	1800°C	1700°C	1800°C
5 (4.6)*	0.84	0.93	0.77	0.89
10(8.9)	0.61	0.86	0.54	0.79
15(13.4)	0.27	0.63	0.16	0.64
20(17.7)	0.23	0.56	0.29	0.58
30(27.3)	0.13	0.49	0.17	0.62

* The numbers in the parentheses are SiC whisker concentrations after infiltration.

prepared with ~27 vol% whiskers have only ~3% open porosity after sintering at 1800°C.

Figure 4.78 shows the average grain intercept size as a function of SiC whisker content for the infiltrated and uninfiltrated samples sintered at 1800°C. The average grain intercept sizes are approximately the same at each whisker concentration. This is an interesting result since infiltrated samples with >10 vol% whiskers have higher relative density and, therefore, less pores to restrain grain boundary movement. This suggests that the constraint on grain growth provided by the SiC whiskers is the dominant factor controlling the grain size.

In the presence of a second phase (i.e, whiskers), the extent of restraining force against grain growth is dependent upon the size and volume fraction of the dispersed second phase particles. According to Zener's relation [Smi48] for randomly distributed spherical inclusions, the limiting grain size given by

$$D_z = \frac{2r}{3f_v\beta} \qquad (4.12)$$

where D_z is the maximum grain size of matrix, r and f_v are the radius and the volume fraction of the second phase, respectively, and β is a numerical constant (originally assumed equal to 0.5 by Zener). Since whiskers have anisotropic geometry, two extreme cases were considered (i.e., when whiskers are aligned parallel to the moving grain boundary and when whiskers are aligned perpendicular to the

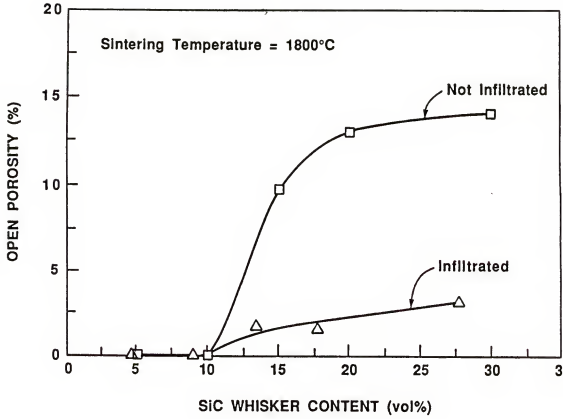

Figure 4.77 Plots of open porosity vs. SiC whisker content for samples prepared with and without infiltration and sintered at 1800°C

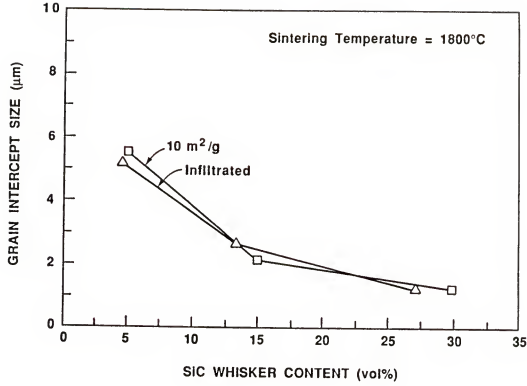

Figure 4.78 Plots of average grain intercept size vs. SiC whisker content for samples prepared with and without infiltration and sintered at 1800°C.

moving grain boundary in two dimension). By balancing pinning force and driving force of grain boundary migration, equation (4.12) is modified to $D_z = 2lr/f(l+r)\beta$ in the former case while it should be $D_z = 2\pi r^2/f\beta$ in the latter case (where l and r are whisker length and diameter, respectively). Figure 4.79 shows the experimentally measured maximum grain sizes as a function of SiC whisker content for the samples with and without infiltration which were sintered at 1800°C. The maximum grain sizes calculated by Zener's approach are also shown for two extreme whisker orientations. Surprisingly, the whiskers aligned perpendicular to moving grain boundaries are more effective in constraining grain growth, as compared to the case where the whiskers are aligned parallel to the moving grain boundary. This is due to much higher number of whiskers intersecting a grain boundary in the perpendicular orientation. The maximum measured grain sizes in all composites fall between the calculated values of two extreme cases (although values are much closer to the parallel orientation case).

Figure 4.80 shows the fracture toughness values obtained by the indentation method for the samples with and without infiltration. As expected, the fracture toughness increases significantly with the addition of SiC whiskers. The infiltrated and uninfiltrated samples showed approximately the same increases in fracture toughness with increasing whiskers. The significant increase in fracture toughness is a

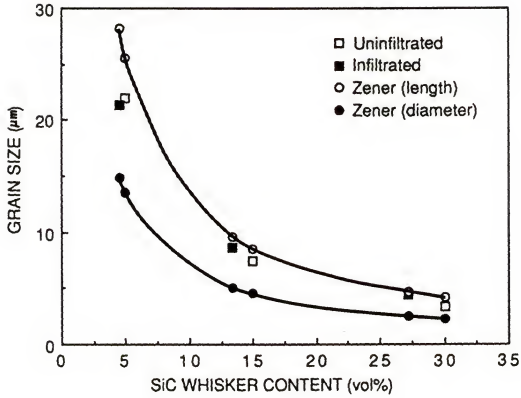

Figure 4.79 Comparison of maximum measured grain size with the predicted grain size by Zener's relation.

result of low interfacial strength which is consistent with TEM and X-ray diffraction studies which showed that no reaction between whiskers and alumina.

Even though the whisker pull-out contribution to the increase in fracture toughness is insignificant compared to and crack deflection and whisker-bridging, the whisker pull-out length has a significant meaning. This is because the whisker pull-out mechanism is the end phenomena of both crack deflection and whisker-bridging mechanisms. The whisker pull-out length is a good indicator of the interfacial properties (fracture strength and fracture toughness), e.g., the interface strength is proportional to the ratio of whisker radius to pull-out length. Figure 4.81 shows the fracture surface produced by indentation in the infiltrated sample with 18 vol% whiskers. The pull-out lengths in this sample appear to be ~1-2 μm. Therefore, the whisker radius to pull-out ratio is ~0.1-0.2, which is slightly smaller than the ratio reported by Becher et al.[Bec88b].

Measured Vickers hardness values were considerably lower than theoretical values, as shown in Figure 4.82. Hardness values decreased as SiC whisker concentration increases. This is due to higher porosity at higher whisker concentrations. Thus, the hardness values with measured porosity were calculated using equation (2.3) with constant B=7. The calculated hardness values agree well with the measured

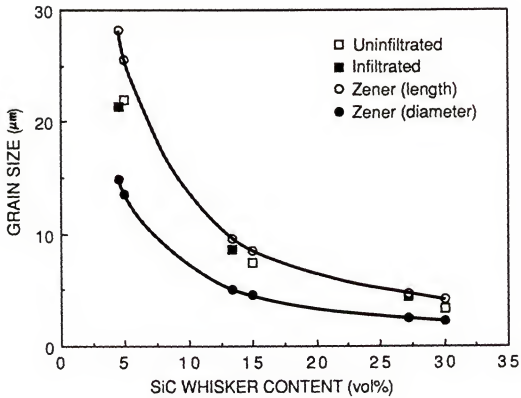

Figure 4.79 Comparison of maximum measured grain size with the predicted grain size by Zener's relation.

result of low interfacial strength which is consistent with TEM and X-ray diffraction studies which showed that no reaction between whiskers and alumina.

Even though the whisker pull-out contribution to the increase in fracture toughness is insignificant compared to and crack deflection and whisker-bridging, the whisker pull-out length has a significant meaning. This is because the whisker pull-out mechanism is the end phenomena of both crack deflection and whisker-bridging mechanisms. The whisker pull-out length is a good indicator of the interfacial properties (fracture strength and fracture toughness), e.g., the interface strength is proportional to the ratio of whisker radius to pull-out length. Figure 4.81 shows the fracture surface produced by indentation in the infiltrated sample with 18 vol% whiskers. The pull-out lengths in this sample appear to be ~1-2 μm. Therefore, the whisker radius to pull-out ratio is ~0.1-0.2, which is slightly smaller than the ratio reported by Becher et al.[Bec88b].

Measured Vickers hardness values were considerably lower than theoretical values, as shown in Figure 4.82. Hardness values decreased as SiC whisker concentration increases. This is due to higher porosity at higher whisker concentrations. Thus, the hardness values with measured porosity were calculated using equation (2.3) with constant B=7. The calculated hardness values agree well with the measured

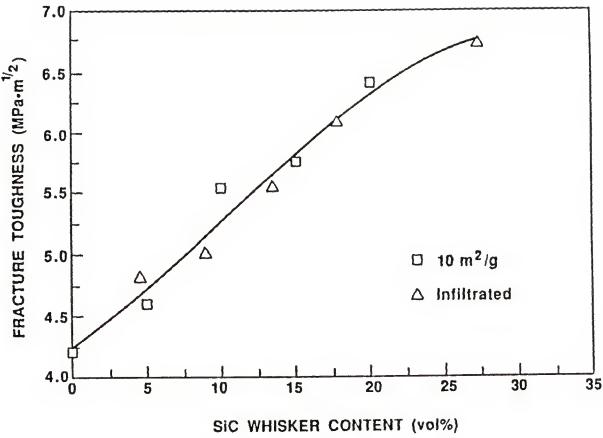

Figure 4.80 Plots of indentation fracture toughness vs. SiC whisker content for the samples prepared with and without infiltration and sintered at 1800°C.

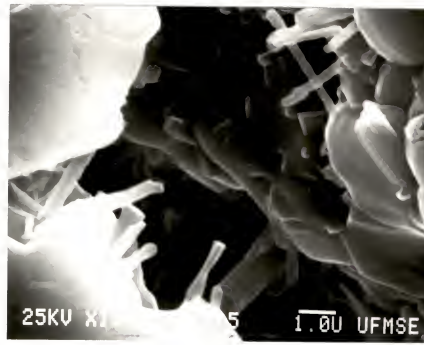

Figure 4.81 SEM micrograph showing significant whisker pull-out lengths which are an indication of low interface strength.

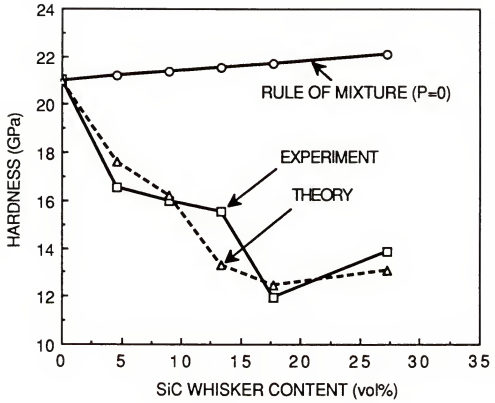

Figure 4.82 Plots of hardness vs SiC whisker content for the infiltrated samples sintered at 1800°C. Measured hardness values are compared with the theoretical prediction.

values. Since the hardness is an important property in applications (such as cutting tool, wear-resistant materials), further densification is needed to remove residual porosity. Hot-isostatic pressing along with pressureless sintering can be used in order to increase hardness since it is possible to pressureless sinter the composites to a near zero open porosity state in composites containing up to 15 vol% whiskers.

CHAPTER 5
CONCLUSIONS

1. Suspension processing was employed to prepare homogeneous Al_2O_3/SiC whisker green bodies with high relative density (~65-71%) and fine median pore size (~10-50 nm). Green microstructures were optimized by using suspensions which were well-dispersed and which contained a high solids loading. Both suspension viscosity and median pore channel radius were dependent on the characteristics of constituent powders and whiskers. At a given dispersion condition (e.g., suspension pH), green density values obtained by suspension processing were independent of the starting powder/whisker characteristics up to 30 vol% whisker concentrations.

2. Pressureless sintering was investigated for compacts with 0-30 vol% SiC whiskers. Whiskers play a dominant role in the densification of composites. Densification of compacts with lower SiC whisker concentrations was enhanced when alumina powders with finer particle size (higher surface area) were used. Samples with 15 vol% SiC whiskers could be sintered to ~97% relative density and no open porosity after sintering at 1800oC for 30 minutes. At higher SiC whisker concentrations, e.g. 30 vol%, the alumina matrix particle size had negligible effect on densification of composites. Microstructure evolution revealed that the composites with high whisker concentrations went through both extensive local

densification and coarsening (i.e., grain growth) of alumina, resulting in reduced sintering driving force and increased diffusion path length for macroscopic densification of composites.

3. Densification could be enhanced with 2 wt% Y_2O_3/0.5 wt% MgO, presumably due to the liquid phase formation at sintering temperature. However, since the sintering additives reacted with Al_2O_3 to form yttrium aluminum garnet ($3Y_2O_3 \cdot 5Al_2O_3$), samples with sintering additives may have an adverse effects on physical properties of composite (e.g., high temperature strength) depending on the location of second phases. At higher sintering temperature (1800°C), the impurities in whiskers dissolved to form low melting second phase (CaY_2O_4) which might further deteriorate the high temperature mechanical properties. At higher whisker concentrations, the use of sintering additives showed limited enhancement in composite densification.

4. An infiltration method was used to increase green density. Significant increases in sintered density were obtained, especially at higher SiC whisker concentrations. Samples with ~27 vol% SiC whiskers could be sintered to ~93% relative density with ~3% open porosity after sintering at 1800°C for 30 minutes.

5. Enhanced densification was also observed in samples prepared with lower aspect ratio due to less extensive network formation.

6. Each of the aforementioned methods was quite effective for compacts prepared with ≤15 vol% SiC whiskers. For samples with highest whisker concentrations (>15 vol%), the infiltration method was the best approach for achieving high sintered relative densities.

7. Further improvements in sintered densities might be expected if some of the above approaches are used in combination. For example, the infiltration approach can be applied to the samples prepared with finer matrix particle size or to the samples with sintering additives. Since, due to local densification and coarsening in composites, samples with high whisker contents maintain open pores to quite a high density, the infiltration approach may be applied at the stage with the largest open pore size. This approach may produce compacts with no-open-porosity state at somewhat lower bulk density. The combination of this technique with SINTER+HIP may allow the production of fully dense ceramics with complex shape.

APPENDIX

PROCEDURES FOR POWDER PREPARATION

1. Alumina-8 Powder from RCHP-DBM

   a. Prepared ~25 vol% suspensions with 400g of as-received RCHP-DBM powder, 299 g of D.I. water, and 4 ml 3N-HNO_3.
   b. Mixed with paint shaker for 5 min.
   c. Ultrasonicated for 30 min.
   d. Adjusted pH to 3.8 with 3N-HNO_3.
   e. Ultrasonicated for 30 min.
   f. Diluted into a 2.5 vol% suspension in a 1-gal plastic container.
   g. Suspensions were subjected to centrifugal field at 1600 RPM with suspension feed rate of 10 ml/sec.
   i. Overflown suspensions were collected in another plastic container, then recirculated through the same centrifugal sedimentation condition.
   j. The overflown suspensions were designated as alumina-8.

2. Alumina-19 and Alumina-27 Powders from AKP-50 powder

   a. Prepared ~25 vol% suspensions with 239 g of as-received AKP-50 powder, 240 g of D.I water, 3 ml 3N-HNO_3.
   b. Mixed with paint shaker for 5 min.
   c. Ultrasonicated for 30 min.
   d. Adjusted pH to 3.8 with 3N-HNO3.

e. Ultrasonicated for 30 min.

f. Suspension was diluted into 1.5 vol% suspension in 1-gal plastic container.

g. The diluted suspension was subjected to the centrifugal field at 4600 RPM, suspension feed rate of 1.6 ml/sec.

h. The overflown suspension was recirculated through centrifuge under the same condition.

i. The collected suspension was subjected to a higher angular speed at 4800 RPM with 1.3 ml/sec.

j. The overflown suspension was subjected to two more circulation through centrifuge at the same conditions.

k. The powder collected from the final overflown suspension was designated as alumina-27 powder.

l. The powder collected inside the centrifuge was designated as alumina-19.

3. Alumina-10 Powder

a. Concentrated the overflown alumina-8 suspension to 35 vol% solids loading by evaporation.

b. Prepared 35 vol% alumina-19 suspension with the collected powder.

c. Mixed the two 35 vol% suspensions in the weight ratio of 1:1.

d. The mixed suspension was concentrated to 50 vol% solids loading and ultrasonicated.

e. The powder in the mixed suspension was designated as alumina-10.

4. Washing of Whiskers

   a. Prepared 2 vol% SiC whisker suspensions in a 1 gal plastic container with 70 g SiC whisker, 54.2 ml 3N NH_4OH, and 1000 ml D.I. water.

   b. Aged for 12 hr with continuously rotating the container in a mill.

   c. Filtered the suspension, then washed with D.I. water 6 times until constant ionic conductivity is reached.

   d. Repeated steps (a-c).

   e. Prepared ~2 vol% suspension in a 1 gal plastic container with the whiskers (recovered from base washing), 6.5 ml 3N HNO_3, and 1050 ml D.I. water.

   f. Aged for 12 hr as in base wash, filtered, then washed.

   g. Repeated the steps e and f.

   h. After washing with D.I. water, the recovered powder was dried at 50°C for 48 hr.

5. Preparation of TSC-A, -B, and -C Whiskers

   a. Prepared ~5 vol% SiC whisker suspensions with washed whiskers (from procedure 5) at pH~10.5.

   b. Sonicated for 30 min.

   c. Diluted to ~0.5 vol% in 1 gal plastic container.

   d. The suspension was subjected to centrifugal field at 350 RPM and with suspension feed rate of 8.5 ml/sec.

   e. The sediment cake was redispersed and classified by gravity sedimentation in order to remove whiskers < 1

μm. The settled whisker suspension was recovered, filtered, then washed 6 times with D.I. water. This was designated TAT-A.

f. The overflown suspension in step d was subjected to centrifugal field at 800 RPM and with suspension feed rate of 2.5 ml/sec.

g. The sediment cake was redispersed and classified by gravity sedimentation in order to remove whiskers < 1 μm. The settled whisker suspension was recovered, filtered, then washed 6 times with D.I.water. This was designated TAT-B.

h. The overflown suspension in step g was combined with the suspension with whiskers < 1 μm from steps e and g. The combined suspension was filtered, then washed 6 times with D.I. water. This was designated TAT-C.

i. The fractionated whiskers were dried at 50°C for 48 hr and stored for later use.

6. Preparation of ASC-F and TSC-F Whiskers

a. Prepared 5 vol% SiC whisker suspension with 32 g whiskers and 200 g D.I water at pH~10.5.

b. Sonicated for 30 min at output=6.

c. Diluted to ~1 vol% to make 1000 ml.

d. Settled for the time when the whiskers of equivalent spherical diameter of 10 mm can reach 1/3 of total height.

e. Withdrew the 2/3 of suspension

f. Redispersed the remaining suspension at pH~10.5

g. Settled in the same manner as in step d.

h. Repeated the gravity sedimentation 5 times total.

i. The withdrawn suspensions were combined, filtered, and washed 6 times with D.I. water.

j. Whiskers were dried at 50°C for 48 hr.

Note that fine SiC particles/whiskers were removed from ASC-F whiskers. This was accomplished by removing supernatant after centrifugation of ~1 vol% whisker suspension at 2800 RPM. The particle size distributions obtained by X-ray sedigraph are shown in Figure A-1 (alumina) and A-2 (SiC whiskers).

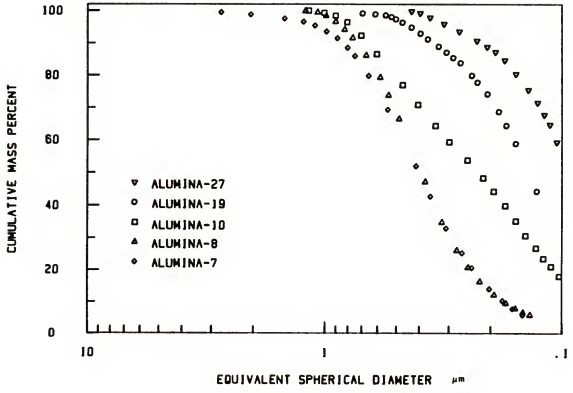

Figure A-1 Particle size distribution plots for various alumina obtained by X-ray sedigraph.

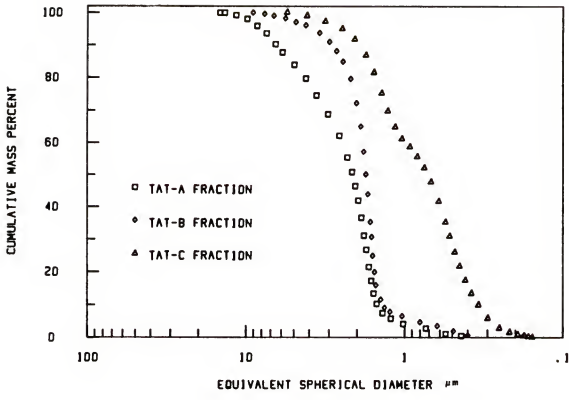

Figure A-2 Particle size distribution for SiC whiskers obtained by X-ray sedigraph.

REFERENCES

[Ada88] J.H. Adair, B.C. Mutsuddy, and E.J. Drauglis, "Stabilization of Silicon Carbide Whisker Suspensions: I, Influence of Surface Oxidation Aqueous Suspensions," Adv. Ceram. Mat., 3 [3] 231-34 (1988).

[Aks84] I.A. Aksay and C.H. Schilling, "Colloidal Filtration Route to Uniform Microstructure"; pp 439-447 in Ultrastructure Processing of Ceramics,Glasses, and Composites, Edited by L.L. Hench and D.R. Ulrich, John Wiley and Sons Inc., New York, 1984.

[Ang86] P. Angelini, P.F. Becher, and W. Mader, "Strain and Fracture in Whisker Reinforced Ceramics"; pp 241-57 in Materials Research Society Symposium Proceedings, Vol.78, Advanced Structural Ceramics, Edited by P.F. Becher, M.V. Swain, and S.Somiya, Materials Research Society, Pittsburgh, PA. 1988.

[Aok87] M. Aoki, T.A. Ring, and J.S. Haggerty, "Analysis and Modeling of the Ultrasonic Dispersion Technique," Adv. Ceram. Mat., 2 [3A] 209-12 (1987).

[Bae76] C.F. Baes and R.E. Mesmer, The Hydrolysis of Cations, John Wiley and Sons, Inc., New York, 1976.

[Bal84] I. Balberg, C.H. Anderson, S. Alexander, and N. Wagner, "Excluded Volume and Its Relation to the Onset of Percolation," Phys. Rev. B, 30 [7] 3799-43 (1984).

[Bar82] E.A. Barringer and H.K. Bowen, "Formation, Packing, and Sintering of Monodisperse TiO_2 Powders," J. Am. Ceram. Soc., 65 [12] C-199-C-201 (1982).

[Bar87] S.J. Barclay, J.R. Fox, and H.K. Bowen, "Processing of Pressureless-Sintered SiC Whisker-Reinforced Al_2O_3 Composites," J. Mat. Sci., 22, 4403-4406 (1987).

[Bec88] P.F. Becher, C.-H. Hsueh, P. Angelini, and T.N. Tiegs, "Toughening Behavior in Whisker-Reinforced Ceramic Matrix Composites," J. Am. Ceram. Soc., 71 [12] 1050-61 (1988).

[Bech87] P.F. Becher and T.N. Tiegs, "Toughening Behavior Involving Multiple Mechanisms: Whisker Reinforcement and Zirconia Toughening," J. Am. Ceram. Soc., 70 [9] 651-54 (1987).

[Bech88] P.F. Becher and T.N. Tiegs, "Temperature Dependence of Strengthening by Whisker Reinforcement: SiC Whisker-Reinforced Alumina in Air," Adv. Ceram. Mat., 3 [2] 148-53 (1988).

[Beche86] P.F. Becher, T.N. Tiegs, J.C. Ogle, and W.H. Warwick, "Toughening of Ceramics by Whisker Reinforcement"; pp 61-73 in Fracture Mechanics of Ceramics, Vol. 7, Edited by R.C. Bradt, A.G. Evans, D.P.H. Hasselman, and F.F. Lange, Plenum Publishing, New York, 1986.

[Becher84] P.F. Becher,and G.C. Wei, "Toughening Behavior in SiC-Whisker-Reinforced Alumina," J. Am. Ceram. Soc., 67 [12]C-267-69 (1984).

[Bhe85] V. Bheemineni and D.W. Readey, "Vaporization of Magnesium Oxide in Hydrogen,"; pp. 553-561 in Structure and Properties of MgO and Al_2O_3 Ceramics. Edited by W.D. Kingery. Advances in Ceramics, Vol. 10, Am. Ceram. Soc., Columbus. OH., 1985

[Boi83] J. Boissonade, F. Barreau, and Carmona, "The Percolation of Fibers with Random Orientations: A Monte Carlo Study," J. Phys., 16 2777-87 (1983).

[Bor86] R.K. Bordia and R. Raj, "Analysis of Sintering of a Composite with a Glass or Ceramic Matrix," J. Am. Ceram. Soc., 69 [3] C-55-C-57 (1986).

[Bor88a] R.K. Bordia and G.W. Scherer, "On Constrained Sintering-I. Constitutive Model For a Sintering Body," Acta Metall., 36 [9] 2393-2397 (1988).

[Bor88b] R.K. Bordia and G.W. Scherer, "On Constrained Sintering-II. Comparison of Constitutive Models," Acta Metall., 36 [9] 2399-2409 (1988).

[Bor88c] R.K. Bordia and G.W. Scherer, "On Constrained Sintering-III. Rigid Inclusions," Acta Metall., 36 [9] 2411-16 (1988).

[Bre82] J.J. Brennan and K.M. Prewo, "Silicon Carbide Fibre Reinforced Glass-Ceramic Matrix Composites Exhibiting High Strength and Toughness," J. Mat. Sci., 17, 2371-2383 (1982).

[Bro65] J.G. Brodnyan, E.L. Kelley, "The Effect of Electrolyte Content of Synthetic Latex Flow Behavior," J. Colloid Sci., 20, 7-19 (1965).

[Bro88a] R.J. Brook, W.H. Tuan, and L.A. Xue, "Critical Issues and Future Directions in Sintering Science"; pp 811-823 in Ceramic Transactions Vol.1, Ceramic Powder Science II, Part B, The American Ceramic Society, Westerville, Ohio, 1988.

[Bro88b] R.J. Brook, W.H. Tuan, and L.A. Xue, unpublished work (1988).

[Bru62] C.A. Bruch, "Sintering Kinetics for the High Density Alumina Process," Am. Ceram. Soc. Bull., 42 [12] 799-806 (1962).

[Bul87a] S.T. Buljan, J.G. Baldoni , and M.L. Huckabee , "Si_3N_4-SiC Composites," Am. Ceram. Soc. Bull., 66 [2] 347-52 (1987).

[Bul87b] S.T. Buljan and V.K. Sarin, "Silicon Nitride-Based Composites," Composites, 18 [2], 99-106 (1987).

[Bur57] J.E. Burke, "The Role of Grain Boundaries During Sintering," J. Am. Ceram. Soc., 40, 80-85 (1957).

[Cap87] A.J. Caputo, D.P. Stinton, R.A. Lowden, and T.M. Besmann, "Fiber-Reinforced SiC Composites with Improved Mechanical Properties," Am. Ceram. Soc. Bull., 66 [2] 368-72 (1987).

[Cha85] M.W. Chase, Jr., C.A. Davies, J.R. Downey, Jr., D.J. Frurip, R.A. McDonald, and A.N. Syverud, JANAF Thermochemical Tables, 3rd ed., J. Phys. Chem. Ref. Data, 14, Suppl. No.1, NBS, 1985.

[Cho85] A.H. Chokshi and T.R. Porter, "Creep Deformation of an Alumina Matrix Composite Reinforced with

Silicon Carbode Whiskers," J. Am. Ceram. Soc., 68[6] C-144-C-145 (1985).

[Cim83] R.R. Ciminelli, M.S. Thesis, The Pennsyvania State University, 1983.

[Cla86] N. Claussen and G. Petzow, "Whisker-Reinforced Zirconia-Toughened Ceramics"; pp 649-62 in Tailoring Multiphase and Composite Ceramics. Edited by R. Tressler, G. Messing, C. Pantano, and R. Newnham. Plenum Publishing Corp., New York, 1986.

[Cob59] R.L. Coble, "Diffusion Sintering in the Solid State"; pp. 147-163 in Kinetics of High-Temperature Processes. Edited by W.D. Kingery. Technology Press of M.I.T., Cambridge, and John Wiley & Sons, Inc., New York, 1959.

[Cob63] R.L. Coble, "A Model for Boundary Diffusion Controlled Creep in Polycrystalline Materials," J. App. Phys., 34 [6] 1679-82 (1963).

[Cob70] R.L. Coble, "Diffusion Models for Hot Pressing with Surface Energy and Pressure Effects as Driving Forces," J. Appl. Phys., 41 [12] 4798-4807 (1970).

[Con60] B.E. Conway and A. Dobry-Duclaux, " Viscosity of Suspensions of Electrically Charged Particles and Solutions of Polymeric Electrolytes"; pp. 83-120 in Rheology: Theory and Applications, Vol. 3. Edited by F.R. Eirich. Academic Press, New York, 1960.

[Dav68] B.W. Davidge and T.J. Green, "The Strength of Two-Phase Ceramic/Glass Materials," J. Mat. Sci., 3, 629-34 (1968).

[Dav87] R.W. Davidge, "Fiber-Reinforced Ceramics," Composites (International J. of Composite Materials), 18 [2] 93-98 (1987).

[DeJ88] L.C. DeJonghe and M.N. Rahaman, "Sintering Stress of Homogeneous and Heterogeneous Powder Compacts," Acta Metall., 36 [1] 223-29 (1988).

[Duc53] W. Duckworth, "Discussion of Ryshkewitch Paper," J. Am. Ceram. Soc., 36 [2], 68 (1953).

[Dyn84] F.W. Dynys and J.W. Halloran, "Influence of Aggregates on Sintering," J. Am. Ceram. Soc., 67 [9] 596-601 (1984).

[Ere70] V.N. Eremenko, Yu. V. Naidich, and I.A. Lavrinenko, Liquid Phase Sintering, Consultants Bureau, New York, 1970.

[Esh57] J.D. Eshelby, "The Determination of the Elastic Field of an Ellipsoidal Inclusion, and Related Problems, Proc. Roy. Soc. London, 241, 376-396 (1957).

[Eva76] A.G. Evans and E.A. Charles, "Fracture Toughness Determinations by Indentation," J. Am Ceram. Soc., 59 [7-8], 371-2 (1976).

[Evan70] A.G. Evans and R.W. Davidge, "The Strength and Oxidation of Reaction Sintered Silicon Nitride," J. Mat. Sci., 5, 314-25 (1970).

[Evan84] A.G. Evans and K.T. Faber, J. Am. Ceram. Soc., 67, 255 (1984).

[Evan88] A.G. Evans and D.B. Marshall, "The Mechanical Performance of Fiber Reinforced Ceramic Matrix Composites," pp 213-46 in HighTemperature/High Performance Composites. Edited by F.D. Lemkey, S.G. Fishman, A.G. Evans, and J.R.Strife. Mat. Res. Soc. Symp. Proc. Vol. 120, MRS, Pittsburgh, PA, 1988.

[Evans82] A.G. Evans, D.B. Marshall, and N.H. Burlingame, pp 202-16 in Advances in Ceramics, Vol. 3, Edited by A.H. Heuer and L.W. Hobbs, Am. Ceram. Soc., Columbus, Ohio, 1982.

[Evans86] A.G. Evans, M. Ruhle, B.J. Dalgleish, and M.D. Thouless, "On Prevalent Whisker Toughening Mechanisms in Ceramics"; pp. 259-71 in Materials Research Society Symposium Proceedings, Vol.78, Advanced Structural Ceramics. Edited by P.F. Becher, M.V. Swain, and S. Somiya. Materials Research Society, Pittsburgh, PA, 1986.

[Fab83] K.T. Faber and A.G. Evans, "Crack Deflection Processes-I. Theory," Acta Met., 34, 565-584 (1983).

[Far88] S.C. Farmer, P. Pirouz, and A.H. Heuer, "Microstructural Characterization of a SiC Whisker-Reinforced Hipped Reaction-Bonded Si_3N_4"; pp 169-74 in High Temperature/High Performance Composites. Mat. Res. Soc. Symp. Proc., Vol 120, Edited by F.D. Lemkey, S.G.

Fishman, A.G. Evans, and J.R. Strife. MRS, Pittsburgh, PA, 1988.

[Fit74] E. Fitzer and R. Ebi, "Kinetic Studies on the Oxidation of Silicon Carbise"; pp. 320-28 in Silicon Carbide. Edited by R.C. Marshall. University of South Carolina Press, Columbia, SC, 1974.

[Fou80] A.S. Foust, L.A. Wenzel, C.W. Clump, L. Maus, and L.B. Anderson, Principles of Unit Operations, 2nd Edition. John Wiley & Sons, New York, 1980.

[Gac84] F.D. Gac, J.V. Milewski, J.J. Petrovic, and P.D. Shalek, "Silicon Carbide Whisker Reinforced Glasses and Ceramics": presented at the Conference on Composite Materials, Cocoa Beach, FL, January 20, 1984.

[Gad86] K.P. Gadkaree and K. Chyung , "Silicon Carbide-Whisker Reinforced Glass and Glass-Ceramic Composites," Am. Ceram. Soc. Bull., 65 [2] 370-76 (1986).

[Gla87] S.J. Glass and D.J. Green, "Surface Modification of Ceramics by Partial Infiltration," Adv. Ceram. Mat., 2 [2] 129-31 (1987).

[Gla88] S.J. Glass and D.J. Green, "Fabrication of Multiphase Particulate Ceramics by Infiltration into Powder Compacts"; pp. 784-91 in Ceramic Transactions, Vol.1, Ceramic Powder Science. Edited by G.L. Messing, E.R. Fuller. Jr., H. Hausner. The American Ceramic Society, Westerville, OH, 1988.

[Goo33] J.N. Goodier, "Concentration of Stress Around Spherical and Cylindrical Inclusions and Flaws," J. App. Mech., 1, 39 (1933).

[Goo62] J. Goodison and J. White, "The Sintering of Mixed Powders"; pp. 251-270 in Agglomeration. Edited by W.A. Knepper. Interscience Publishers, New York, 1962.

[Gre73] R.A. Gregg and F.N. Rhines, "Surface Tension and the Sintering Force in Copper," Metall. Trans., 4 [5] 1365-74 (1973).

[Han89] C.A. Handwerker, P.A. Morris, and R.L. Coble, "Effects of Chemical Inhomogeneities on Grain

Growth and Microstructure in Al_2O_3," J. Am. Ceram. Soc., 72 [1] 130-136 (1989).

[Hay86] R. Hayami, K. Ueno, I. Kondou and Y. Toibana, "Si_3N_4-SiC Whisker Composite Material"; pp 663-674 in Tailoring Multiphase and Composite Ceramics. Edited by R. Tressler, G. Messing, C. Pantano, and R. Newnham. Plenum Publishing Corp. New York, 1986.

[Her50a] C. Herring, "Effect of Change of Scale on Sintering Phenomena," J. Appl. Phys., 21 [4] 301-303 (1950).

[Her50b] C. Herring, "Diffusional Viscosity of a Polycrystalline Solid," J. App. Phys., 21 [5] 437-45 (1950).

[Her86] M.A. Herron and S.H. Risbud, "Characterization of SiC-Fiber-Reinforced Ba-Si-Al-O-N Glass-Ceramic Composites," Am. Ceram. Soc. Bull., 65 [2] 342-46 (1986).

[Hie77] P.C. Hiemenez, Principles of Colloid and Surface Chemistry. Marcel Dekker, New York, 1977.

[Hil80] W.B. Hillig, R.L. Mehan, and C.R. Morelock, Ceram. Eng. Sci. Proc., 1 [7-8] 405 (1980).

[Hof89] M.J. Hoffmann, A. Nagel, P. Greil, and G. Petzow, "Slip Casting of SiC-Whisker-Reinforced Si_3N_4," J. Am. Ceram. Soc., 72 [5] 765-69 (1989).

[Hol89] E.A. Holm and M.J. Cima, "Two-Dimensional Whisker Percolation in Ceramic Matrix-Ceramic Whisker Composites," J. Am. Ceram. Soc., 72[2] 303-305 (1989).

[Hom87] J. Homeny, W.L. Vaughn, and M.K. Ferber, "Processing and Mechanical Properties of SiC-Whisker-Al_2O_3 Composites," Am. Ceram. Soc. Bull., 67 [2] 233-38 (1987).

[Hsu86] C.H. Hsueh, A.G. Evans, R.M. Cannon, and R.J. Brook, "Viscoelastic Stresses and Sintering Damages in Heterogeneous Compacts," Acta Metall., 34 [5] 927-36 (1986).

[Hun81] R.J. Hunter, Zeta Potential in Colloid Science. Academic Press, New York, 1981.

[Hun87] R.J. Hunter, Foundations of Colloid Science, Vol. 1. Claredon, New York, 1987.

[Hup75] W.J. Huppmann and H. Riegger, "Modelling of Rearrangement Processes in Liquid Phase Sintering," Acta Metall., 23, 965-71 (1975).

[Ish88] T. Ishii and H.K. Bowen, "Dispersion and Pressureless Sintering of Al_2O_3-SiC Whisker Composites"; pp 452-459 in Ceramic Transactions, Vol. 1, Ceramic Powder Science Part A. Edited by G.L. Messing, E.R. Fuller, and H. Hausner. Am. Ceram. Soc. Inc., Westerville, OH, 1988.

[Kay87] W.A. Kaysser, M. Sprissler, C.A. Handwerker, and J.E. Blendell, "Effects of a Liquid Phase on the Morphology of Grain Growth in Alumina," J. Am. Ceram. Soc., 70 [5] 339-43 (1987).

[Kel73] A. Kelly, pp. 157-226 in Strong Solids. Claredon Press, Oxford, England, 1973.

[Ken86] K. Kendall, N. McN. Alford, and J.D. Birchall, "The Strength of Fibers in All Ceramic Composites"; pp 181-87 in Materials Research Society Symposium Proceedings, Vol.78, Advanced Structural Ceramics. Edited by P.F. Becher, M.V. Swain, and S.Somiya. Materials Research Society, Pittsburgh, PA, 1986.

[Kha88] C. Khadilkar, "The Effect of Adsorbed Poly (Vinyl Alcohol) on the Properties of Model Silica Suspensions," Ph.D. Dissertation, University of Florida (1988).

[Kin59] W.D. Kingery, "Densification during Sintering in the Presence of a Liquid Phase. I. Theory," J. App. Phys., 10 [3] 301-6 (1959).

[Kin67] W.D. Kingery and B. Francois, "The Sintering of Crystalline Oxides, I. Interactions between Grain Boundaries and Pores," pp. 471-498 in Sintering and Related Phenomena, edited by C. Kuczinski, Plennum Press, New York, 1967.

[Kir76] H.P. Kirchner,R.M. Gruver and W.A. Sotter, "Characteristics of Flaws at Fracture Origin and Fracture Stress-Flaw Size Relations in Various Ceramics," Mat. Sci. Eng., 22, 147-56 (1976).

[Kit81] T. Kitano and T. Kataoka, " The Rheology of Suspensions of Vinylon Fibers in Polymer Liquids. I. Suspensions in Silicone Oil," Rheol. Acta, 20, 390-402 (1981).

[Kri72] I.M. Krieger, "Rheology of Monodisperse Lattices," Adv. Colloid Interface Sci., 3, 111-36 (1972).

[Kri81] V.V. Kristie and P.S. Nicholson, "Toughening of Glasses by Metallic Particles," J. Am. Ceram. Soc., 64 [9] 499-504 (1981).

[Kuk73] V.N. Kuklina, "Phase Composition and Particle Size of Decomposition Products of Aluminum Nitrate Nonahydrate," Kinetics and Catalysis, 4 [3], 626 (1973).

[Lam86] P.J. Lamicq, G.A. Bernhart, M.M. Dauchier, and J.G. Mace, "SiC/SiC Composite Ceramics," Am. Ceram. Soc. Bull., 65 [2] 336-38 (1986).

[Lan83] F.F. Lange,"Processing-Related Fracture Origin: I. Observations in Sintered and Isostatically Hot-Pressed Al_2O_3/ZrO_2 Composites," J. Am. Ceram. Soc., 66 396-98 (1983).

[Lan87] F.F. Lange, "Constrained Network Model for Predicting Densification Behavior of Composite Powders," J. Mat. Res., 2 [1] 59-65 (1987).

[Lang83a] F.F Lange and M. Metcalf, "Processing-Related Fracture Origins: II, Agglomerate Motion and Crack-like Internal Surfaces Caused by Differential Sintering," J. Am. Ceram. Soc., 66 [6] 398-406 (1983).

[Lang83b] F.F. Lange, B.I. David, and I.A. Aksay, "Processing-Related Fracture Origins: III, Differential Sintering of ZrO2 Agglomerates in Al_2O_3/ZrO_2 Composites, Ibid., 66 [6] 407-408 (1983).

[Lev70] A.P. Levitt, Whisker Technology. Wiley-Interscience, New York, 1970.

[Lip88] P. Lipetzky, S.R. Nutt, and P.F. Becher, "Creep Behavior of an Al_2O_3-SiC Composite,"; pp. 271-77 in High Temperature/High Performance Composites. Edited by F.D. Lemkey, S.G. Fishman, A.G. Evans, and J.R. Strife. Mat. Res. Soc. Symp. Vol 120, MRS, Pittsburgh, PA, 1988

[Lun87] R.L. Lundberg, K. Kahlman, R. Pompe, and R. Carlsson, "SiC-Whisker-Reinforced Si_3N_4 Composites," Am. Ceram. Soc. Bull., 66 [2] 330-33 (1987).

[Lut88] K.L. Luthra, "Chemical Interactions in High-Temperature Ceramic Composites," J. Am. Ceram. Soc., 71 [12] 1114-20 (1988).

[Mah84] T. Mah, N.L. Hecht, D.E. McCullum, J.R. Hoenigman, H.M. Kim, A.P. Katz, H.A. Lipsitt, "Thermal Stability of SiC Fibers," J. Mat. Sci, 19, 1191-1201 (1984).

[Mah85] T. Mah, M.G. Mendiratta, A.P. Katz, R. Ruh, and K.S. Mazdiyasni, "Room-Temperature Mechanical Behavior of Fiber-Reinforced Ceramic-Matrix Composites," J. Am. Ceram. Soc., 68 [1] C-27-C-30 (1985).

[Mar83] D.B. Marshall, A.G. Evans, and M. Drory, pp 289-307 in Fracture Mechanics of Ceramics, Vol. 6. Edited by R.C. Bradt, A.G. Evans, D.P.H. Hasselman, and F.F. Lange. Plenum Press, New York, 1983.

[Mar86] R.A. Marra and D.J. Bray, "Thermochemical Characterization of SiC Whiskers in Al_2O_3 Matrices," Cer. Eng. Sci. Proc., 7 [7-8] 945-46 (1986).

[Mil78] J.V. Milewski, "The Combined Packing of Rods and Spheres in Reinforcing Plastics," Ind. Eng. Chem. Prod. Res. Dev., 17[4] 363-66 (1978).

[Mil86] J.V. Milewski, "Efficient Use of Whiskers in the Reinforcement of Ceramics," Adv. Ceram. Mat., 1 [1] 36-41 (1986).

[Nic88] K.G. Nickel, M.J. Hoffman, P. Greil, and G. Petzow, "Thermo-dynamic Calculations for the Formation of SiC-Whisker-Reinforced Si_3N_4 Ceramics," Adv. Ceram. Mat., 3 [6] 557-62 (1988).

[Occ84] M. A. Occhinero and J.W. Halloran, "The Influence of Green Density Upon Sintering," Mat. Sci. Res., 16, 89-102 (1984).

[Ono77a] G.Y. Onoda, Jr., "Green Body Characterizations and Their Relationship to Finished

Microstructure"; pp. 163-83 in Ceramic Microstructures '76. Edited by R.M. Fulrath and J.A. Pask. Westview Press, Boulder, CO, 1977.

[Ono77b] G.Y. Onoda, Jr. and G.L. Messing, "Packing and Sintering Relations for Binary Powders"; pp. 99-112 in Processing of Crystalline Ceramics, Vol. 11, Materials Science Research. Edited by H. Palmour III, R.F. Davis, and T.M. Hare. Plenum Press, New York, 1977.

[Ott87] R.H. Ottewill, "Properties of Concentrated Dispersions"; pp. 183-198 in Solid/Liquid Dispersions. Edited by Th.F. Tadros. Academic Press, New York, 1987.

[Par84] H.-H. Park, S.-J. Cho, and D.N. Yoon, "Pore Filling Process in Liquid Phase Sintering," Metall. Trans. A, 15A, 1075-80 (1984).

[Pas84] A.E. Pasto, "Causes and Effects of Fe-Bearing Inclusions in Sintered Si_3N_4," J. Am. Ceram. Soc., 67, C-178-C-180 (1984).

[Pet82] G. Petzow, W.A. Kaysser, and M. Amtenbrink, "Liquid Phase and Activated Sintering," pp. 27-36 in Sintering--Theory and Practice. Edited by D. Kolar, S. Pejovnik, and M.M. Ristic. Elsevier Scientific Publishing Company, Amsterdam, Netherlands, 1982.

[Pet85] J.J. Petrovic, J.V. Milewski, D.L. Rohr, and F.D. Gac, "Tensile Mechanical Properties of SiC Whiskers," J. Mat. Sci., 20, 1167-1177 (1985).

[Por87] J.R. Porter, F.F. Lange, and A.H. Chokshi, "Processing and Creep Performance of SiC-Whisker-Reinforced Al_2O_3," Am. Ceram. Soc. Bull., 66 [2] 343-47 (1987).

[Pre82] K.M. Prewo and J.J. Brennan, "Silicon Carbide Yarn Reinforced Glass Matrix Composites," J. Mat. Sci., 17, 1201-1206 (1982).

[Pre86] K.M. Prewo, "The Development of Fiber Reinforced Glasses and Glass Ceramics"; pp 529-47 in Tailoring Multiphase and Composite Ceramics. Edited by R. Tressler, G. Messing, C. Pantano, and R. Newham. Plenum Publishing Corp., New York, 1986.

[Produ] Product Brochure. Tateho Chemical Industries Co., Ltd., Hyogo-ken, Japan.

[Rah87] M.N. Rahaman and L.C. De Jonghe, "Effect of Rigid Inclusions on the Sintering of Glass Powder Compacts," J. Am. Ceram. Soc., 70 [12] C-348-C-351 (1987).

[Rah88] M.N. Rahaman and L.C. De Jonghe, "Effect of Rigid Inclusions on Sintering"; pp 887-96 in Ceramic Transactions Vol. 1, Ceramic Powder Science II, Part B, The American Ceramic Society, Westerville, Ohio, 1988.

[Raj84] R. Raj and R.K. Bordia, "Sintering Behavior of Bimodal Compacts," Acta Metall., 32 [7] 1003-19 (1984).

[Rev63] K.D. Reeve, "Nonuniform Shrinkage in Sintering," Am. Ceram. Soc. Bull., 42 [8] 452 (1963).

[Rho81] W.H. Rhodes, "Agglomerate and Particle Size Effects on Sintering Yttria-Stabilized Zirconia," J. Am. Ceram. Soc., 64 [1] 19-22 (1981).

[Ric73] R.W. Rice, "Fractographic Identification of Strength-Controlling Flaws and Microstructure"; pp 323-45 in Fracture Mechanics of Ceramics, Vol. 1. Edited by R.C. Bradt,,D.P.H. Hasselman, and F.F. Lange. Plenum, New York, 1973.

[Ric81] R.W. Rice, "Mechanism of Toughening in Ceramic Matrix Composites," Cer. Eng. Sci. Proc., 2 [7-8] 661-701 (1981).

[Roj88] O.E. Rojas, M.S. Thesis, University of Florida, 1988.

[Sa84] M.D. Sacks, "Properties of Silicon Suspensions and Cast Bodies," Am. Ceram. Soc. Bull., 63 [12] 1510-15 (1984).

[Sac88] M.D. Sacks, H.-W. Lee, and O. E. Rojas, "Suspension Processing of Al_2O_3/SiC Whisker Composites," J. Am. Ceram. Soc., 71 [5] 370-79 (1988).

[Sack85] M.D. Sacks and G.W. Scheiffele, "Properties of Silicon Suspensions and Slip-Cast Bodies," Ceram. Eng. Sci. Proc., 6 [7-8] 1109-1123 (1985).

[Sacks84a] M.D. Sacks and T.Y. Tseng, "Preparation of SiO_2 Glass from Model Powder Compacts: I, Formation and Characterization of Powders, Suspensions, and Green Compacts," J. Am. Ceram. Soc., 67 [8] 526-31 (1984).

[Sacks84b] M.D. Sacks and T.Y. Tseng, "Preparation of SiO_2 Glass from Model Powder Compacts: II, Sintering," J. Am. Ceram. Soc., 67 [8] 532-37 (1984).

[Sacks88] M.D. Sacks and S.D. Vora, "Preparation of SiO2 Glass from Model Powder Compacts: III, Enhanced Densification by Sol Infiltration," J. Am. Ceram. Soc., 71 [4] 245-49 (1988).

[Sam72a] R.A.J. Sambell, D.H. Bowen, and D.C. Phillips, "Carbon Fiber Composites with Ceramic and Glass Matrices: Part1 Discontinuous Fibers" J. Mat. Sci., 7, 663-675 (1972).

[Sam72b] R.A.J. Sambell, A. Briggs, D.C. Phillips, and D.H. Bowen, "Carbon Fiber Composites with Ceramic and Glass Matrices: Part2 Continuous Fibers," J. Mat. Sci., 7, 676-681 (1972).

[Sam85] S.C. Samanta and S. Musikant, "SiC Whisker-Reinforced Ceramic Matrix Composites," Ceram. Eng. Sci. Proc., 6 [7-8] 663-72 (1985).

[Sat78] T. Sato, F. Ozawa, and S. Ikoma, "Thermal Decomposition of Aluminum Salts-Hydrates of the Chloride, Nitrate, and Sulphate, and of Ammonium Alum," J. Appl. Chem. Bio-technol., 281, 811 (1978).

[Sat84] T. Sata and T. Sasamoto, "Vaporization from Magnesia and Alumina Materials," pp. 541-552 in Advances in Ceramics, Vol 10. Edited by W.D. Kingery. American Ceramic Society, Westerville, OH, 1984.

[Sch87] G.W. Scherer, "Sintering with Rigid Inclusions," J. Am. Ceram. Soc., 70 [10] 719-25 (1987).

[Sea70] A.W. Searcy, Chapter 4 in Chemical and Mechanical Behavior of Inorganic Materials, Wiley, New York, 1970.

[Sel61] J. Selsing, "Internal Stresses in Ceramics," J. Am. Ceram. Soc., 44, 419 (1961).

[Sha86a] P.D. Shalek, J.J. Petrovic, G.F. Hurley , and F.D. Gac , "Hot-Pressed SiC Whisker-Si_3N_4 Matrix Composites," Am. Ceram. Soc. Bull., 65 [2] 351-56 (1986).

[Sha86b] T.M. Shaw, "Liquid Redistribution during Liquid-Phase Sintering," J. Am. Ceram. Soc., 69 [1] 27-34 (1986).

[Sin88] R.N. Singh and A.R. Gaddipati, "Mechanical Properties of a Uniaxially Reinforced Mullite-Silicon Carbide Composite," J. Am. Cream. Soc., 71 [2] C-100-C-103 (1988).

[Smi48] C.S. Smith, "Grains, Phases, and Interfeces: An Interpretation of Microstructure," Trans. A.I.M.E., 175, 15- (1948).

[Smi84] J.P. Smith and G.L. Messing, "Sintering of Bimodally Distributed Alumina Powders," J. Am. Ceram. Soc., 67 [4] 238-42 (1984).

[Stu71] D.R. Stull and H. Prophet, JANAF Thermochemical Tables, 2d ed. Nat. Bur. Stand. Ref. Dat. Ser., NBS, 1971.

[Swa87] P.L. Swanson, C.J. Fairbanks, B.R. Lawn, Y.-W. Mai, and B.J. Hockey, "Crack-Interface Bridging as a Fracture Resistance Mechanism in Ceramics: I, Experimental Study on Alumina," J. Am. Ceram. Soc., 70 [4] 279-89 (1987).

[Swe78] J.C. Swearangen, E.K. Beauchamp, and R.J. Eagan, "Fracture Toughness of Reinforced Glasses"; pp. 973-987 in Fracture Mechanics of Ceramics, Vol. 4. Edited by R.C. Bradt, D.P.H. Hasselman and F.F, Lange. Plenum Publishing Corp., New York, 1978.

[Tad87] Th.F. Tadros, pp. 1-16 in Solid/Liquid Dispersions. Edited by Th.F. Tadros. Academic Press, New York, 1987.

[Tak87] F. Takao, W.R. Cannon, and S.C. Danforth, "Nonaqueous Colloidal Processing of Reaction-Bonded Silicon Nitride-SiC Whisker Composites"; pp. 699-708 in Ceramic Powder Science, Advances in Ceramics, Vol. 21. Edited by G.L. Messing, K.S. Mazdiyasni, J.W. McCauley, and R.A. Haber. Am. Ceram. Soc., Westerville, OH., 1987.

[Thu67] F. Thummler and W. Thomma, "The Sintering Process," Metall. Rev., 1, 69-108 (1967).

[Tie86] T.N. Tiegs and P.F. Becher, "Whisker Reinforced Ceramic Composites"; pp. 639-648 in Tailoring Multiphase and Composite Ceramics. Edited by R.Tressler, G. Messing, C. Pantano, and R. Newnham. Plenum Publishing Corp., New York, 1986.

[Tie87a] T.N. Tiegs and P.F. Becher, "Thermal Shock Behavior of an Alumina-SiC Whisker Composite," J. Am. Ceram. Soc., 70 [5] C-109-C-111 (1987).

[Tie87b] T.N. Tiegs and P.F. Becher, "Sintered Al_2O_3-SiC-Whisker Composites," Am. Ceram. Soc. Bull., 66 [2] 339-42 (1987).

[Var77] O. Vardar, I. Finne, D.R. Viswas, and R.M. Fulrath, "Effect of Spherical Pores on the Strength of a Polycrystalline Ceramics," Int. J. Fract., 13 [2] 215-23 (1977).

[Was21] E.W. Washburn, "The Dynamics of Capillary Flow," Phys. Rev., 17 [3] 273-283 (1921).

[Wei85] G.C. Wei and P.F. Becher , "Development of SiC-Whisker-Reinforced Ceramics," Am. Ceram. Soc. Bull., 64 [2] 298-304 (1985).

[Wei88] M.W. Weiser and L.C. De Jonghe, "Inclusion Size and Sintering of Composite Powders," J. Am. Ceram. Soc, 71 [3] C-125-C-127 (1988).

[Yaj79] S. Yajima, K. Okamura, T. Katsuzawa, Y. Hasegawa, and T. Shishido, Nature 279, 706 (1979).

[Yeh88] T.-S. Yeh and M.D. Sacks, "Low-Temperature Sintering of Aluminum Oxide," J. Am. Ceram. Soc., 71 [10] 841-44 (1988).

[Yeh89] T.S. Yeh, Ph.D. Dissertation, University of Florida, 1989.

[Zal83] R. Zallen, Chapter 4 in The Physics of Amorphous Solids. John Wiley & Sons, New York, 1983.

[Zha88a] J. Zhao and M. Harmer, "Effect of Pore Distribution on Microstructure Development: I, Matrix Pores," J. Am. Ceram. Soc., 71 [2] 113-20 (1988).

[Zha88b] J. Zhao and M. Harmer, "Effect of Pore distribution on Microstructure Development: II, First- and Second-Generation Pores," J. Am. Ceram. Soc., 71 [7] 530-39 (1988).

[Zie70] K.D. Ziegel, "The Viscosity of Suspensions of Large, Nonspherical Particles in Polymer Fluids," J. Colloid Interface Sci., 34 [2] 185-196 (1970).

BIOGRAPHICAL SKETCH

Hae-Weon Lee was born on August 15, 1957, in Taegu, Republic of Korea. He has three children, Kang-Eun, Jong-Hyuk and Jong-Woo, with wife, Jin-Shim Park Lee.

In 1980, He received his B.S. in ceramic engineering from Seoul National University, Seoul, Korea. After receiving M.S. in ceramic engineering from the same university in 1982, he joined Korean Army and served for 6 months.

In 1983, during his study for the Ph.D. in ceramic engineering at SNU, he was selected by Ministry of Education of Korea to be a student studying abroad. He joined the Department of Materials Science and Engineering, University of Florida, with the support of the Korean Government, in 1984.

Since he joined the department, he has published or will publish 8 articles, which are related to the dissertation work.

I certify that I have read this study and that in my opinion it conforms to acceptable standards of scholarly presentation and is fully adequate, in scope and quality, as a dissertation for the degree of Doctor of Philosophy.

Michael D. Sacks, Chair
Associate Professor of
Materials Science and
Engineering

I certify that I have read this study and that in my opinion it conforms to acceptable standards of scholarly presentation and is fully adequate, in scope and quality, as a dissertation for the degree of Doctor of Philosophy.

David E. Clark
Professor of Materials Science
and Engineering

I certify that I have read this study and that in my opinion it conforms to acceptable standards of scholarly presentation and is fully adequate, in scope and quality, as a dissertation for the degree of Doctor of Philosophy.

Robert T. DeHoff
Professor of Materials Science
nd Engineering

I certify that I have read this study and that in my opinion it conforms to acceptable standards of scholarly presentation and is fully adequate, in scope and quality, as a dissertation for the degree of Doctor of Philosophy.

Chang T. Sun
Professor of Aerospace
Engineering, Mechanics,
Engineering Science

I certify that I have read this study and that in my opinion it conforms to acceptable standards of scholarly presentation and is fully adequate, in scope and quality, as a dissertation for the degree of Doctor of Philosophy.

Ellsworth D. Whitney
Professor of Materials Science and Engineering

This dissertation was submitted to the Graduate Faculty of the College of Engineering and to the Graduate School and was accepted as partial fulfillment of the requirements for the degree of Doctor of Philosophy.

May, 1990

for Winfred M. Phillips
Dean, College of Engineering

Madelyn M. Lockhart
Dean, Graduate School